

THE SCHWERTFEGER LIBRARY
1225 W. Dayton Street
Madison, WI 53706

**Engineering and Scientific Support for the
National Polar-orbiting Operational Environmental
Satellite System Airborne Sounder Testbed
Interferometer (NAST-I) Instrument**

Contract NAS1-00070
Modification No. 1
(Effective Date 16 February 2001)

Final Report

University of Wisconsin-Madison
Space Science and Engineering Center

30 November 2001

Table of Contents

1.0 INTRODUCTION	3
2.0 SUMMARY BY TASK.....	3
2.1 TRANSPORT AND CHEMICAL EVOLUTION OVER THE PACIFIC (TRACE-P) EXPERIMENT IN-FIELD SUPPORT	3
2.2 TRACE-P FINAL CALIBRATED DATASET PREPARATION AND DISTRIBUTION.....	3
2.3 TRACE-P DATA ANALYSIS.....	4
2.3.1 <i>Cloud Property Retrieval</i>	5
2.3.2 <i>Trace Gas Column Retrieval</i>	5
2.4 NAST-I BLACKBODY SUBSYSTEM CALIBRATION.....	8
2.4.1 <i>Controller Electronics Resistance Measurement Accuracy</i>	8
2.4.2 <i>Blackbody Thermistor Accuracy</i>	9
2.5 NAST-I MIRROR DATA WAREHOUSE SUPPORT.....	11
2.5.1 <i>Mirroring Warehouse Summary</i>	11
2.5.2 <i>User's Guide</i>	12
2.6 CAMEX-IV EXPERIMENT IN-FIELD SUPPORT	13
2.7 S-HIS ACTIVITIES FOR NPOESS	14
2.7.1 <i>Scanning-HIS Vibration-Induced Tilt Analysis</i>	14
2.7.1.1 <i>Amplitude Modulation Effects of Tilt and Tests for Proof of Concept</i>	14
2.7.1.2 <i>Sample-Position Error effects of tilt</i>	15
2.7.1.3 <i>Vibrational Tilt Modeling</i>	16
2.7.2 <i>Instrumentation</i>	16
2.7.2.1 <i>Bomem Dynamic Alignment Mirror Mechanism Modifications</i>	18
2.7.2.2 <i>Tilt Board General Description</i>	19
2.7.3 <i>Observations</i>	20
2.7.4 <i>Analysis</i>	21
3.0 CONCLUSIONS.....	27
4.0 PUBLICATIONS	27
5.0 REFERENCES.....	27
APPENDIX A: TRACE-P NAST-I BRIGHTNESS TEMPERATURE GRAPHS	28
APPENDIX B: CLAMS BRIGHTNESS TEMPERATURE GRAPHS	36
APPENDIX C: SUGGESTED MODIFICATIONS TO NAST FOR IMPROVING PERFORMANCE AND RELIABILITY.....	43
APPENDIX D: CLOUD PROPERTIES PUBLICATION.....	46

1.0 Introduction

This report comprises the "Contract Final Report", Task 14 of the NASA Contract NAS1-00070 from NASA Langley Research Center to the University of Wisconsin Space Science and Engineering Center (UW-SSEC). This report describes the activities performed under tasks 8–15 for the time period ending 31 October 2001. The report for tasks 1–7 under this contract was submitted on 31 May 2001.

2.0 Summary by Task

Tasks 8–15 under the NASA contract are summarized in the following sections. The identification of each task, and the corresponding section in which they appear in this report, is given below:

Contract Task ID	Description	Report Section
Task 8	Trace-P In-field Support	Section 2.1
Task 9	Trace-P Final Calibrated Dataset Preparation and Distribution	Section 2.2
Task 10	Trace-P Data Analysis	Section 2.3
Task 11	NAST-I Instrument Calibration Support	Section 2.4
Task 12	NAST-I Mirror Data Warehouse Support	Section 2.5
Task 13	CAMEX-IV In-Field Support	Section 2.6
Task 14	Contract Final Report	All
Task 15	S-HIS Activities for NPOESS	Section 2.7

Table 1: Mapping of contract task ID, description, and report Section number.

2.1 Transport and Chemical Evolution over the Pacific (TRACE-P) Experiment In-field Support

The UW-SSEC provided in-field support for the NAST-I instrument during the TRACE-P field experiment. This support was organized into three phases: Hawaii, Okinawa, and Alaska. The UW deployed one person to Hawaii during the Proteus deployment along with the support equipment used to process NAST-I data in the field. After the Proteus left Hawaii, the support equipment was shipped ahead to Kadena Air Base on the island of Okinawa, Japan where two UW personnel supported the deployment. After the Okinawa deployment, the support equipment was sent to Eielson AFB near Fairbanks, Alaska where one person from UW supported the deployment.

At the end of each of the three phases of the deployment, a set of re-writeable compact discs (CD-R) was provided to the NAST Principal Investigator containing a complete set of preliminary calibrated radiances from in-field data processing.

2.2 TRACE-P Final Calibrated Dataset Preparation and Distribution

The TRACE-P dataset, containing raw data, quality controlled spectral radiances in native NAST-I (i.e., RNC) format and 3-line smoothed products in netcdf format is available online at

<http://gi.ssec.wisc.edu/~nasti/nastidata.php3>

by selecting "TRACE-P" from the drop-down menu under "Experiment".

Table 2 gives a summary of the approximately 60 hours of TRACE-P flight data available. Please note that data start and end times are indicative of raw data availability only, and may not correspond to quality-controlled data availability. In addition, Column 6 has been provided to give the difference in time between the initial and final data collection times during each flight, not taking into account data outages.

The final four columns give the relevant data archive volume numbers, which correspond to both the storage location on the online database, and the original CD-ROM archive number.

Date of Aircraft Takeoff	Flight Number	Departure Location	Data Start Time (HH:MM)	Data End Time (HH:MM)	End time minus start time (hr, min)	Raw Data	Calibrated, QCed Radiances	3-line smooth without tilt correction	3-line smooth with tilt correction
010219	116	Mojave	17:52	23:25	5 hr 33 min	NASTI-361 NASTI-362	NASTI-367	NASTI-366	NASTI-366
010226	117	Honolulu	19:45	23:47	4 hr 2 min	NASTI-363 NASTI-364	NASTI-370	NASTI-368	NASTI-369
010301	118	Majuro	20:43	21:54	1 hr 11 min	NASTI-365	NASTI-371	NASTI-371	NASTI-371
010308	120	Okinawa	05:19	08:43	3 hr 24 min	NASTI-372 NASTI-373	NASTI-374	NASTI-375	NASTI-376
010309	121	Okinawa	00:15	06:13	5 hr 58 min	NASTI-377 NASTI-378 NASTI-379	NASTI-380 NASTI-381	NASTI-382 NASTI-383	NASTI-384 NASTI-385
010310	122	Okinawa	03:04	08:49	5 hr 45 min	NASTI-386 NASTI-387 NASTI-388	NASTI-390 NASTI-391	NASTI-392 NASTI-393	NASTI-394 NASTI-395
010312	123	Okinawa	00:03	05:13	5 hr 10 min	NASTI-396 NASTI-397 NASTI-398	NASTI-399	NASTI-400	NASTI-401
010313	124	Okinawa (aborted) 1 spiral.	02:43	03:39	56 min	NASTI-402	NASTI-403	NASTI-404	NASTI-405
010316	125	Kadena	01:38	04:06	2 hr 28 min	NASTI-406 NASTI-407	NASTI-427	NASTI-428	NASTI-429
010318	126	Yokota	10:59	17:08	6 hr 9 min	NASTI-430 NASTI-431 NASTI-432	NASTI-433 NASTI-434	NASTI-435 NASTI-436	NASTI-437 NASTI-438
010320	127	Fairbanks	19:26	02:14 (next day)	6 hr 48 min	NASTI-408 NASTI-409 NASTI-410 NASTI-411	NASTI-412 NASTI-413	NASTI-414 NASTI-415	NASTI-416 NASTI-417
010321	128	Fairbanks	19:18	01:53 (next day)	6 hr 35 min	NASTI-418 NASTI-419 NASTI-420	NASTI-421 NASTI-422	NASTI-423 NASTI-424	NASTI-425 NASTI-426
010323	129	Fairbanks	04:20	07:17	2 hr 57 min	NASTI-439 NASTI-440	NASTI-441	NASTI-442	NASTI-443
010326	130	Fairbanks	16:38	23:26	6 hr 48 min	NASTI-446 NASTI-447 NASTI-448 NASTI-449	NASTI-444	NASTI-450 NASTI-451	NASTI-452 NASTI-453

Table 2: NAST-I data availability for the TRACE-P experiment. Technical problems during Flight 119 resulted in no data being collected for that particular deployment.

Quick-look graphs of brightness temperatures for the window (transparent) channel and near-instrument (opaque) channel for each flight are provided in Appendix A.

2.3 TRACE-P Data Analysis

This section summarizes the two data analysis activities that were conducted at least in part with the support of this contract. The activities are related cloud property retrieval and trace gas column retrieval.

2.3.1 Cloud Property Retrieval

A paper was presented during the contract time period concerning cloud property retrieval by Paolo Antonelli of UW-SSEC titled "Retrieval of cloud top height, effective emissivity, and particle size, from aircraft high spectral resolution infrared measurements" (see Section 4.0). This paper is attached as Appendix D.

2.3.2 Trace Gas Column Retrieval

An algorithm developed under NASA funding to retrieve total column carbon monoxide and methane amounts was applied to the NAST-I data from the TRACE-P experiment. The technique applied to the observations is one developed for the NASA SAFARI experiment to map CO distribution from fires.

The method makes use of high spectral resolution emission lines observed by the infrared spectrometer to derive an optical depth using weak absorption lines. It is less sophisticated than a full profile retrieval approach, but is very useful for a survey result of localized events.

A ratio of on-line to off-line emission for selected lines of the gas of interest provides a measure of the gas amount. The selected wavenumbers are displayed in Table 3.

Gas	On-line wavenumbers	Off-line wavenumbers
CO	2150.80	2151.77
	2154.667	2153.698
	2158.05	2159.02
	2158.52	2164.80
	2165.29	2166.75
	2165.77	2168.193
	2169.157	2170.126
	2172.54	2173.506
CH4	2173.02	
	1230.0	1230.96
	1240.62	1240.14
	1241.11	1241.59

Table 3: Wavenumbers used in the determination of trace gas amounts.

The form of the equation to be used can easily be derived from a single-layer atmosphere approximation, i.e.,

$$N_{\nu}^{Obs} = t_{\nu} \cdot N_{\nu}^{Surf} + N_{\nu}^{Atm} + t_{\nu} \cdot N_{\nu}^{Ref} \quad (1)$$

with the assumptions that

$$N_{\nu}^{Ref} = 0 \text{ and } N_{\nu}^{Atm} = B_{\nu}(\overline{T_{Atm}}),$$

In these equations, $t_{\nu} = \exp[-\tau_{\nu}]$ is the atmospheric transmission for wavenumber ν (τ being the optical depth), N_{ν}^{Obs} is the observed upwelling spectral radiance at an altitude of 20 km, N_{ν}^{Surf} is the emission from the surface, N_{ν}^{Atm} is the atmospheric emission, N_{ν}^{Ref} is the contribution from surface reflection, and B is the Planck emission function at a temperature T_A which approximates the mean atmospheric temperature. Neglecting the reflected radiance and substituting for the atmospheric emission leads to:

$$N_{\nu}^{Obs} \cong t_{\nu} \cdot N_{\nu}^{Surf} + B_{\nu}(\overline{T_{Atm}}). \quad (2)$$

We then rearrange terms and split equation (2) into separate expressions for the on-line and off-line radiance:

$$t_{on} \cdot N_{on}^{Surf} = N_{on}^{Obs} - B_{on}(\overline{T_{Atm}}) \quad (3)$$

$$t_{off} \cdot N_{off}^{Surf} = N_{off}^{Obs} - B_{off}(\overline{T_{Atm}}) \quad (4)$$

We further assume that the surface emitted radiance is equal for both on-line and off-line spectral channels, i.e., that $N_{on}^{Surf} = N_{off}^{Surf}$.

We may then divide equations (3) and (4) to obtain a ratio. Using the previously mentioned relationship between transmission and optical depth, we find

$$\frac{t_{on}}{t_{off}} = \frac{\exp(-\tau_{on})}{\exp(-\tau_{off})} = \frac{N_{on}^{Obs} - B_{on}(\overline{T_{Atm}})}{N_{off}^{Obs} - B_{off}(\overline{T_{Atm}})}.$$

Taking the natural log of both sides results in the expression

$$\Delta \tau = \tau_{on} - \tau_{off} = -\ln \left[\frac{N_{on}^{Obs} - B_{on}(\overline{T_{Atm}})}{N_{off}^{Obs} - B_{off}(\overline{T_{Atm}})} \right].$$

The measured optical depths are divided by a calculated optical depth using a climatological trace gas profile to obtain a scale factor. These measured scale factors can be used to obtain a column amount. Figures 1–4 show results using this method from both the TRACE-P and CLAMS (refer Section 2.6) experiments.

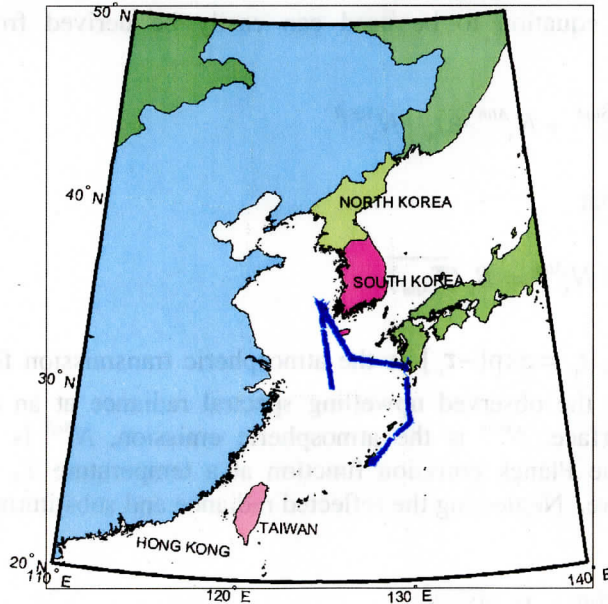


Figure 1. Flight track for NAST-I flight 12 March 2001 to the Yellow Sea near the Korean Peninsula corresponding to the CO analysis presented in Figure 2.

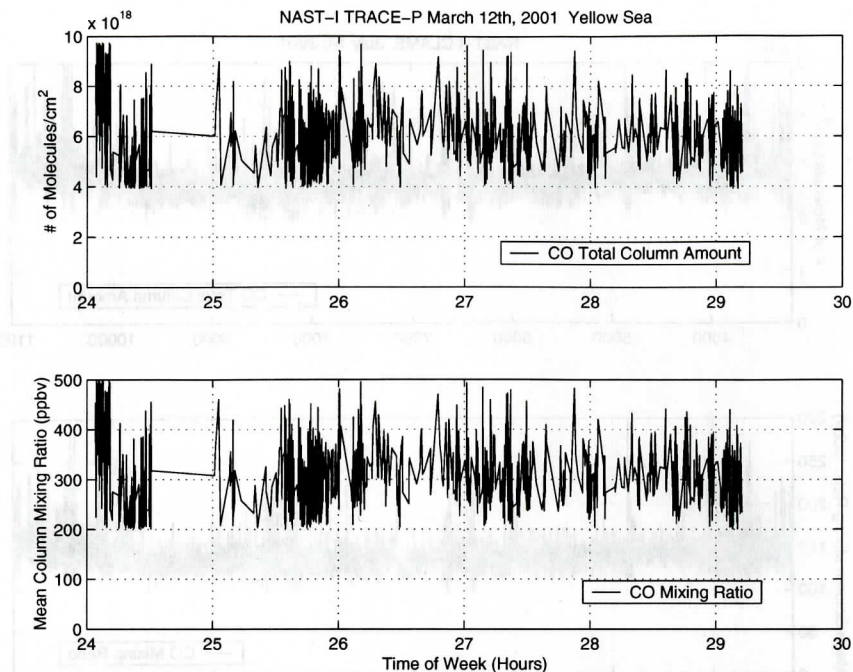


Figure 2. Time series of derived column carbon monoxide from 00:03 to 05:13 UTC on 12 March 2001 using the technique described in the text. The upper panel is a total column amount while the lower panel is the mean mixing ratio. The average column amounts are 2.5 to 3 times larger than mid-latitude summer climatology presumably due to the large emission of CO from the Chinese mainland.

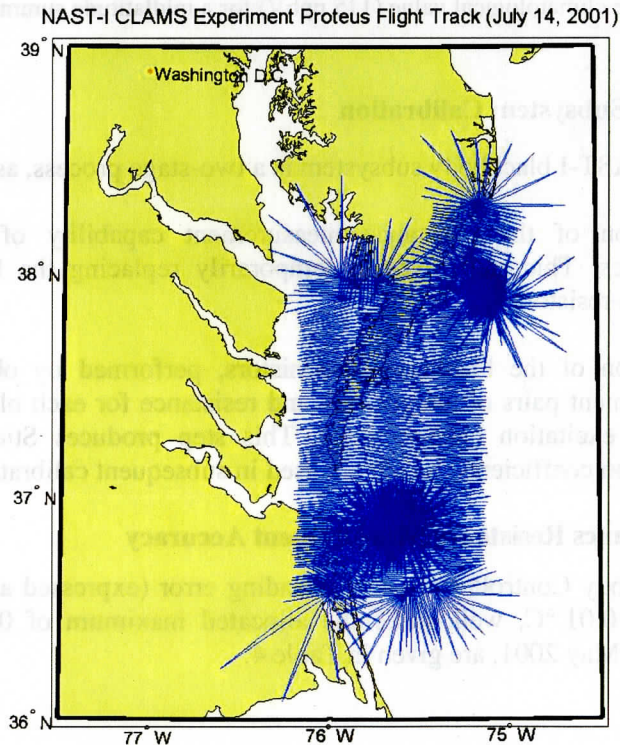


Figure 3. Flight track for NAST-I flight 14 July 2001 in the Chesapeake Bay area corresponding to CO analysis presented in Figure 4.

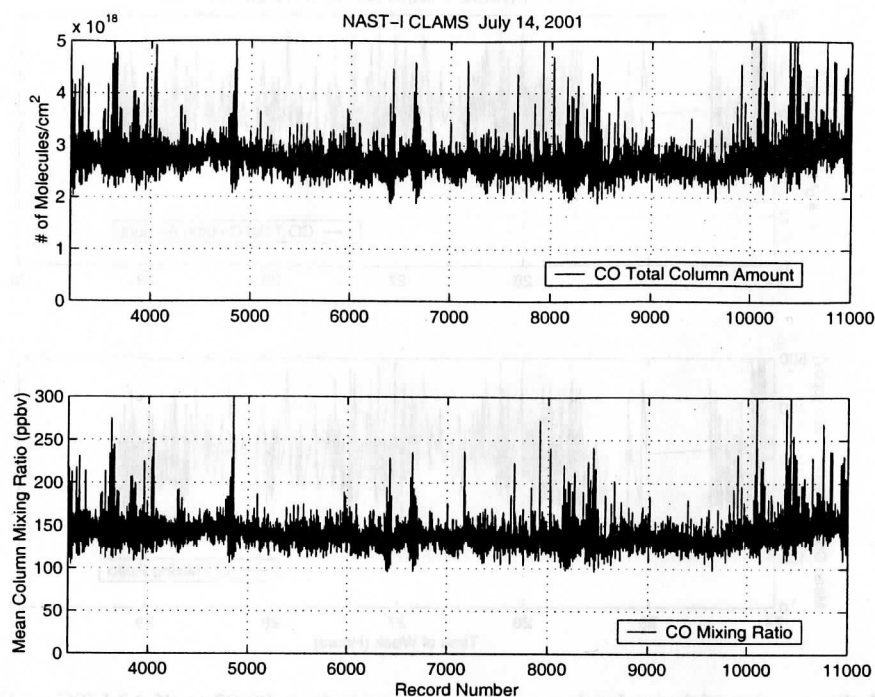


Figure 4. Time series of derived column carbon monoxide from 16:00 to 17:45 UTC on 14 July 2001 using the technique of described in the text. The Proteus aircraft was in the altitude range 54,000 to 56,000 feet during this time period. This data has not been filtered for noise spikes. The magnitude of the CO derived amount is close to the climatological value (115 ppbV) for a midlatitude summer atmosphere.

2.4 NAST-I Blackbody Subsystem Calibration

Calibration of the NAST-I blackbody subsystem is a two-stage process, as follows:

- i) calibration of the resistance measurement capability of the blackbody controller electronics. This step involves temporarily replacing the blackbody thermistors with precision resistors.
- ii) calibration of the blackbody thermistors, performed by obtaining three very precise measurement pairs of temperature and resistance for each blackbody thermistor, at each relevant excitation current range. This step produces Stienhart and Hart thermistor calibration coefficients, which are used in subsequent calibration processing.

2.4.1 Controller Electronics Resistance Measurement Accuracy

The NAST-I Blackbody Controller resistance reading error (expressed as an equivalent temperature error) was found to be 0.01 °C, well under the allocated maximum of 0.02 °C. The details of this calibration, conducted in May 2001, are given in Table 4.

NAST Blackbody Controller Calibration						
Nominal		Measured Values of Calibration Resistors (Ohms) (May 9, 2001)				
Temperature	Resistance	A - Top	B - Apex	C - Bot	D - Refl.	Plug Color
60	2,740	2,741.4	2,740.5	2,730.0	2,740.7	Grey
27	9,310	9,262.8	9,281.7	9,286.0	9,292.8	White
21	11,800	11,722.6	11,746.6	11,720.7	11,762.2	Black
-13	54,900	54,650.0	54,755.0	55,008.0	54,822.0	Red

Resistances read in place of Blackbody at blackbody connector

Equivalent Temperature of Calibration Resistor (C)					
Nom Temp.	A - Top	B - Apex	C - Bot	D - Refl.	
60	60.195	60.205	60.320	60.203	
27	26.904	26.853	26.841	26.823	
21	21.095	21.046	21.099	21.013	
-13	-12.809	-12.847	-12.940	-12.872	

Variation within color				
0.000	0.010	0.124	0.008	
0.000	-0.051	-0.063	-0.081	
0.000	-0.050	0.004	-0.082	

ABB: NAST Reported Temperatures (5/17/01)					
Nom Temp.	A - Top	B - Apex	C - Bot	D - Refl.	
60					
27					
21	21.106	21.046	21.101		
-13					

current range 0

HBB: NAST Reported Temperatures (5/17/01)					
Nom Temp.	A - Top	B - Apex	C - Bot	D - Refl.	
60	60.188	60.197	60.314		
27	26.901	26.851	26.839		
21					
-13					

current range 3
current range 2

ABB: (NAST Reported Temperature) - (Eq. Temp. of Cal. R)					
Nom Temp.	A - Top	B - Apex	C - Bot	D - Refl.	Quantization
60					
27					
21*	0.011	0.000	0.002		0.050
-13					

* temperature values were averaged over 2 minutes

HBB: (NAST Reported Temperature) - (Eq. Temp. of Cal. R)					
Nom Temp.	A - Top	B - Apex	C - Bot	D - Refl.	Quantization
60	-0.007	-0.008	-0.006		0.001
27	-0.003	-0.002	-0.002		0.001
21					
-13					

Table 4. NAST-I Blackbody Controller resistance measurement errors.

2.4.2 Blackbody Thermistor Accuracy

The results from the blackbody thermistor calibration, conducted in January 2001, are presented in Figures 5a (ambient blackbody) and 5b (hot blackbody). The maximum blackbody temperature error for operation under laboratory conditions was found to be $+0.064^{\circ}\text{C}$ (at 22.51°C) for the ambient blackbody and -0.052°C (at 59.68°C) for the hot blackbody. These errors both lie safely within the allocated maximum of $\pm 0.098^{\circ}\text{C}$.

Calibration for blackbody temperatures typically encountered in the field (i.e., during flight) was conducted for the case of NAST-I flying in the ER-2, where the ambient blackbody temperatures (-13°C) are higher than those encountered in the Proteus (less than -60°C). Prior to the next deployment, the blackbodies will be calibrated over the Proteus environment's temperature range.

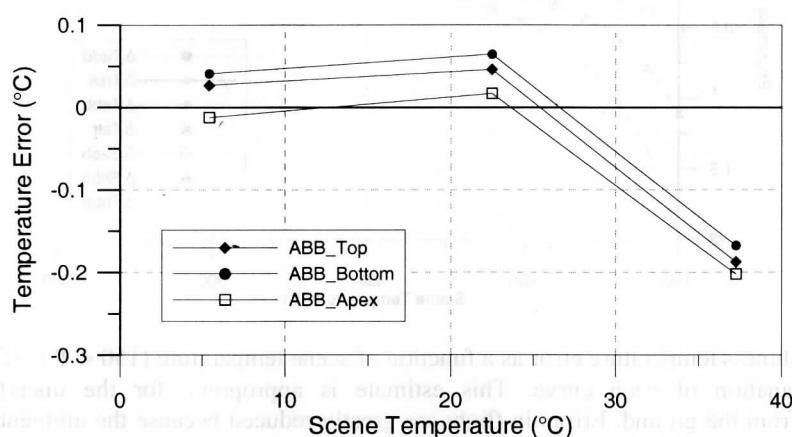


Figure 5a. Temperature errors arising from the use of Nominal Stienhart and Hart coefficients for the blackbody thermistors in place of the coefficients derived from the latest calibration, for the case of laboratory operation for the ambient blackbody. The Nominal coefficients are currently used in NAST-I calibration processing so the above curves represent actual errors.

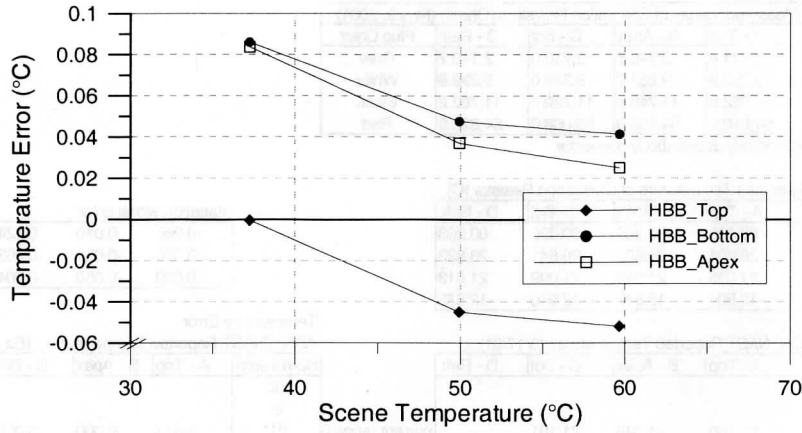


Figure 5b. As for 5a, except for the hot blackbody.

Figures 6a and 6b show the impact of subsystem uncertainties on the NAST-I instrument measurement errors. The root-sum-square (RSS) combination of the uncertainty in blackbody temperature (assumed to be ± 0.098) together with other subsystem uncertainties, as listed in Table 5, is illustrated as ΔT_{rss} (thick line). These errors are expected to be less than 0.2 K for the for the end-to-end NAST-I laboratory calibration points that are typically run at 313 K and 333 K.

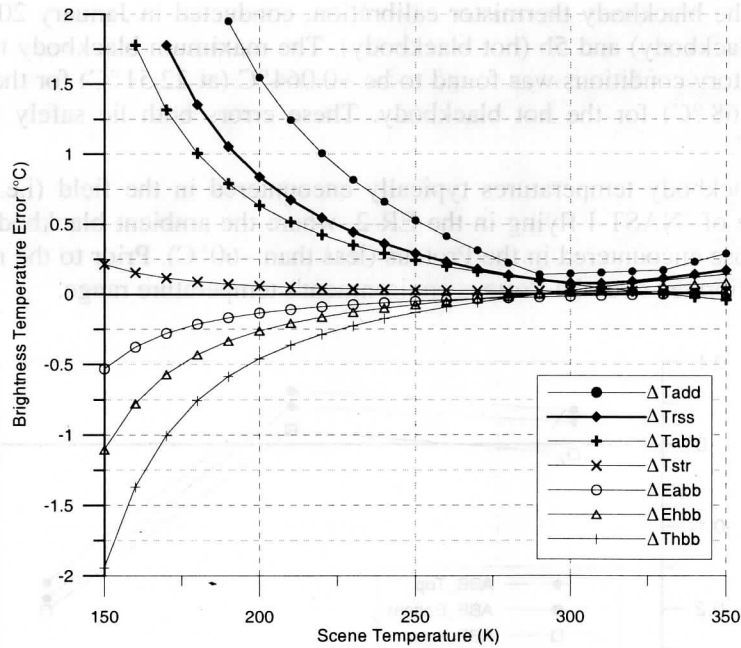


Figure 6a. Brightness temperature error as a function of scene temperature ($150 < T < 350$ K). Refer to Table 5 for an explanation of each curve. This estimate is appropriate for the uncertainty in uplooking measurements from the ground. Errors in flight are greatly reduced because the ambient blackbody operates at much colder temperatures.

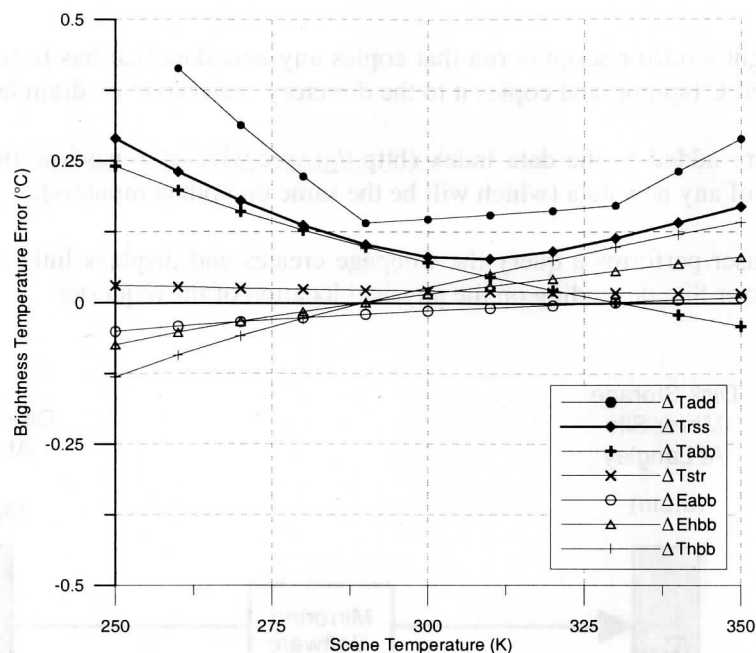


Figure 6b. Detail from Figure 6a, showing brightness temperature error as a function of scene temperature solely in the 250 to 350 K range. This is the range appropriate for laboratory tests.

Input Parameter [unit]		Value	Uncertainty	Uncertainty Value
Wavenumber, [cm ⁻¹]	wn	770	N/A	
Temp. of Hot Blackbody, [K]	Thbb	330	ΔThbb	0.098 [K]
Temp. of Cold Blackbody, [K]	Tcbb	290	ΔTcbb	0.098 [K]
Temp. of structure reflecting into BB's, [K]	Tstr	300	ΔTstr	5 [K]
Emissivity of HBB, [-]	Ehbb	0.996	ΔEhbb	0.002 [-]
Emissivity of CBB, [-]	Ecbb	0.996	ΔEhbb	0.002 [-]

Table 5. NAST-I instrument calibration errors arising from various subsystem uncertainties.

2.5 NAST-I Mirror Data Warehouse Support

The Mirror Data Warehouse has been shipped to NASA LaRC. The Langley warehouse contains an exact copy of the data at Wisconsin. UW personnel assisted in setting up the hardware and the “mirroring” capability has been confirmed to work properly. In this section we provide an overview of the mirroring data warehouse system (Section 2.5.1), and a user’s guide description of the mirroring software (Section 2.5.2).

2.5.1 Mirroring Warehouse Summary

The SSEC-LaRC data distribution system for NAST-I data is illustrated in Figure 7. Essentially, there are five main steps between receipt of processed data at UW-SSEC and its download by either a remote or local user.

- 1) After data is processed it is burned onto CD-ROM and added to the CD-ROM Archive.
- 2) Next, the contents of the CD-ROM are copied to the directory “reservoir” on spigot.ssec.wisc.edu.

- 3) Every night a mirror script is run that copies any new data that has been placed onto the disk storage at SSEC (spigot) and copies it to the directory "reservoir" on drain.larc.nasa.gov.
- 4) Entries are added to the data index (<http://gi.ssec.wisc.edu/~nasti/nastidata.php3>) describing the location of any new data (which will be the same on both computers).
- 5) When a user performs a query the webpage creates and displays links to either the SSEC or Langley Mirror Site depending on the physical location of the requester.

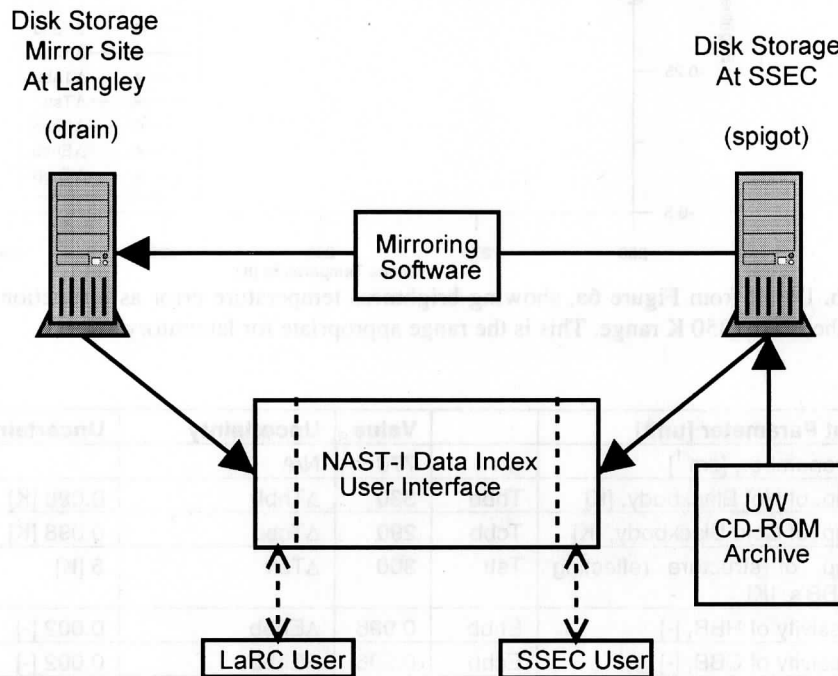


Figure 7. Schematic diagram of the NAST-I data mirroring system linking SSEC and Langley data storage devices "drain" and "spigot".

2.5.2 User's Guide

The mirroring process is currently performed at 9:05 UTC each day by way of the following entry in drain's root's crontab: "5 9 * * * /root/bin/sync_controller". Altering the time of data synchronization can be achieved by using the command "crontab -e" to edit the crontab. (The format is space delimited values for minute, hour, month, year, and day of week (0 through 7, Sunday through Saturday) in that order).

The shell script which manages the data synchronization is /TOOLS/dev/webtests/nasti2/sync_controller, a script under cvs configuration management. The first thing the script does is to set up the variables PIDFILE, PIDTEMP, LOGFILE, and RSYNC_OPTIONS. Then the script looks to see if a PIDFILE corresponding to an rsync process currently exists; if so, the process is killed and a new rsync process is begun. This prevents any complications which may arise should the duration of any single mirroring process exceed 24 hours.

The rsync process creates a logfile, /tmp/synclog.YYYYMMDD, in which all data transfers and any transmission errors are recorded. All of the reservoir directory on drain, except for /reservoir/tmp, is a carbon copy of spigot with the same permissions, owner, group, times and soft links. Any files on drain that are not on spigot will be deleted. After the rsync is complete the PIDFILE is removed.

Drain connects securely to spigot by way of an ssh key which can be recreated if needed by the following process.

- i) run "ssh-keygen -b 1024" in the /root/.ssh directory.
- ii) when asked for a filename simply press enter to get the default; when asked for a passphrase simply press enter once again. This way you can connect without ever having to enter a password.
- iii) A file called identity.pub will have been created, which you append to the /user/.ssh/authorized_keys file of the computer you are connecting to.

2.6 CAMEX-IV Experiment In-Field Support

Originally this task called for participation in the CAMEX-IV experiment. Under direction of the NAST-I Principal Investigator the experiment field support was changed from CAMEX-IV to a NASA Langley led experiment known as CLAMS (Chesapeake Lighthouse and Aircraft Measurements for Satellites). A preliminary data set of processed NAST-I data was provided to the NAST-I Principal Investigator at the end of the CLAMS field phase.

The CLAMS preliminary dataset is currently available online at

<http://gi.ssec.wisc.edu/~nasti/nastidata.php3>

by selecting "CLAMS" from the drop-down menu titled "Experiment".

Table 6 gives a summary of the approximately 40 hours of CLAMS data available, sorted by flight number. As for the Table 2, the final four columns give the relevant data volume number, which correspond to both the directory in which the data is located on the online database, and the original CD-ROM archive number.

Date of Aircraft Takeoff	Flight Number	Data Start Time (HH:MM)	Data End Time (HH:MM)	Duration	Raw Data	Calibrated, QC Radiances	3-line smooth without tilt correction	3-line smooth with tilt correction
010710	135	12:46	18:19	5 hr 33 min	NASTI-475 NASTI-476 NASTI-477 NASTI-478	NASTI-478 NASTI-479 NASTI-480	NASTI-478 NASTI-479 NASTI-480	
010712	136	11:44	16:28	4 hr 44 min	NASTI-481 NASTI-482	NASTI-530	NASTI-483 NASTI-484	
010713	137	00:14	04:58	4 hr 44 min	NASTI-485 NASTI-486	NASTI-487	NASTI-486	
010714	138	14:21	18:43	4 hr 22 min	NASTI-488 NASTI-489	NASTI-490	NASTI-491	
010717	140	11:21	17:24	6 hr 3 min	NASTI-492 NASTI-493	NASTI-494	NASTI-495	NASTI-496
010721	141	23:10	05:25 (next day)	6 hr 15 min	NASTI-497 NASTI-498 NASTI-499	NASTI-500 NASTI-501	NASTI-502 NASTI-503	
010725	142	19:07	22:29	3 hr 22 min	NASTI-504 NASTI-505	NASTI-506	NASTI-507	NASTI-508
010726	143	14:10	16:28	2 hr 18 min	NASTI-509	NASTI-510	NASTI-511	NASTI-511
010728	144	11:55	18:10	6 hr 15 min	NASTI-512 NASTI-513 NASTI-514	NASTI-515 NASTI-516	NASTI-517 NASTI-518	NASTI-519 NASTI-520

Table 6: NAST-I data availability for the CLAMS experiment.

2.7 S-HIS Activities for NPOESS

This section contains a summary of activities that focus on the UW Scanning-HIS instrument performance analysis.

2.7.1 Scanning-HIS Vibration-Induced Tilt Analysis

This discussion summarizes the analysis of vibration-induced tilt errors on an airborne Fourier-transform spectrometer (FTS). A theoretical description of the errors associated with flat mirror Michelson interferometers is presented in Sections 2.7.1.1 for the amplitude modulation effects and Section 2.7.1.2 for the sample position effects. The instrumentation used in this analysis is the University of Wisconsin (UW) Scanning High-resolution Interferometer Sounder (S-HIS) developed by the UW Space Science and Engineering Center (UW-SSEC) using a unique mirror tilt monitoring system. The analysis of the data includes a comparison of radiometric noise performance versus the integrated power spectrum of the tilt error.

2.7.1.1 Amplitude Modulation Effects of Tilt and Tests for Proof of Concept

For any interferometer, wavefront tilts cause a reduction of interferogram amplitudes. Amplitude modulation from a tilt is given by

$$2 J_1(z)/z \cong [1 - z^2/8 + z^4/192 - \dots], \text{ for a circular interferogram beam} \quad (4)$$

$$\sin(z)/z \cong [1 - z^2/6 + z^4/120 - \dots], \text{ for a square interferogram beam} \quad (5)$$

where J_1 is a first order Bessel function, argument $z = 2\pi \bar{\nu} R \theta_t$, θ_t is the total wavefront tilt, R is the radius (or side of the square) of the beam in the interferometer and $\bar{\nu}$ is the wavenumber. Therefore, for the shortwave band with a circular detector, the effect of tilt on interferogram amplitudes $F(x, \theta_t)$ is approximately given by

$$\begin{aligned} F(x, \theta_t) &= [2 J_1(2\pi \bar{\nu} R \theta_t) / (2\pi \bar{\nu} R \theta_t)] F(x, \theta_t=0) \\ &\cong [1 - \frac{1}{2}(\pi \bar{\nu} R \theta_t)^2] F(x, \theta_t=0) \end{aligned} \quad (6)$$

where the argument x is the optical path difference (OPD) and $\bar{\nu}$ is the average wavenumber in the band. This relationship is not rigorous for broad spectral bands like those of Scanning HIS, because of the wavenumber dependence shown in Equations 4 and 5. However, we expect that it should provide a useful formulation for checking our basic understanding and implementation of tilt measurements. The two other spectral bands of the Scanning HIS 3-color detector subsystem should be more closely approximated by the relationship for a square beam, making the coefficient of $\frac{1}{2}$ in Equation 6 closer to $\frac{2}{3}$. Probably, the effective coefficient (including R) will be refined from the tilt test data itself.

The total tilt consists of the combination of static tilt (believed to arise mainly from the mismatch of beamsplitter and compensator wedges) and the tilt jitter caused by vibration. Each is a vector measured with respect to orthogonal axes (x, y). Therefore,

$$\begin{aligned} \theta_t^2(x, \nu) &= [\theta_{x0}(\nu) + \theta_x(x)]^2 + [\theta_{y0}(\nu) + \theta_y(x)]^2 \\ &= [\theta_{x0}^2(\nu) + \theta_{y0}^2(\nu)] + [\theta_x^2(x) + \theta_y^2(x)] + 2 [\theta_{x0}(\nu) \theta_x(x) + \theta_{y0}(\nu) \theta_y(x)] \end{aligned}$$

$$= A(v) + B(x) + 2 [\theta_{x0}(v) \theta_x(x) + \theta_{y0}(v) \theta_y(x)] \quad (7)$$

where the subscript 0 labels the static tilts which can be wavenumber dependent (because they arise largely from refraction), and the subscripts x and y refer to the 2-D coordinate system of the tilt used by the dynamic alignment system (remember that x is also being used as an argument representing OPD as an independent variable). Equation 7 shows that we need estimates of the static tilt to accurately represent the cross terms that influence the correlation of tilt with interferogram amplitude.

The jitter tilt angles θ_x and θ_y can be obtained from the new phase angle measurements ϕ_x and ϕ_y using the relationship

$$\theta = (\phi/360^\circ) / (s v_l) \quad (8)$$

for each orthogonal axis, where v_l is the laser wavenumber (15799.6 cm^{-1}) and s is the distance separating the "R" and "X" (or "R" and "Y") laser detectors (0.3 cm) used by the dynamic alignment system.

We need to test that our measured tilts are consistent with the expected relationship between tilt and amplitude changes to convince ourselves that the system is working properly and that no other effect exists that can not be corrected for. From Equation 6 we can separate the fractional changes of interferogram amplitudes from the tilt dependence as

$$[F(x, \theta_i) - F_{\max}(x)] / F_{\max}(x) = -\frac{1}{2} (\pi \sqrt{R} \theta_i)^2 \quad (9)$$

where $F(x, \theta_i=0)$ has been replaced with $F_{\max}(x)$, the maximum interferogram value in a measured time sequence. The relationship illustrates the expected correlation between interferogram modulation and tilt. We expect to be able to demonstrate the correlation with scatter plots and time series comparing the left-hand side evaluated near zero path difference (ZPD) with the right-hand side evaluated for the same point.

2.7.1.2 Sample-Position Error effects of tilt

In addition to affecting interferogram amplitudes, tilts cause sample-position errors on the Scanning HIS because of the way aperture sharing is used for spectral band separation. Since the center of the IR beams in the interferometer for the longwave (LW) and midwave (MW) bands are displaced from the location of the laser beam feeding the sample-triggering detector by a distance d (on the order of 1 cm), tilt causes the mean OPD for each sample of these bands to differ from the uniformly-spaced sample positions triggered by laser signal zero crossings. The error is just

$$\delta x = \theta_d(x) d \quad (10)$$

where $\theta_d(x)$ is the component of the jitter tilt (not the total tilt including static tilt) in the direction from the sample-triggering beam center to the IR beam center. The tilt $\theta_d(x)$ is defined by

$$\begin{aligned} \theta_d(x) &= +\theta_x(x) \cos \gamma - \theta_y(x) \sin \gamma, & \text{for the longwave detector} \\ &= -\theta_x(x) \cos \gamma + \theta_y(x) \sin \gamma, & \text{for the midwave detector} \end{aligned} \quad (11)$$

where γ is the angle between the x-axis and the vector to the longwave detector from the interferometer beam center, nominally 45° .

This type of error causes phase errors and can in principle create "ghosts" about individual spectral lines, depending on the spectrum of the tilt errors. From past experience, it appears that the mechanical resonances associated with vibrations are broad enough that the actual radiance errors from these sample position errors are dominantly low-resolution effects and not ghost lines.

The effect of tilt-induced sample position errors near ZPD on the LW and MW has been demonstrated in our previous analyses of Scanning HIS data. Because the sample-position errors act approximately like a translation, the low resolution effect is a change in phase that is linear in wavenumber. We have determined the slopes of the linear phase changes and shown that the LW and MW results are of opposite sign and approximately equal, as would be expected from their geometry.

2.7.1.3 Vibrational Tilt Modeling

To assure ourselves that we are correctly modeling the different aspects of the vibrational tilt induced errors, we have written routines to add modulation and sample position errors to existing SHIS data. Our goal is to recreate the vibrational tilt effects that we see in the final calibrated data. The modeling process takes the a calibrated spectrum and adds modulation errors calculated from measured tilt datasets. By using the same initial spectrum, the differences in the figures are completely due to tilt measurement datasets. As we expected, the modulation errors cause a fractional error which has a $\sqrt{2}$ dependence. Figure 8 illustrates the modulation error for this simulation example.

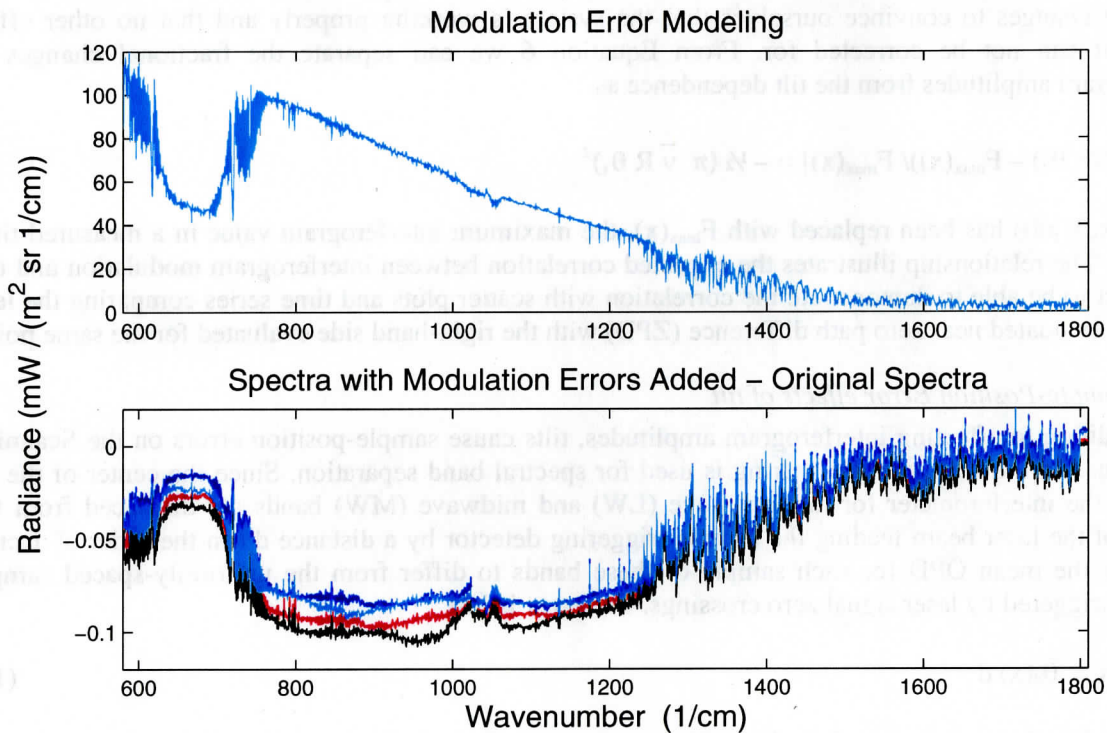


Figure 8. a) LW and MW regions of a SHIS spectrum from the AFWEX field experiment; b) the change in the simulated spectra due to tilt induced modulation effects for four sets of tilt angle measurements. A scale factor has been included in Figure 8b to improve legibility.

2.7.2 Instrumentation

The S-HIS was initially designed to fly aboard an unmanned aircraft vehicle (UAV) with limited payload capacity. Therefore, it is small and light-weight, and has low power requirements. The S-HIS is a Fourier-transform interferometer with laser-controlled sampling. It utilizes a mechanical detector cooler, eliminating the use of cryogen. Due to the initial design constraints on size, the S-HIS uses a novel "3-color" detector with a shared focal plane, eliminating the need for multiple detectors and their associated dichroic beamsplitters and coolers. The S-HIS design and performance parameters are given in Table 7.

Interferometer:		
Type:	Voice Coil Dynamically Aligned Plane mirror (Custom Bomem DA-5)	
Beam Diameter	4.5 cm	
Fringe Counting	¼ wave quadrature, continuous	
Optical path drive	Flex Pivot Porch Swing	±1.037 cm; 4 cm/s
OPD sampling reference	HeNe laser w/ white light at startup	
fvAngular FOV	40 mrad (full)	
Scan Time	0.5 s (2 spectra per spot)	
Spectral Coverage:		
Four Band Option (3-25 µm):	<u>Coverage</u>	<u>Material</u>
Extra Longwave	19–25 µm, 400–525 cm ⁻¹	HgCdTe
Longwave	10–19 µm, 525–1000 cm ⁻¹	HgCdTe
Midwave	5.5–10 µm, 1000–1800 cm ⁻¹	HgCdTe
Shortwave	3–5.5 µm, 1800–3000 cm ⁻¹	InSb
Three Band Option (3-16 µm)		
Longwave	9–16 µm, 620–1100 cm ⁻¹	HgCdTe
Midwave	5.5–9.9 µm, 1100–1800 cm ⁻¹	HgCdTe
Shortwave	3–5.5 µm, 1800–3000 cm ⁻¹	InSb
Spectral Resolution:	0.5 cm ⁻¹	
Spatial Field-of-view:		
Instrument Field-of-view	100 mrad (nadir: 2 km from 20 km altitude)	
Cross Track Scan Step	0.15 rad	Programmable
Number of IFOV per scan	11 earth views + 2 calibration views	Programmable
Dwell time per spot	1 s	Programmable
Total scan time	15 s	Programmable
Cooler/Temperature:	0.6 W Stirling Cooler (Litton), 68 K	
Mass/Size:	70 kg; 0.05 m ³	
Power:	225 W	
Onboard processing:	DSP numerical filters	
RMS noise (per spot):	<0.25K at 260 K; except ELW	
Radiometric Calibration:	<0.1K at 260 K; absolute <0.2K at 260 K; reproducibility	

Table 7. S-HIS Instrument Specifications.

The S-HIS utilizes a 45° scene mirror that rotates through a measurement sequence consisting of views of the earth and two calibration sources, one at ambient and another up to 60 K above ambient. The raw interferograms from each view are compressed in real time to reduce the volume of data. A numerical filter is applied using a digital signal processor (DSP), while a second DSP is used for controlling the instrument. The S-HIS uses calibration techniques that were developed for the HIS and AERI (Revercomb et al., 1988).

The retrieval and spectroscopic applications of the S-HIS data require high radiometric accuracy. The RMS noise level in terms of brightness temperature for the AERI and HIS instruments is generally less than 0.2 K, except near the edges of spectral bands and in some localized spectral regions. The performance of the S-HIS is comparable for its shorter dwell time, except for the extra longwave (ELW) band which requires longer averaging times for comparable performance.

For the S-HIS system, variable wavefront tilts caused by external vibrations create radiometric uncertainties from both interferogram amplitude modulation and from sample-position errors. Correction for these effects can in principle be accomplished using measurements from the dynamic alignment system that characterize the tilt jitter during an interferogram scan. We have implemented a system to record wavefront phase errors (along the dynamic alignment x and y-axes) for every eighth interferogram sample (close to 8,350 Hz). This sampling results in a Nyquist frequency of about 4.2 kHz, but the system has an analog filter with a 2 kHz cut-off to suppress noise aliasing. The highest resonant frequencies observed in recent tests using this system occur in the region 1.2–1.4 kHz. The primary resonances are largely contained between 290 and 650 Hz.

The S-HIS instrument has flown aboard both NASA's DC-8 research and on NASA's ER-2 aircraft during several field campaigns. It has the potential to fly on a UAV and other aircraft in the future as opportunities arise. Figure 9 illustrates the S-HIS instrument and the aircraft platforms used.

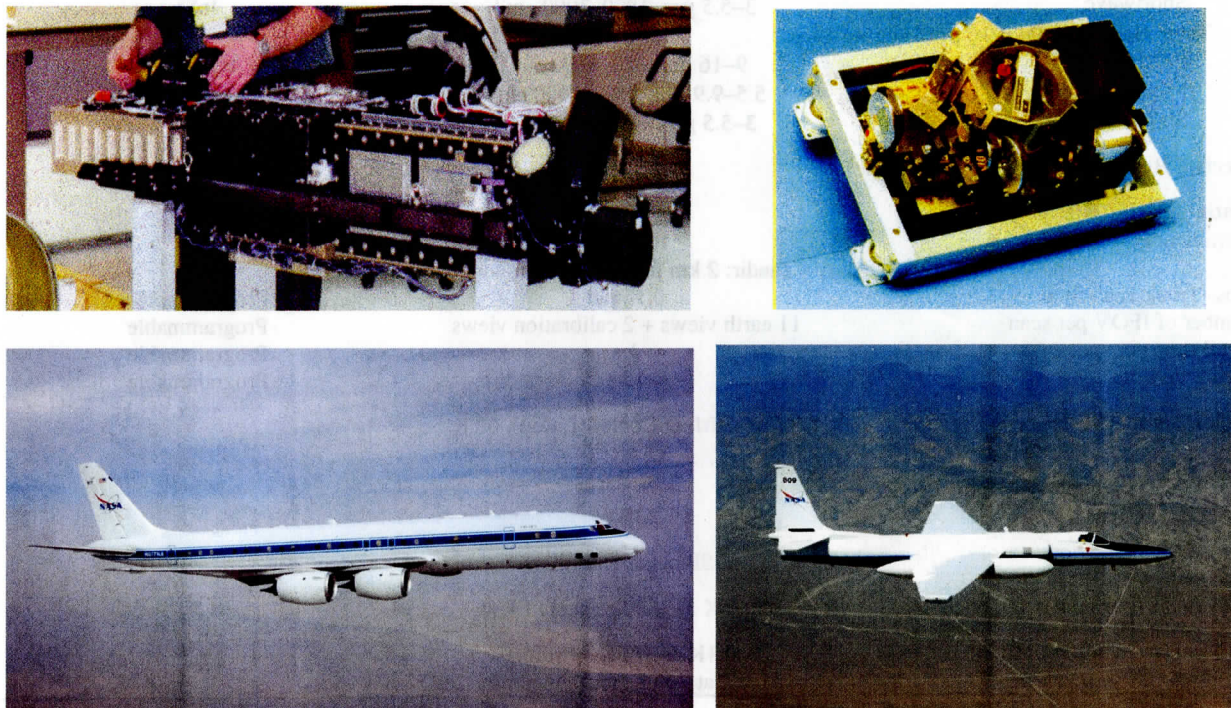


Figure 9. S-HIS instrument (upper left). S-HIS interferometer (upper right). NASA DC-8 (lower left). NASA ER-2 (lower right). Aircraft photographs courtesy of NASA.

2.7.2.1 Bomem Dynamic Alignment Mirror Mechanism Modifications

The following modifications were made to the Dynamic Alignment mechanism to reduce its sensitivity to aircraft vibration.

- Redesigned the D/A mechanism cover so that the voice coil magnets (mirror actuators) mount to it rather than to the mirror support plate. This eliminates the problem of the voice coils being supported on a mechanically soft structure and also reduces the coupling between the magnet portion of the actuator and the mirror.
- Stiffened the mirror support plate by eliminating the cantilevered sections.

- Glued damping plates on both of the above parts (cover and support plate) to attenuate vibrations.
- Mounted the voice coil magnets using damping materials to attenuate vibrations.
- Installed tip-tilt adjustment screws with finer threads to make static mirror alignment more precise.

Figure 10 illustrates the original and modified mechanism design.

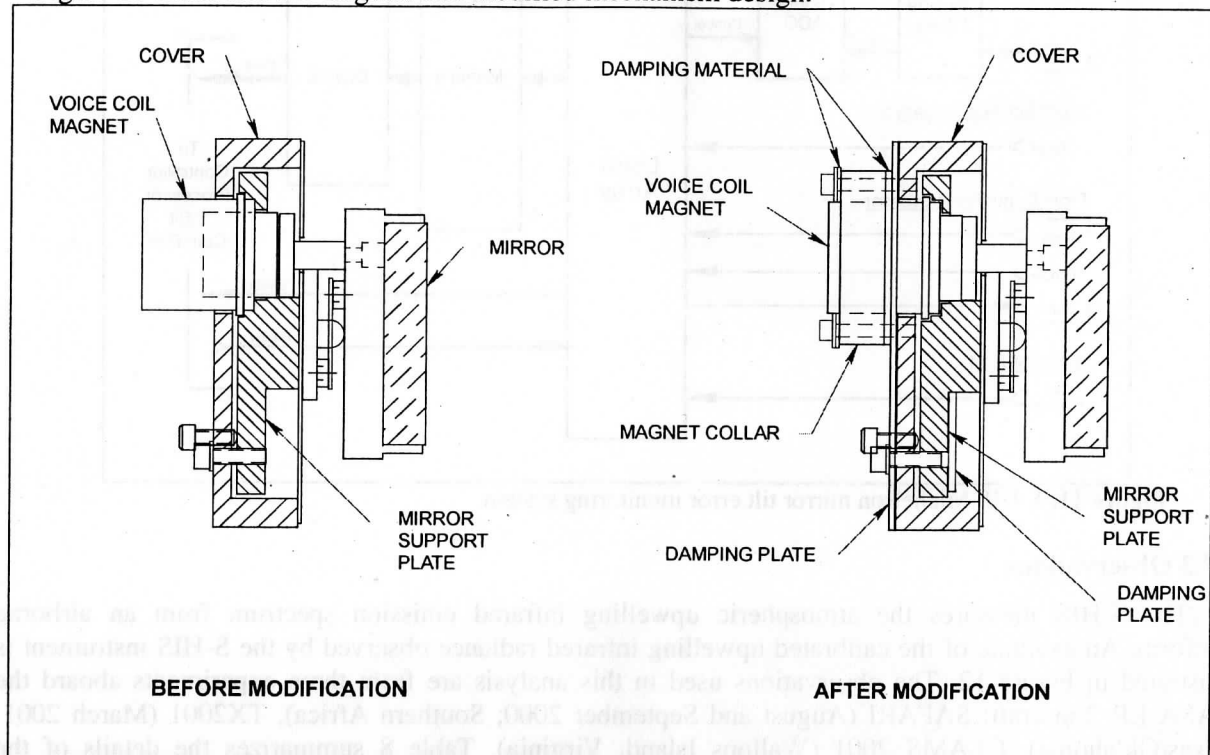


Figure 10. Original (left) and modified (right) configurations of the Bomem Dynamic Alignment Mirror Mechanism. The new configuration is stiffer and has increased levels of damping, making it less sensitive to vibrations.

2.7.2.2 Tilt Board General Description

The Tilt Board circuit samples and digitizes the Dynamic Alignment (DA) X & Y error signals. The bandwidth of the DA system is limited and vibration to the system may result in significant residual alignment errors. The DA X & Y error signals are generated by the interferometer control circuitry to provide feedback for the DA system. The DA X and Y error signals are taken from the two phase detector outputs and provide signals which are proportional to the residual alignment errors. The phase detector outputs are filtered and then digitized by the Tilt Board. The Tilt Board DA X & Y error signal sampling is synchronized to the sampling of the detectors. Mechanical tilt of the DA mirrors is measured with a resolution of approximately 0.003 microradians.

The Tilt Board's functionality is controlled by an FPLA (Field Programmable Logic Array). This FPLA handles communication (data and status) with the SHIS Controller Processor. The FPLA also provides the synchronization between the interferometer control signals and the 16 bit Analog to Digital Converter. The alignment error signals are sampled every 8th detector sample. The first sample can be offset by 0 to 31 detector samples. The SHIS Controller processor passes the Tilt Board data and status information to the SHIS data storage computer.

Figure 11 provides a schematic of the S-HIS tilt monitoring system electronics.

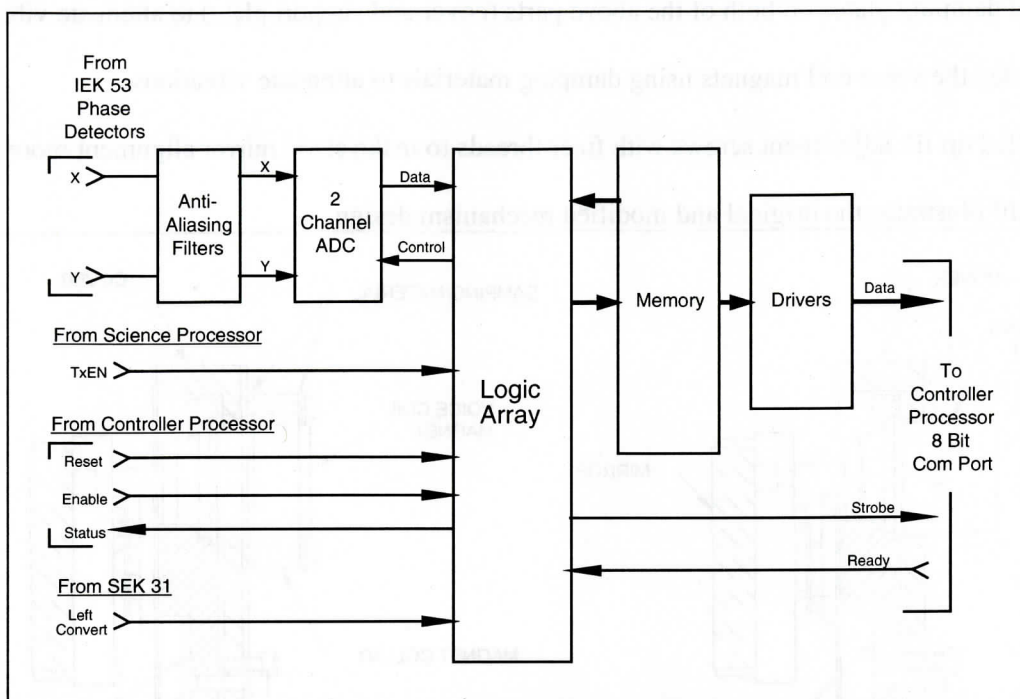


Figure 11: S-HIS Michelson mirror tilt error monitoring system.

2.7.3 Observations

The S-HIS measures the atmospheric upwelling infrared emission spectrum from an airborne platform. An example of the calibrated upwelling infrared radiance observed by the S-HIS instrument is illustrated in Figure 12. The observations used in this analysis are from three experiments aboard the NASA ER-2 aircraft: SAFARI (August and September 2000; Southern Africa), TX2001 (March 2001; Texas/Oklahoma), CLAMS 2001 (Wallops Island, Virginia). Table 8 summarizes the details of the observation periods analyzed. All of these cases make use of a new linear drive mechanism using a sliding carriage for the Michelson moving mirror.

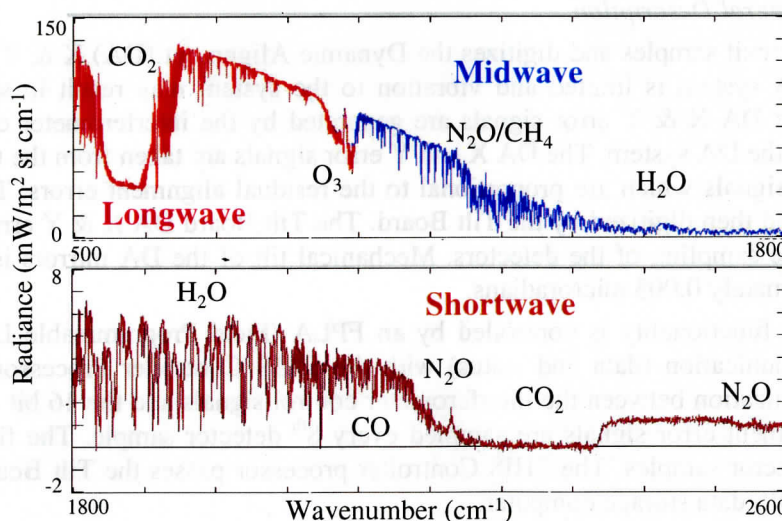


Figure 12. S-HIS observation of upwelling infrared radiance at about 20 km altitude aboard the NASA ER-2 aircraft on 24 August 2000 during the SAFARI experiment in Southern Africa.

ID	Date (UTC)	Time (UTC)	Filename	Comment
SAFARI-1	6 Aug 2000	15:46:33	ddgzgaz.rsh	Early in flight. Ferry to Florida.
SAFARI-2	6 Aug 2000	18:48:19	ddgzwel.rsh	Late in flight. Ferry to Florida.
SAFARI-3	8 Aug 2000	13:38:31	ddhiqhr.rsh	Early in flight. Ferry to Brazil. Pod aperture covered. No air dam.
SAFARI-4	8 Aug 2000	16:39:28	ddhjgig.rsh	Late in flight. Ferry to Brazil. Pod aperture covered. No air dam.
TX2001-1	22 Mar 2001	17:55:02	deycmhe.rsh	Early in flight.
TX2001-2	22 Mar 2001	20:42:09	deydbcr.rsh	Late in flight.
CLAMS-1	21 Jul 2001	14:36:12	dfuypsm.rsh	Early in flight.
CLAMS-2	21 Jul 2001	16:29:52	dfuyzuu.rsh	Late in flight.

Table 8. Observation periods used in this analysis. Each file is named using a base-26 representation of time in units of number of seconds since 00:00 Jan 1, 1970.

2.7.4 Analysis

The analysis of the S-HIS observations presented in this report will focus on the relationship between the total power contained in the measured mirror tilt error and the corresponding interferometric errors found in the calibrated radiance. The cases analyzed are those shown in Table 8.

For each half-hour case, the mean of the magnitude of the Fourier transform of the measured tilt error was computed for each mirror tilt axis, along with the standard deviation over the case time period and the integral of the mean frequency spectrum (excluding zero frequency). The root sum square of the frequency integrals for each axis are given in Table 9.

Each case was also processed using the standard S-HIS ground processing algorithm to compute calibrated radiance spectra. The calibrated spectra for the on-board hot blackbody views were chosen for this analysis because of the stability of the scene and the known temperature of the source. Statistics for the error between the calibrated radiance of each hot blackbody view and the corresponding calculated radiance (using a Planck function and measured BB temperatures) include a radiance error standard deviation for the spectrally correlated, spectrally uncorrelated, and total noise. The spectrally correlated error is obtained by smoothing the radiance error spectrum using a fixed correlation length (about 10 cm⁻¹) and computing a standard deviation over a time series of spectra. The uncorrelated error estimate is obtained by differencing the spectrally smooth error from the original and computing a standard deviation over a time series of spectra. The assumption for this report is that the uncorrelated error is due to detector noise and the correlated error is due to uncompensated Michelson interferometer mirror wavefront tilt errors. The ratio of the total radiometric noise spectrum to the uncorrelated noise spectrum is used as a measure of the size of the vibration-induced tilt error impact on the calibrated data. A ratio of unity implies that there is no impact due to vibration-induced tilt. Table 9 provides a tabulated summary of the noise ratio for selected wavenumber ranges (in cm⁻¹).

Date YYMMDD	File ID	Mirror Tilt Integral	HBB Noise Ratio (Total Noise/Uncorrelated Noise)								
			LW1 650– 660	LW2 850– 860	LW3 950– 960	MW1 1050– 1060	MW2 1180– 1190	MW3 1500– 1510	SW1 2000– 2010	SW2 2400– 2410	SW3 2800– 2810
000806	ddgzgaz	153640	2.67	3.21	2.62	6.34	6.40	3.82	1.95	1.43	1.05
000806	ddgzwel	148180	2.30	1.71	1.77	4.39	1.44	2.28	1.01	1.00	1.00
000808	ddhiqhr	62474	1.21	1.05	1.07	1.49	1.06	1.09	1.04	1.02	1.00
000808	ddhjghj	64000	1.25	1.05	1.08	1.62	1.05	1.10	1.10	1.03	1.00
010322	deycmhe	90433	1.59	1.11	1.23	2.00	1.09	1.28	1.07	1.03	1.00
010322	deydbcr	107510	2.15	1.25	1.49	3.22	1.35	1.67	1.39	1.12	1.01
010721	dfuypsm	73440	1.58	1.09	1.26	1.71	1.07	1.24	1.01	1.01	1.00

010721	dfuypsm	73440	1.58	1.09	1.26	1.71	1.07	1.24	1.01	1.01	1.00
010721	dfuyzuo	134540	3.32	4.12	2.85	5.43	5.73	2.91	5.68	3.51	1.30

Table 9. Summary of S-HIS interferometer mirror tilt analysis comparing the integral of the mirror tilt frequency to an estimate of the vibration-induced tilt noise based on views of the on-board hot blackbody. The noise ratios are presented for selected wavenumber regions.

The HBB noise ratio from the longwave end of each spectral band (LW1, MW1, and SW1) is shown in Figure 13 versus the integrated mirror frequency spectrum. Figures 14–17 provide detailed plots of each of the observed cases. The following conclusions can be drawn from these figures and Table 9:

- The longwave and mid-wave S-HIS bands are both affected by sample position error. This is evidenced by a decrease in the noise ratio in the center of each band compared to the ends of each band. Sample position errors lead to a rocking of the spectrum. This is consistent with the detector geometry which places each of these detectors off-axis by a similar amount. The nonlinear dependence shown in Figure 13 suggests that modulation error may become important at high vibration levels.
- Relative to the background detector noise, the impact of sample position error is larger on the mid-wave band than the long-wave band. Presumably this is due to better detector signal to noise in the mid-wave band than exists in the longwave band.
- The shortwave S-HIS band is less sensitive to the vibration-induced tilt errors. This is consistent with the known detector geometry (symmetrical about the optic axis) which makes it relatively immune to sample position errors.
- The best performance was obtained in cases where the S-HIS viewport was closed during flight. This suggests that the source of the vibration is related to turbulent airflow in and around the S-HIS viewport. Additional steps need to be considered to reduce the source of this vibration or better isolate the instrument from this vibration source.

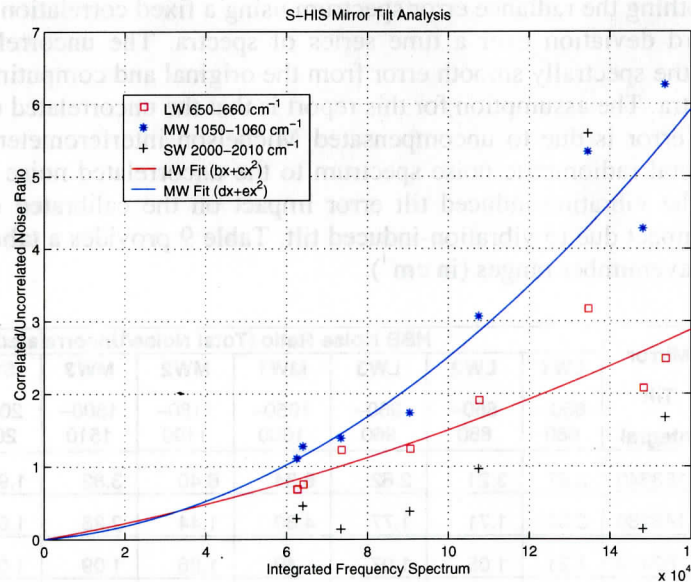


Figure 13. S-HIS correlated noise ratio for the LW1, MW1, and SW1 cases shown in Table 9. The LW and MW band measurements (symbols) show reasonable agreement with a linear plus quadratic dependence. The SW band measurements require further analysis to screen out cases containing noise unrelated to tilt errors.

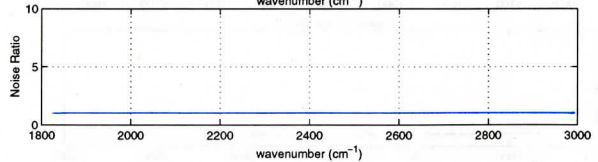
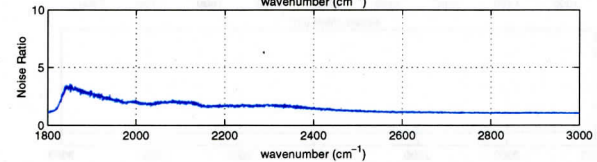
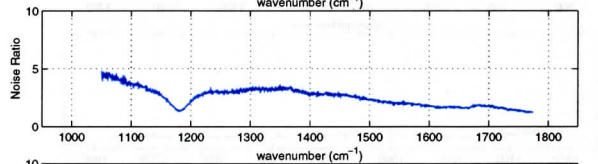
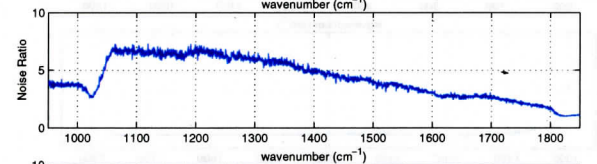
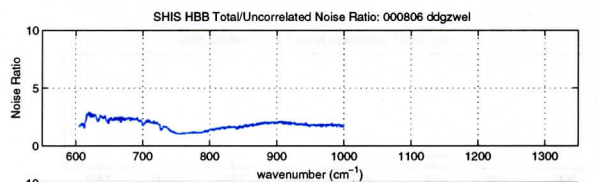
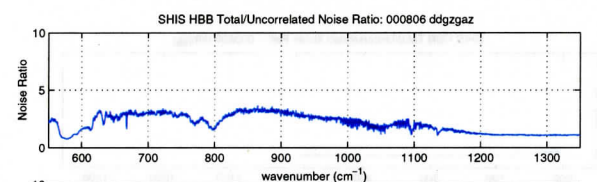
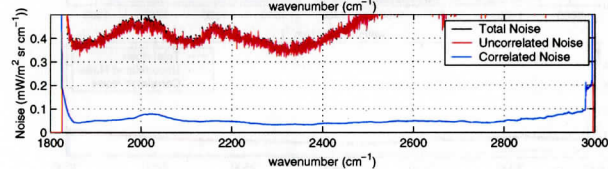
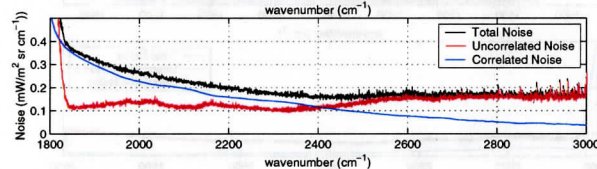
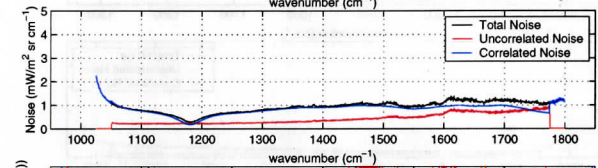
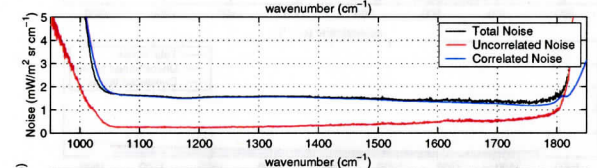
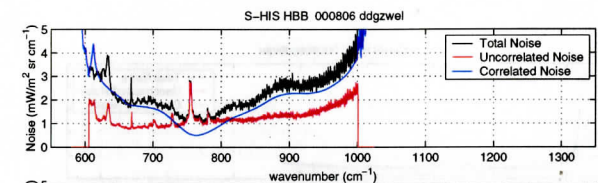
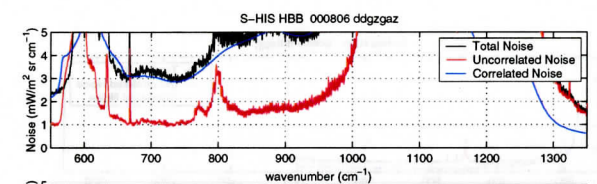
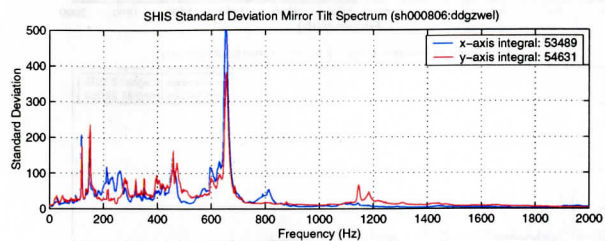
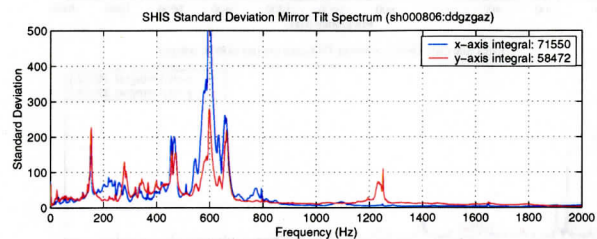
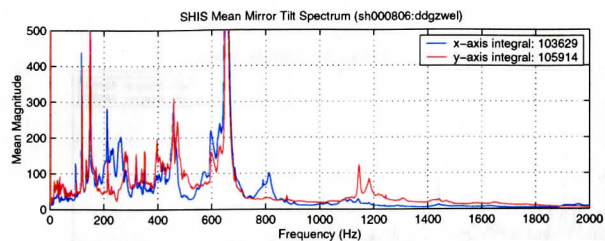
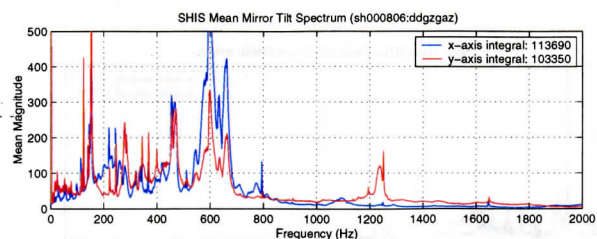


Figure 14: S-HIS tilt analysis for SAFARI-1 (left) and SAFARI-2 (right) cases from 6 August 2000. From top to bottom: Tilt frequency spectrum, HBB radiometric noise estimates, and noise ratio (Total/Uncorrelated).

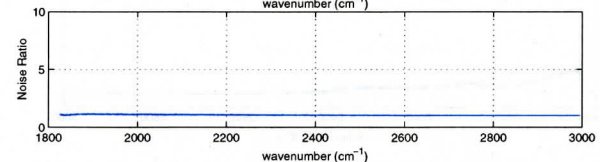
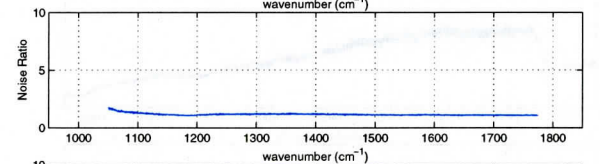
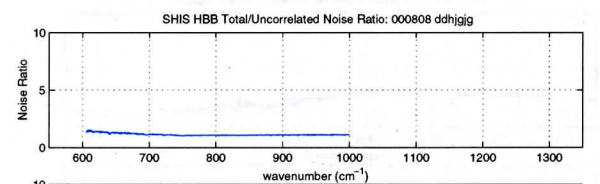
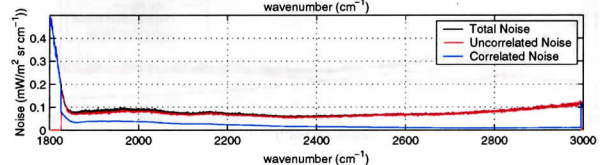
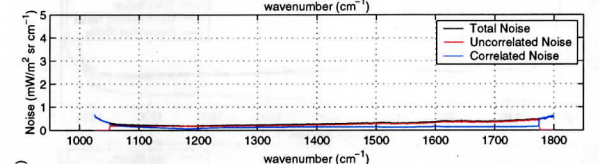
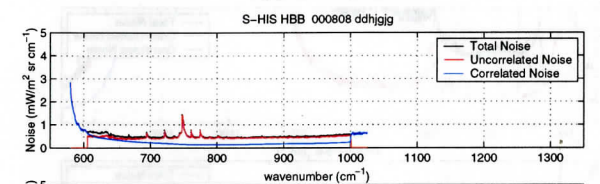
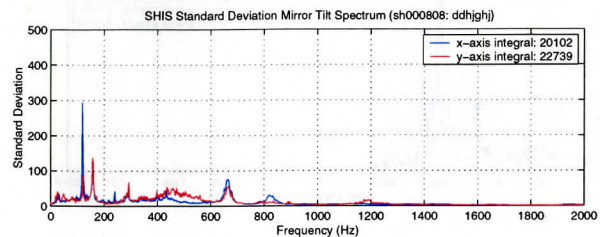
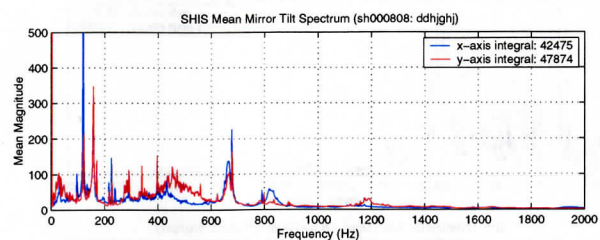
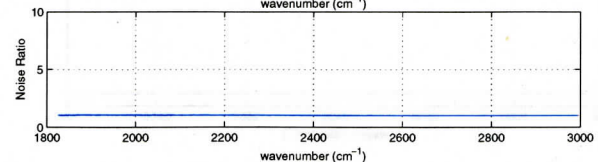
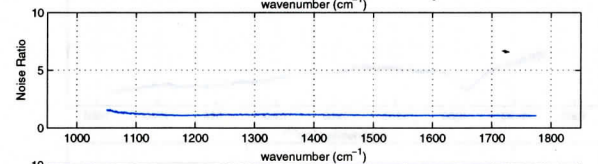
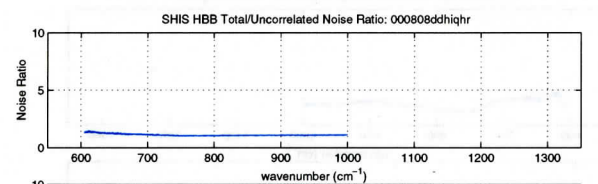
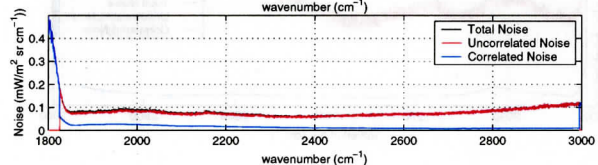
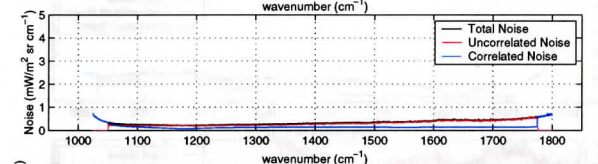
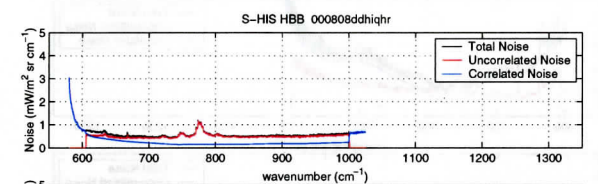
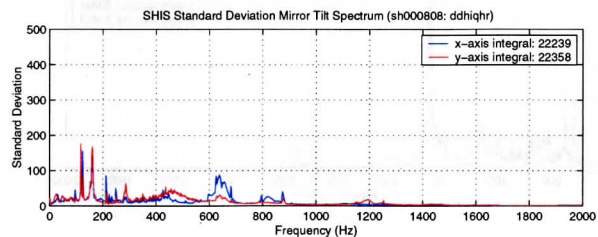
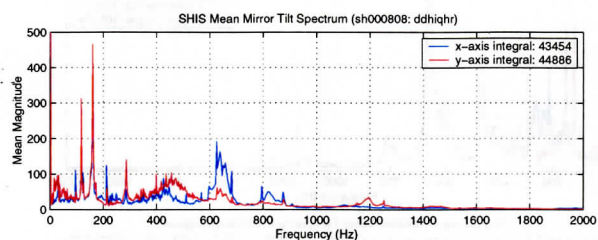


Figure 15: S-HIS tilt analysis for SAFARI-3 (left) and SAFARI-4 (right) cases from 8 August 2000. From top to bottom: Tilt frequency spectrum, HBB radiometric noise estimates, and noise ratio (Total/Uncorrelated).

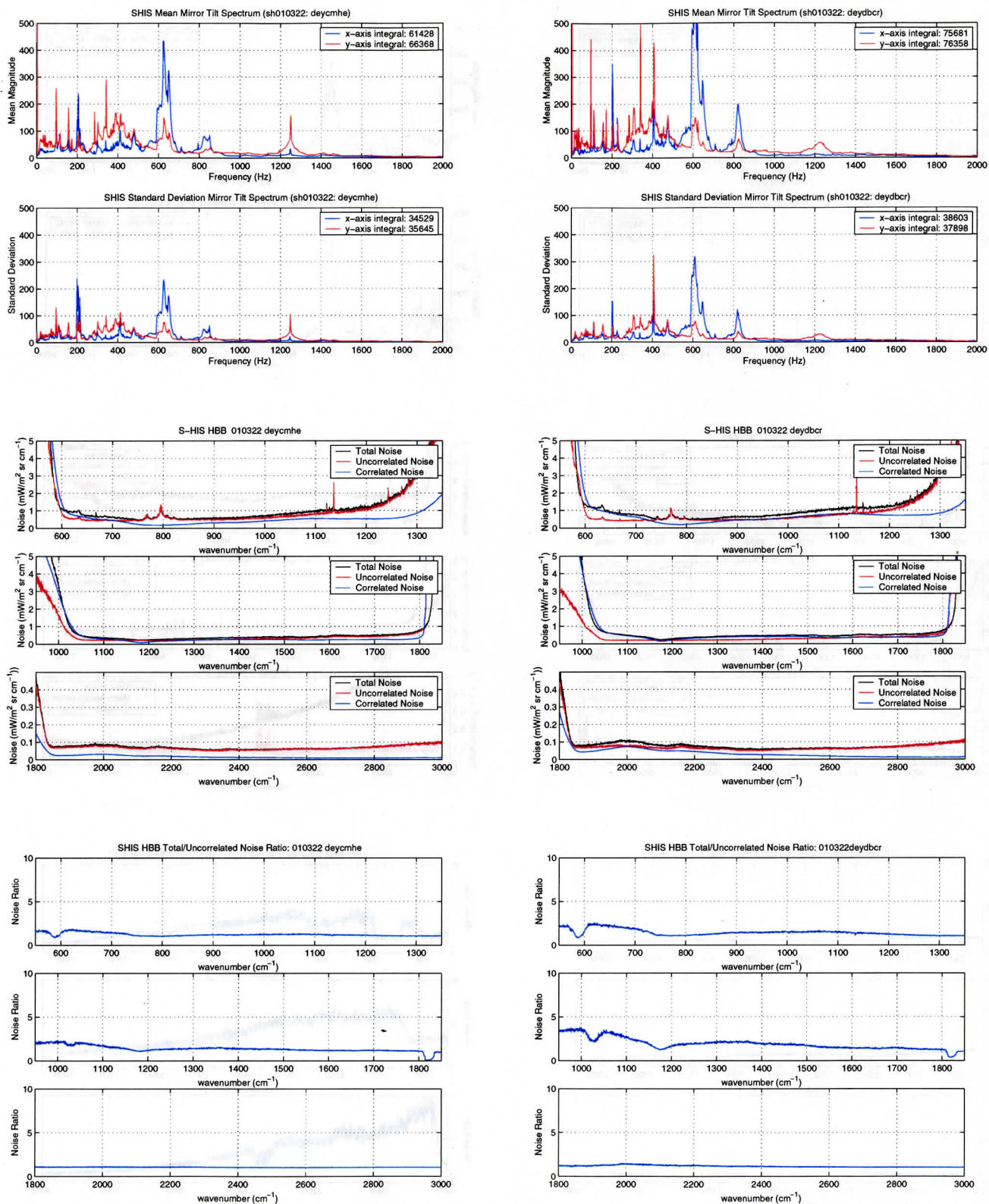


Figure 16: S-HIS tilt analysis for TX2001-1 (left) and TX2001-2 (right) cases from 22 March 2001. From top to bottom: Tilt frequency spectrum, HBB radiometric noise estimates, and noise ratio (Total/Uncorrelated).

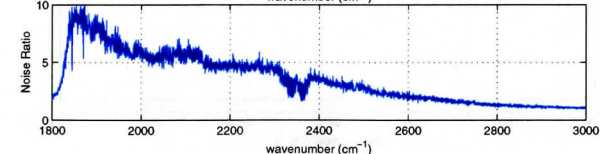
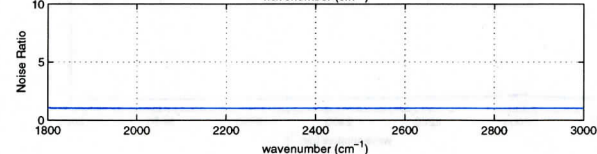
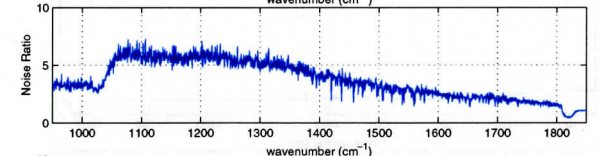
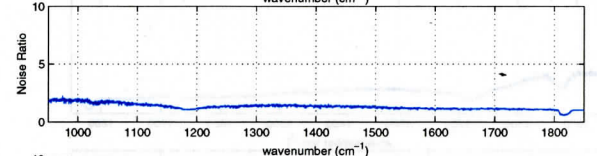
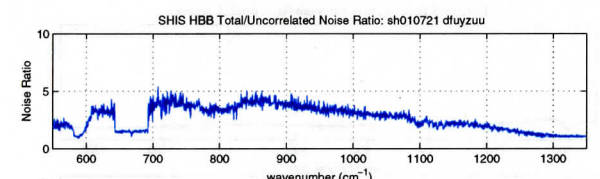
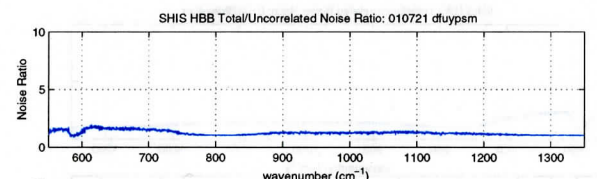
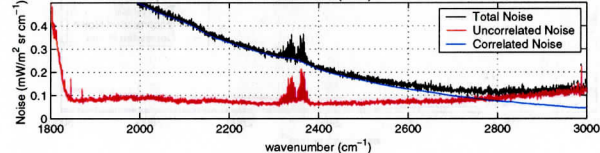
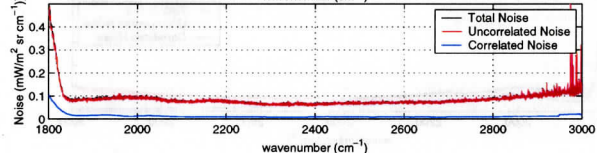
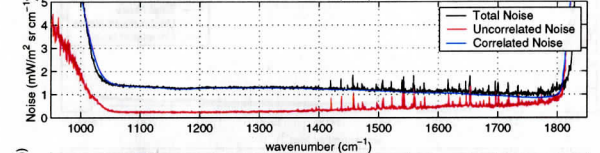
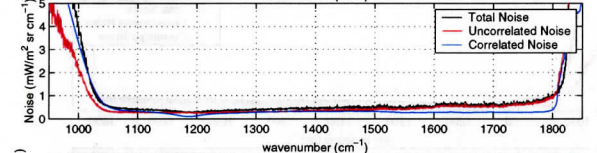
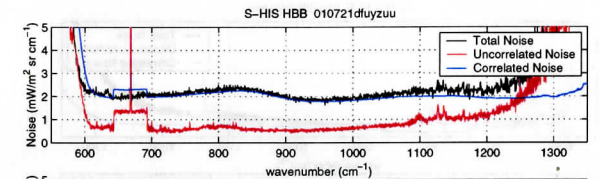
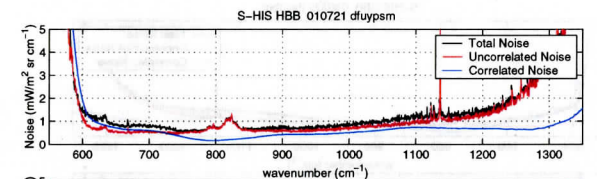
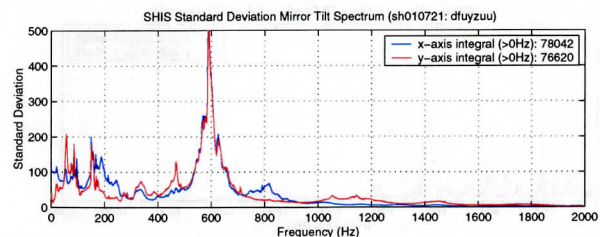
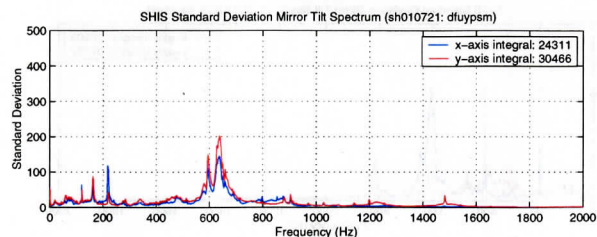
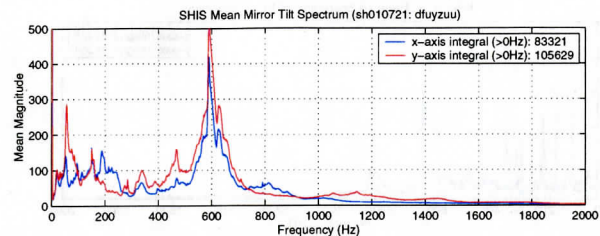
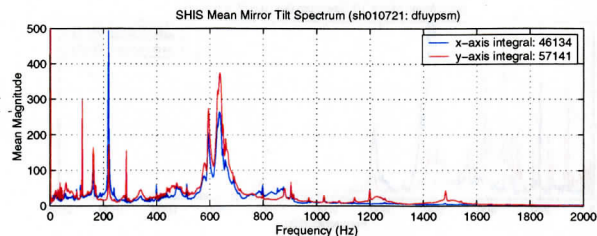


Figure 17: S-HIS tilt analysis for CLAMS-1 (left) and CLAMS-2 (right) cases from 21 July 2001. From top to bottom: Tilt frequency spectrum, HBB radiometric noise estimates, and noise ratio (Total/Uncorrelated)

3.0 Conclusions

This section contains statements summarizing any significant results, lessons learned, and suggestions for future activities.

- One of the most significant results accomplished under this contract was the integration of an electronic offset into the dynamic alignment system of both the S-HIS and the NAST-I to minimize the Michelson mirror static offset in each instrument. The NAST-I obtained significant benefit from this instrument modification evidenced by the improved performance in the CLAMS experiment compared to TRACE-P. The S-HIS benefit was more limited presumably because the error induced by static offset is much smaller than for NAST-I.
- To further improve the NAST-I two further modifications should be implemented, namely: i) improve the matching of the beamsplitter and compensator, and ii) apply a Dynamic Alignment modification similar to that which has been successfully applied to S-HIS. A tilt monitoring system like that on S-HIS should also be added to monitor performance and form the basis for residual tilt corrections. Further details are provided in Appendix C.
- The S-HIS performance was improved between SAFARI and CLAMS by several refinements made to the dynamic alignment system. However, vibration-induced "sample position error" noise still dominates over random detector noise in some spectral regions. The primary immediate thrust is to use the available tilt measurements to correct for residual errors. If adequate resources were available a major reduction in tilt errors could be accomplished by incorporating a new detector assembly with symmetrically aligned detectors for the LW and MW bands.

4.0 Publications

Antonelli, P., S. A. Ackerman, W. P. Menzel, A. Huang, B. A. Baum, W. L. Smith, "Retrieval of cloud top height, effective emissivity, and particle size, from aircraft high spectral resolution infrared measurements", presented at SPIE's Second International Asia-Pacific Symposium on Remote Sensing of the Atmosphere, Environment, and Space, Sendai, Japan, 9-12 October 2000.

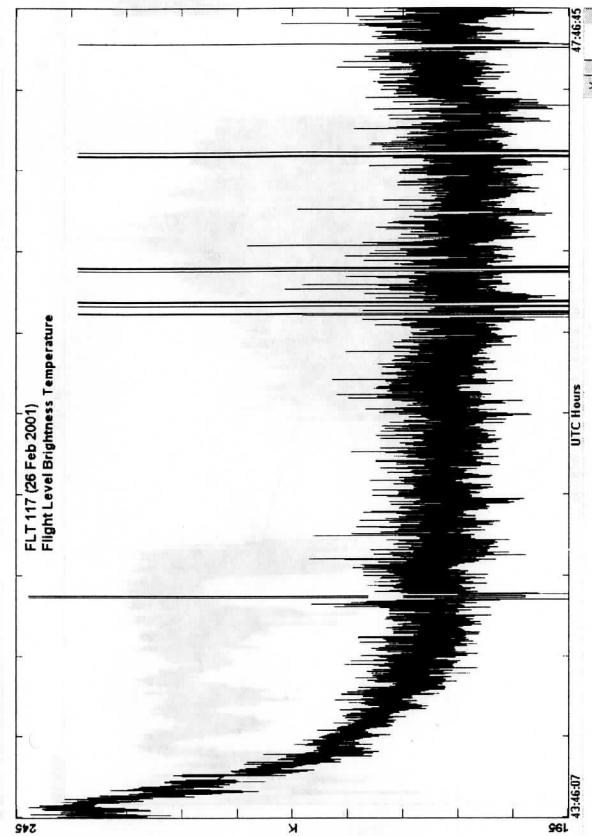
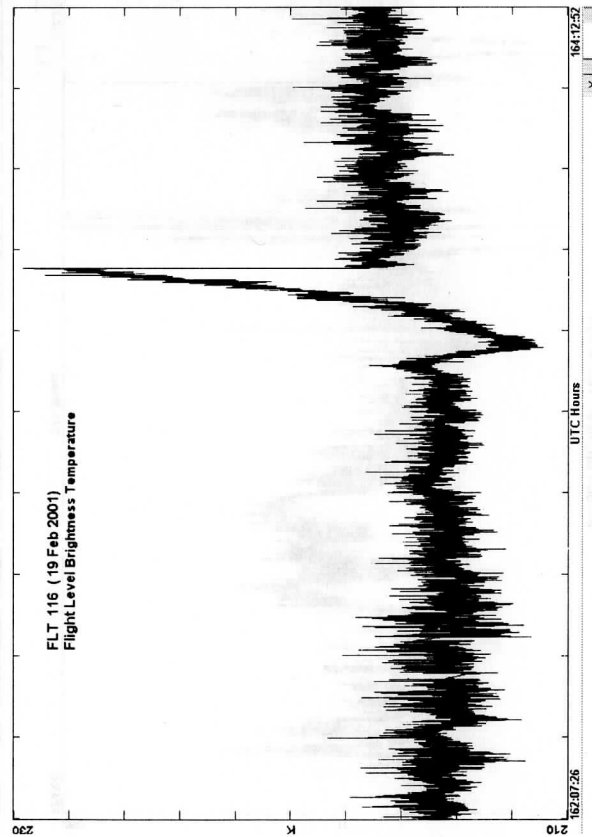
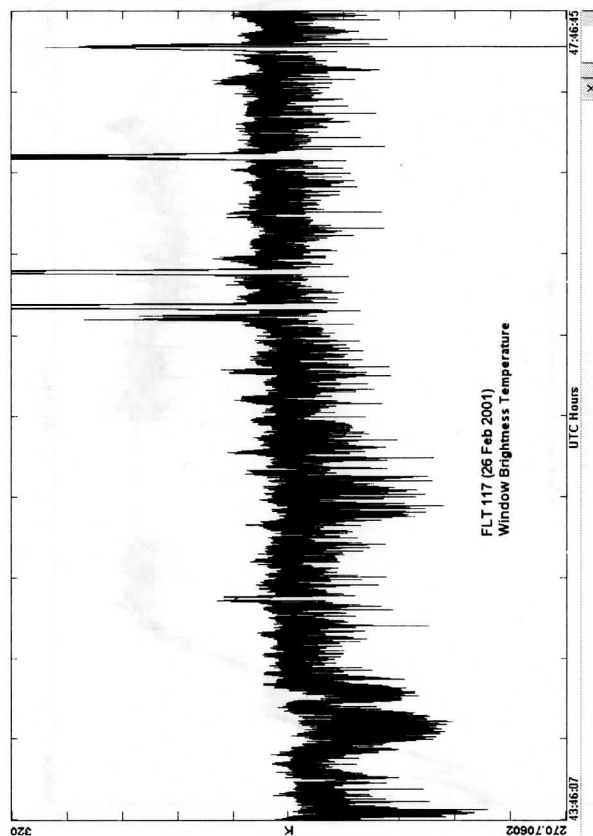
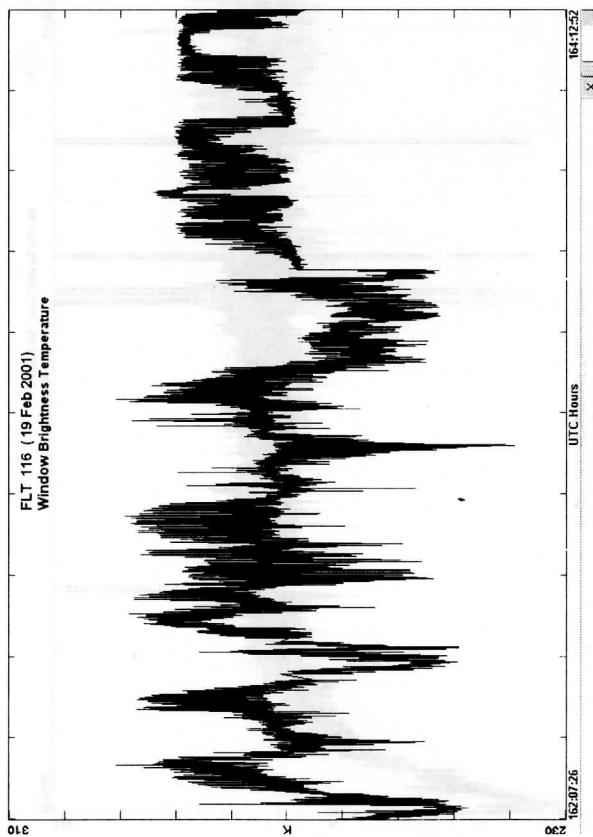
This paper is attached as Appendix D.

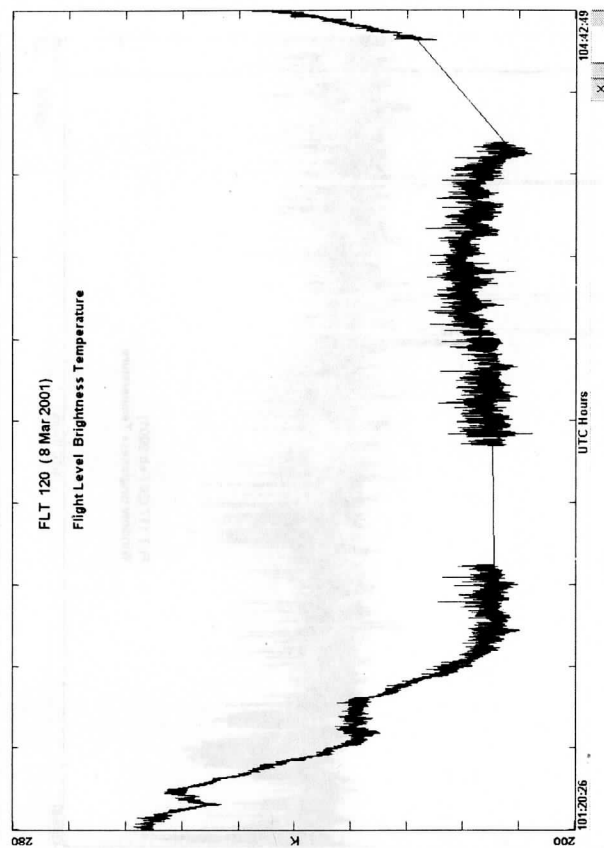
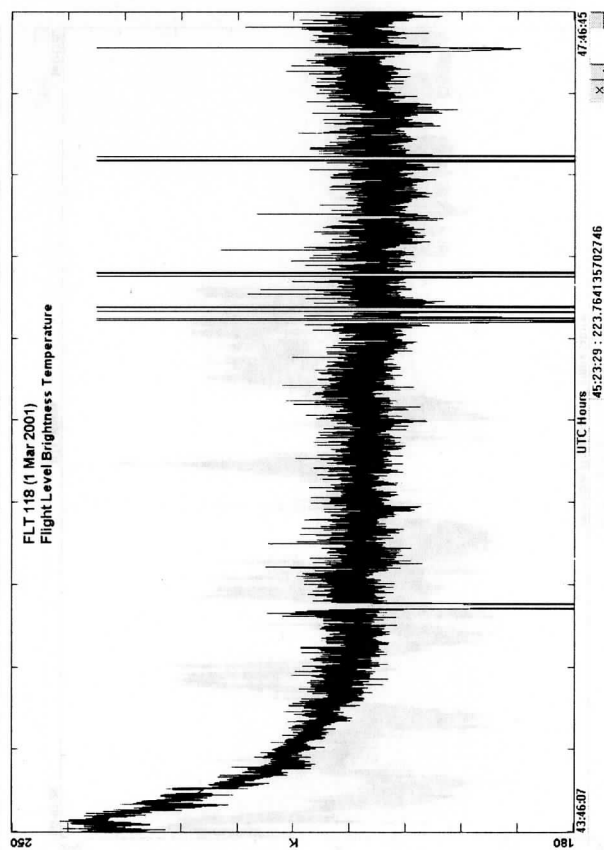
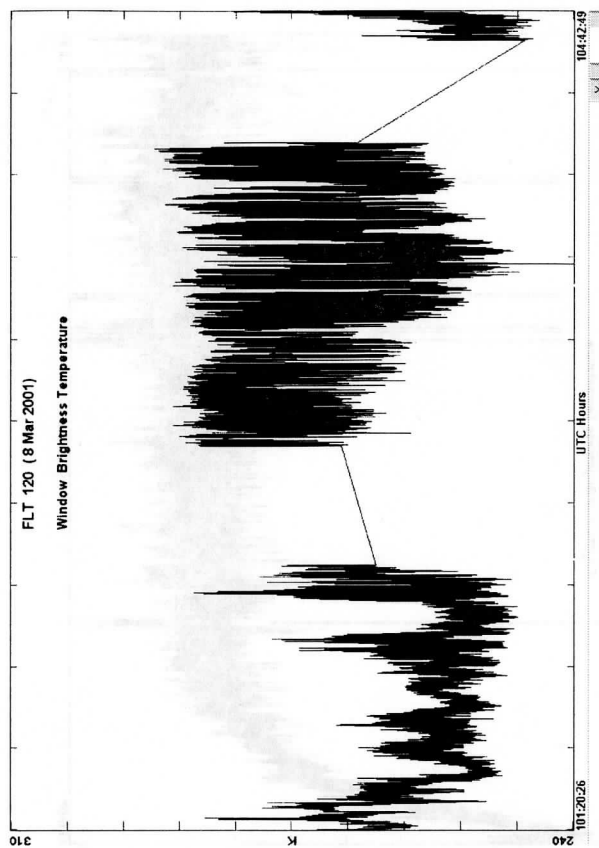
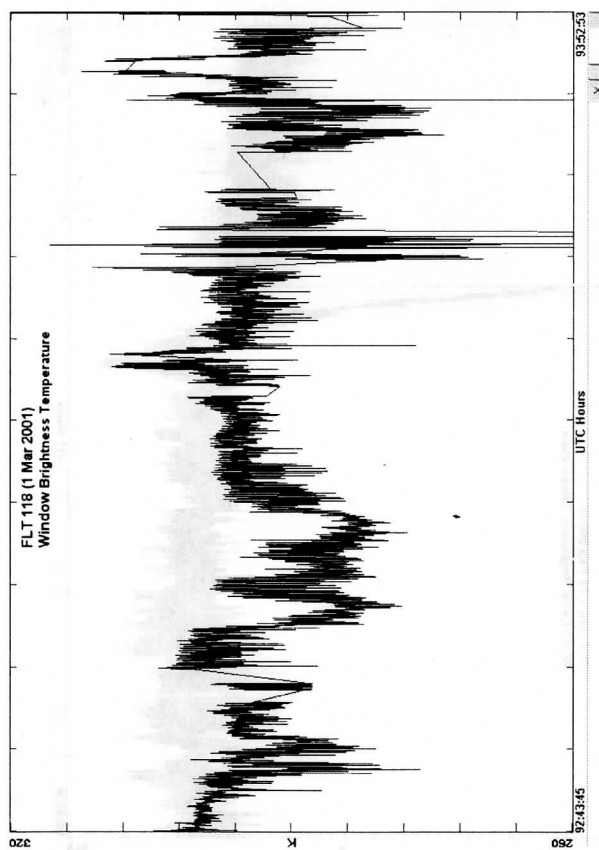
5.0 References

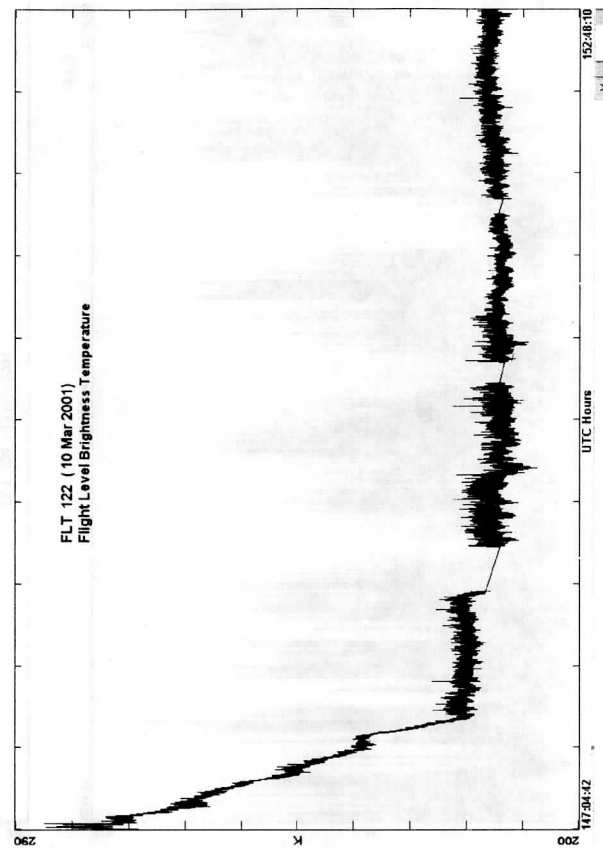
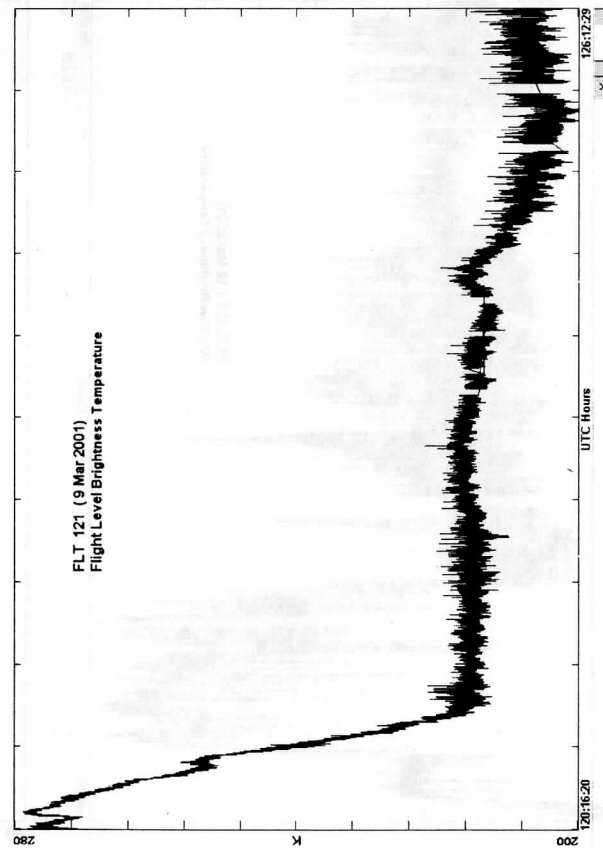
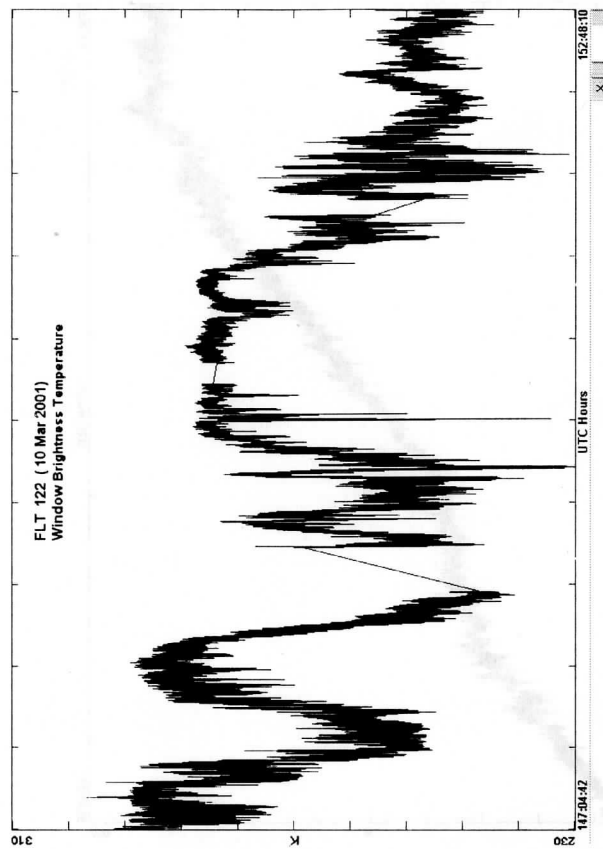
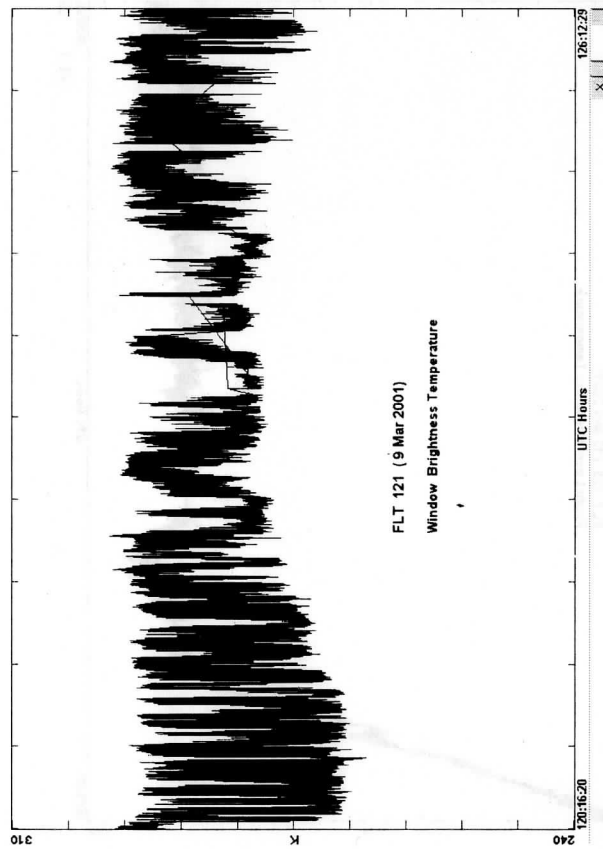
Revercomb, H. E., H. Buijs, H. B. Howell, D. D. LaPorte, W. L. Smith, and L. A. Sromovsky, 1988: Radiometric calibration of IR Fourier transform spectrometers: solution to a problem with the High-Resolution Interferometer Sounder. *Appl. Opt.*, **27**, 3210-3218.

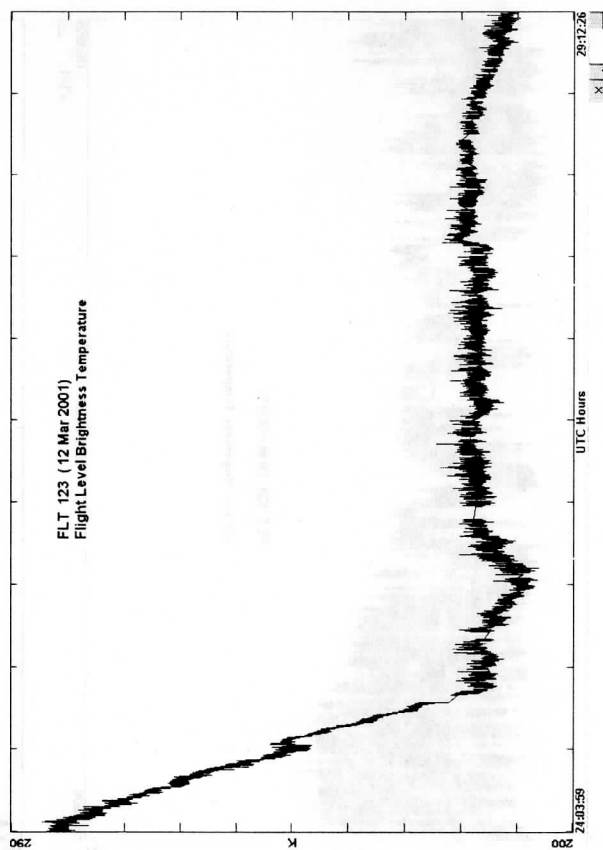
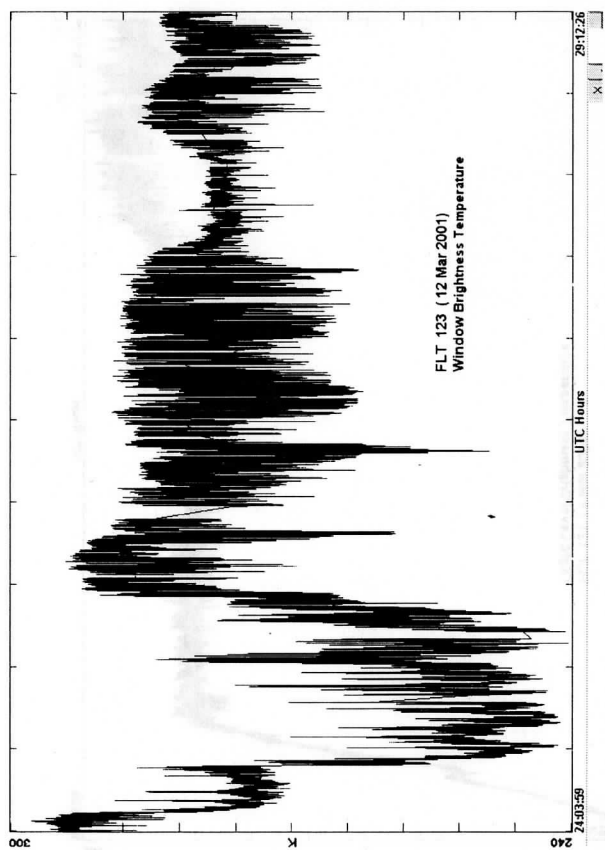
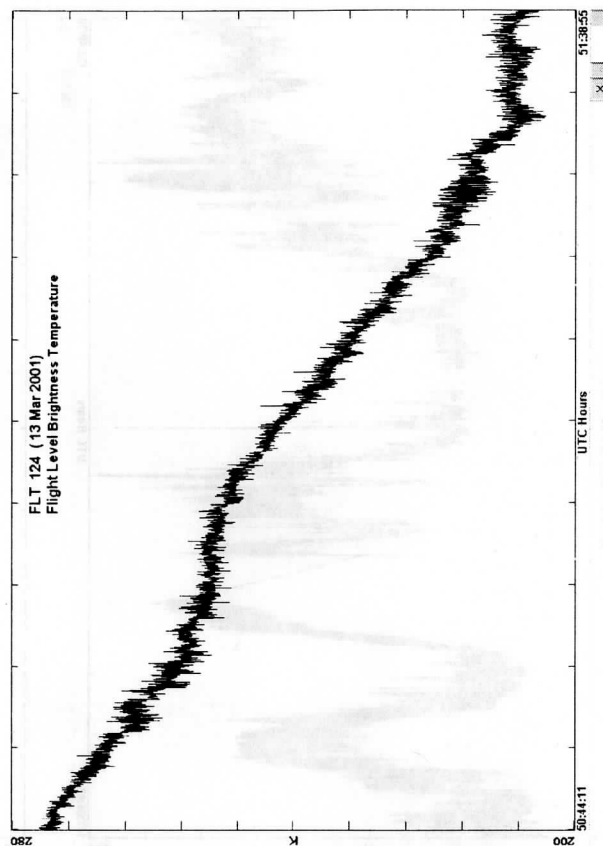
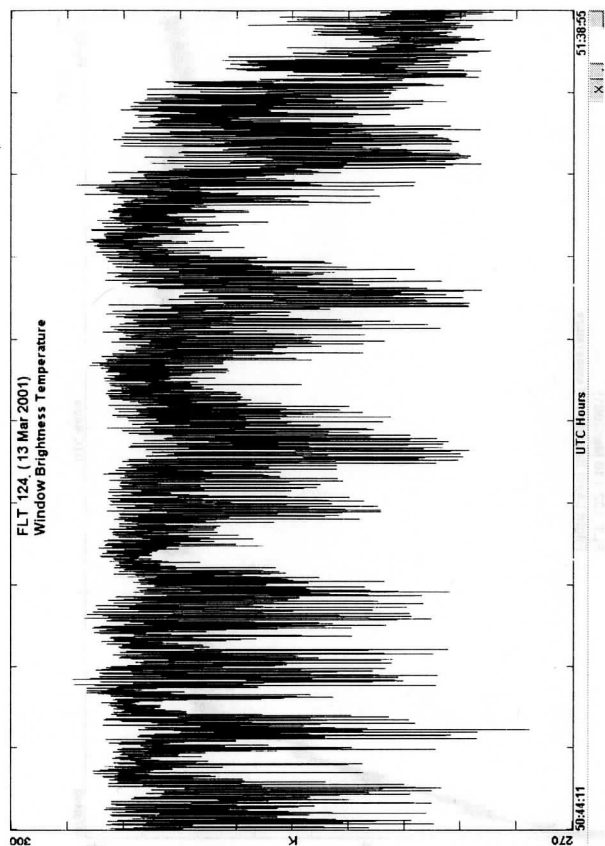
Appendix A: TRACE-P NAST-I Brightness Temperature Graphs

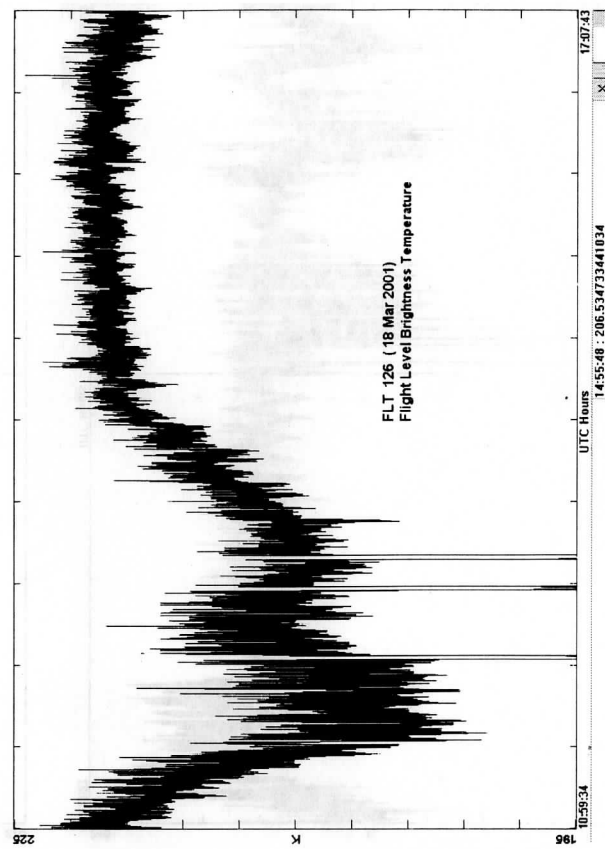
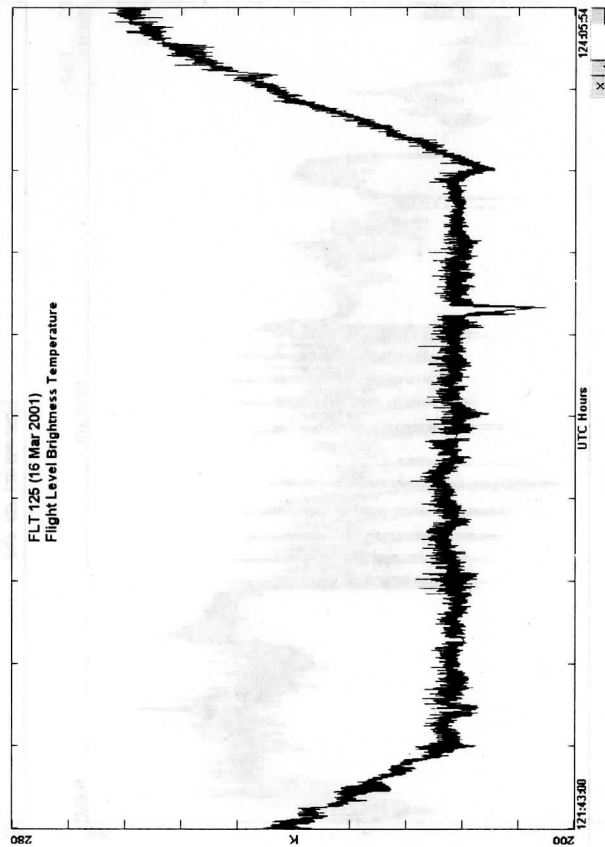
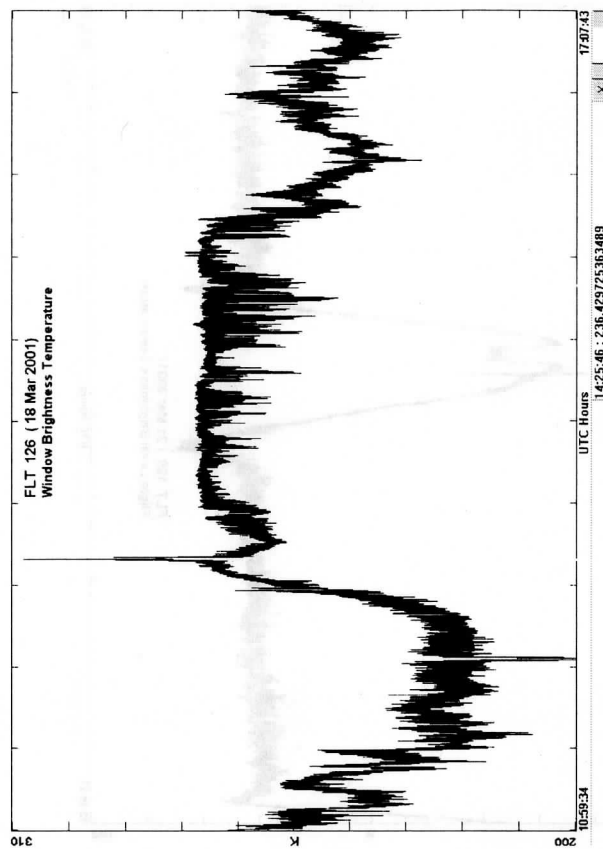
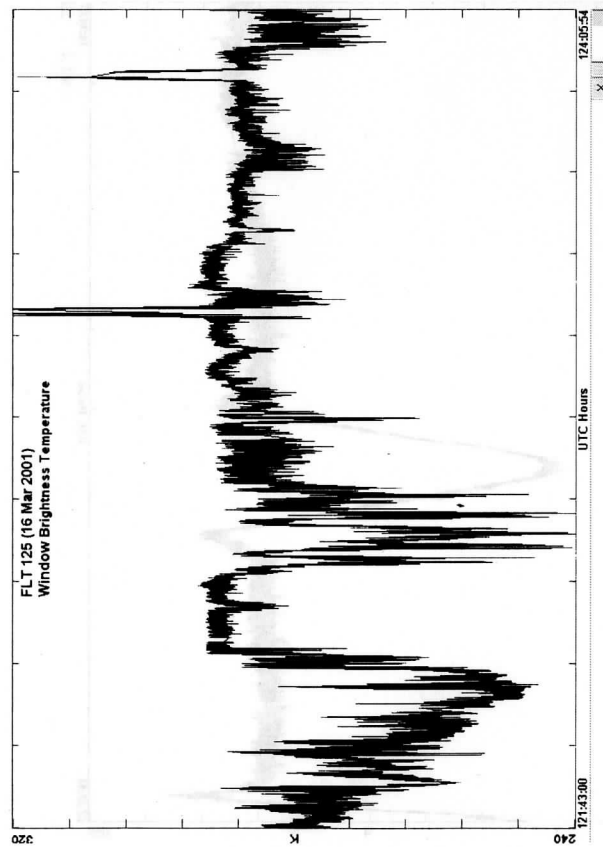
This appendix contains summary plots of the NAST-I data collected during the TRACE-P experiment. Plots are included of the longwave window channel equivalent brightness temperature ($10\text{ }\mu\text{m}$) and a flight level temperature ($15\text{ }\mu\text{m}$). The longwave infrared window channel shows the provides a coarse estimate of surface skin temperature (uncorrected for atmospheric effects) in clear skies or cloud top temperatures in the presence of clouds. The longwave infrared window channel plot is a useful "quicklook" to determine the regions of when clouds are present in the data. The flight level temperature clearly illustrates the data time periods when the aircraft is in ascent/descent or in level flight. The flight level temperature is generally insensitive to the presence of clouds.

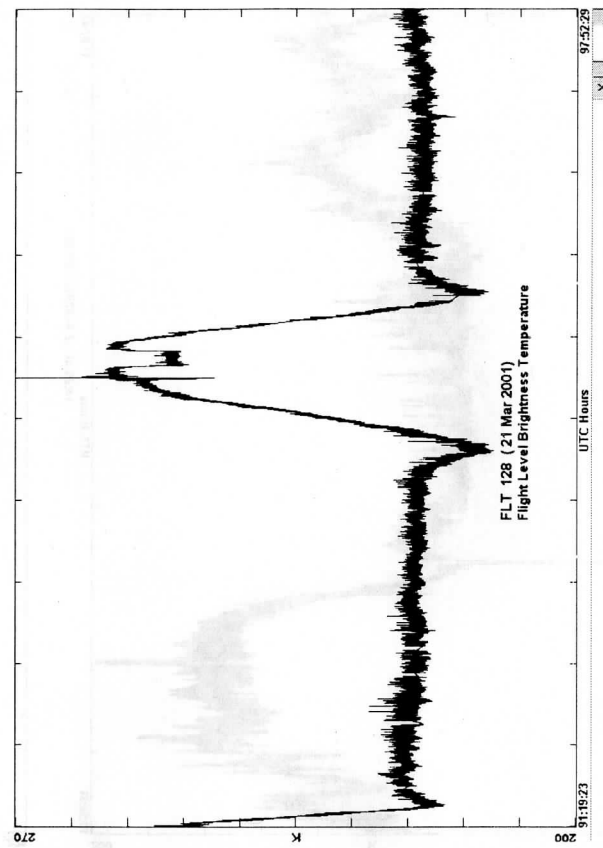
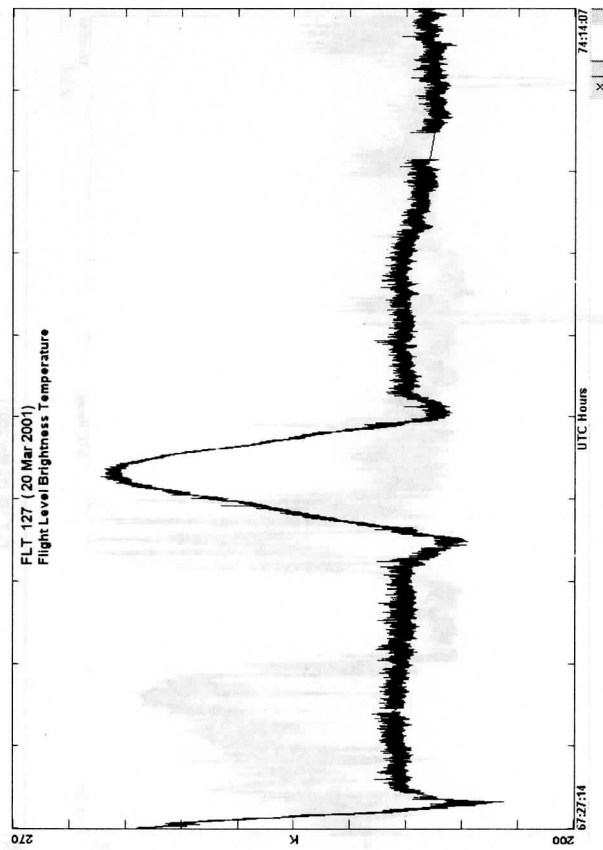
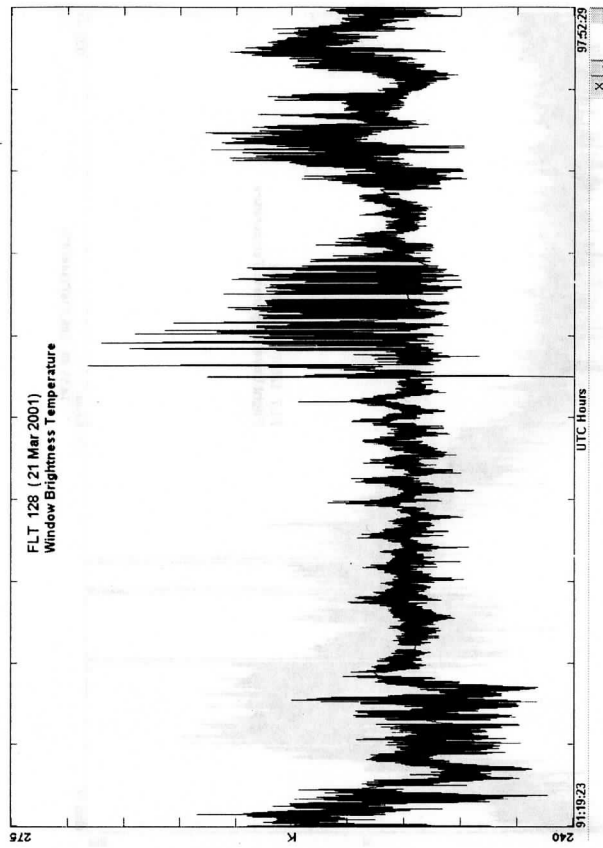
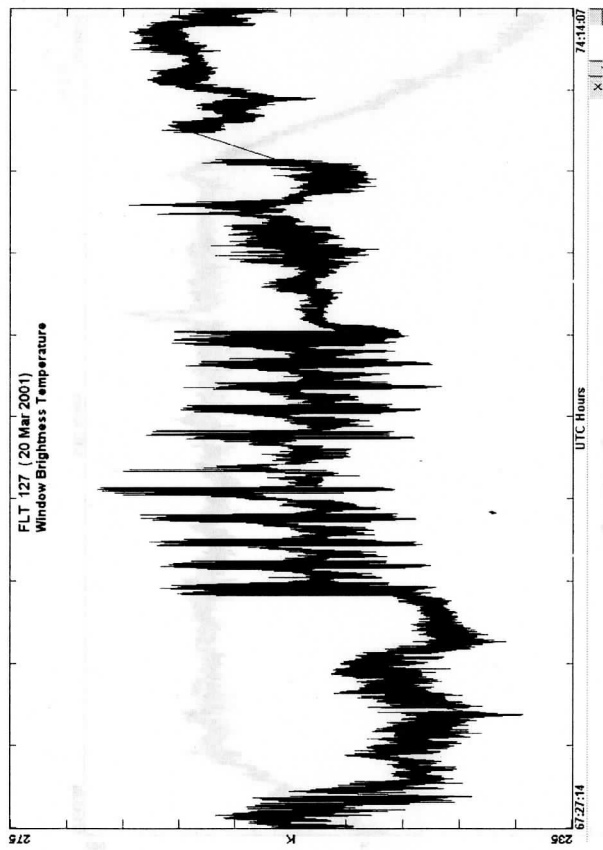


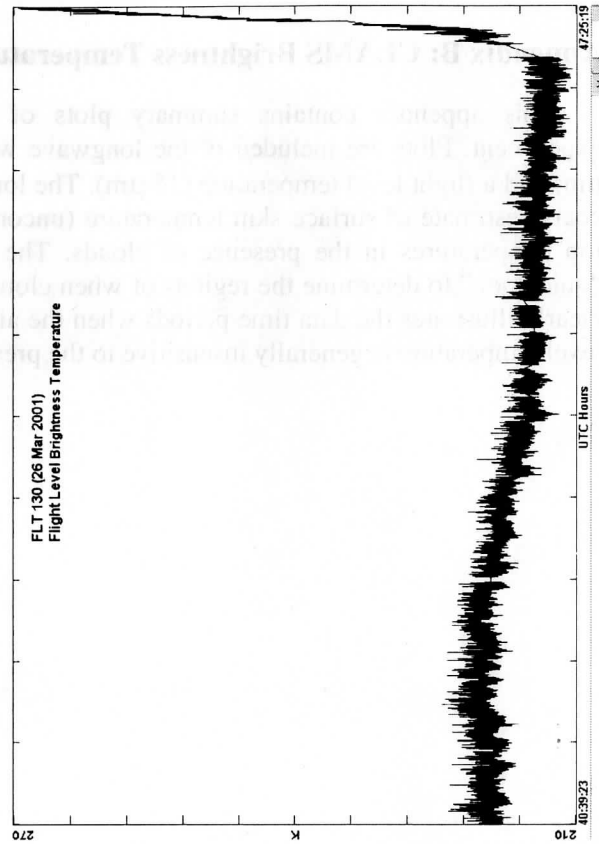
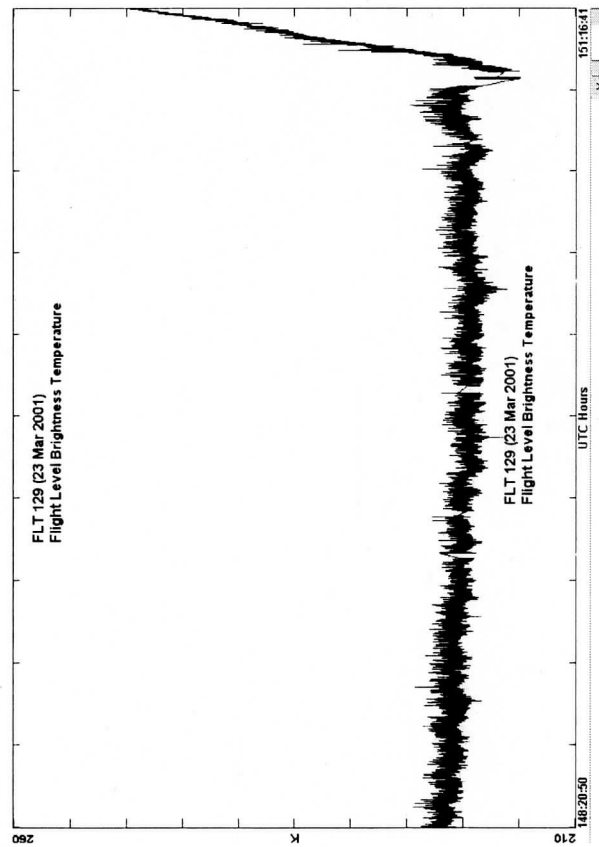
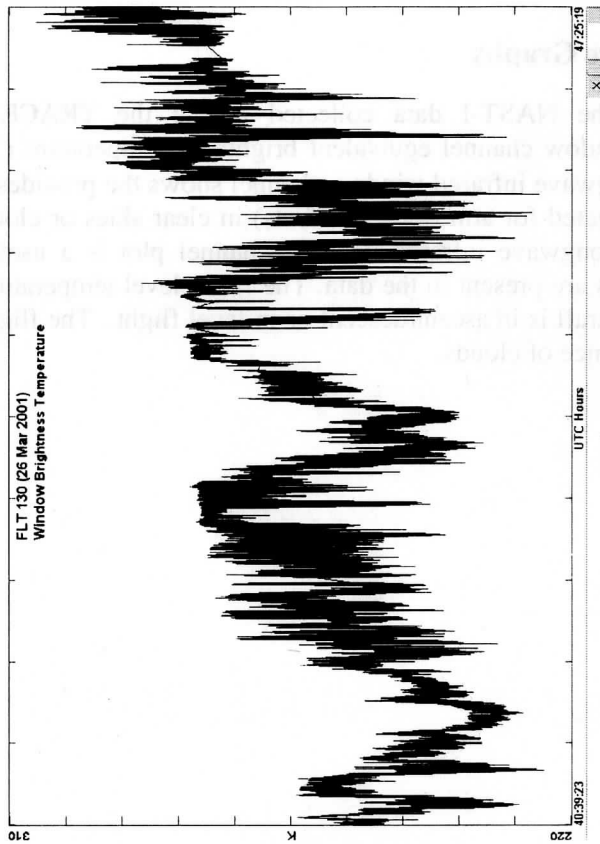
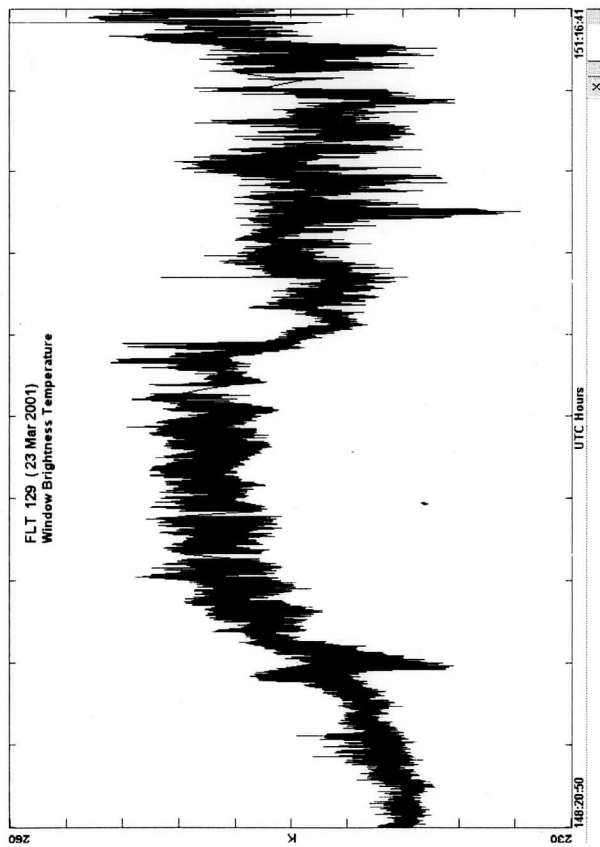






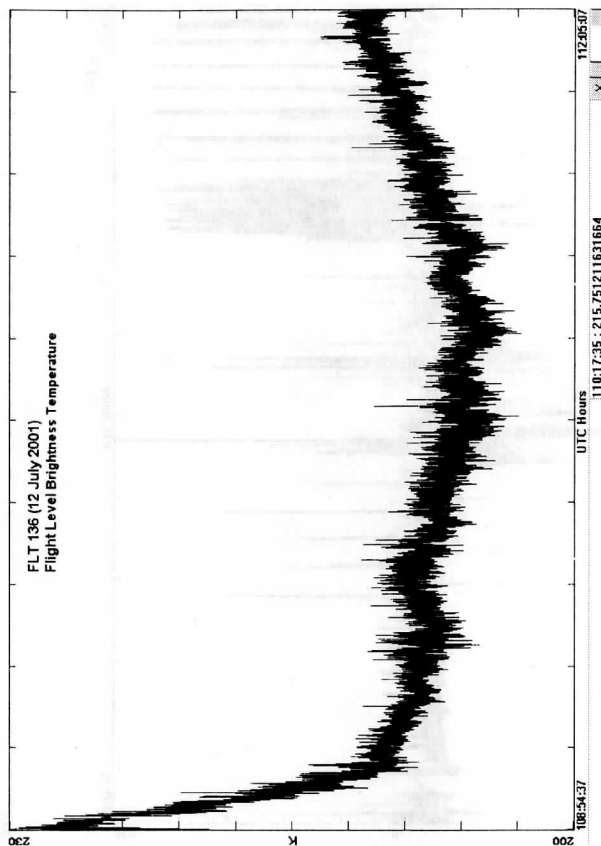
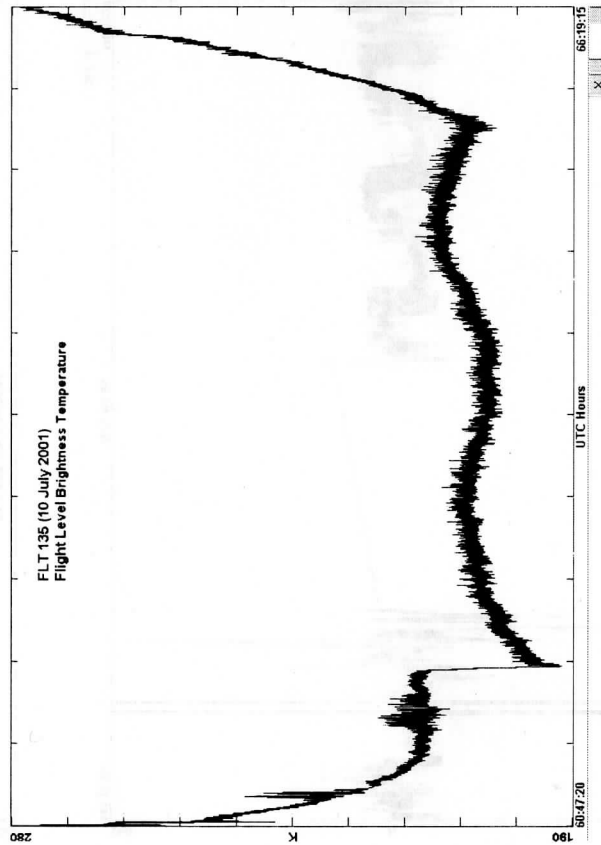
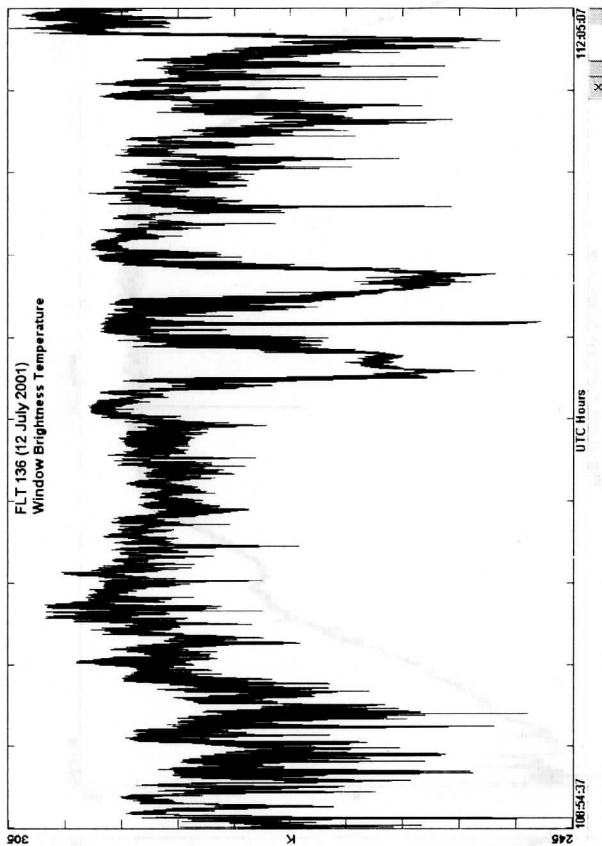
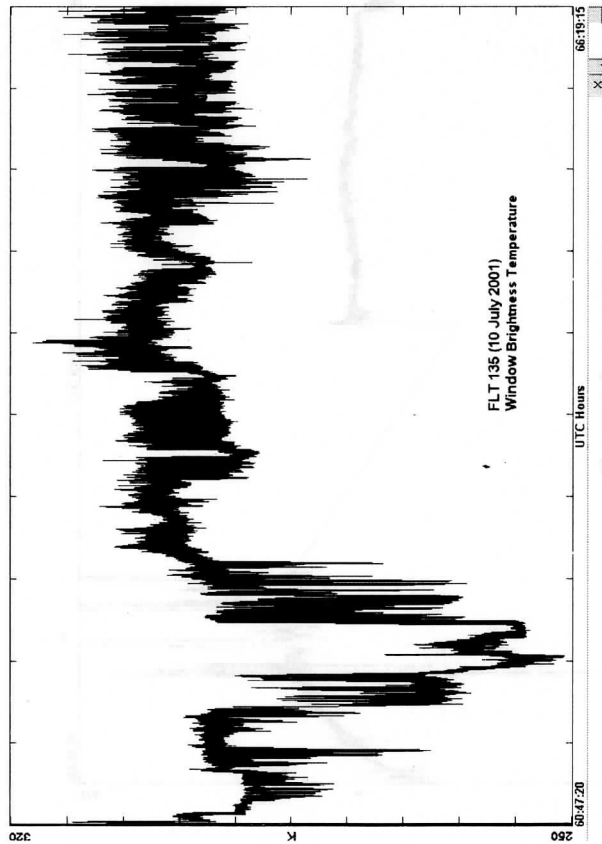


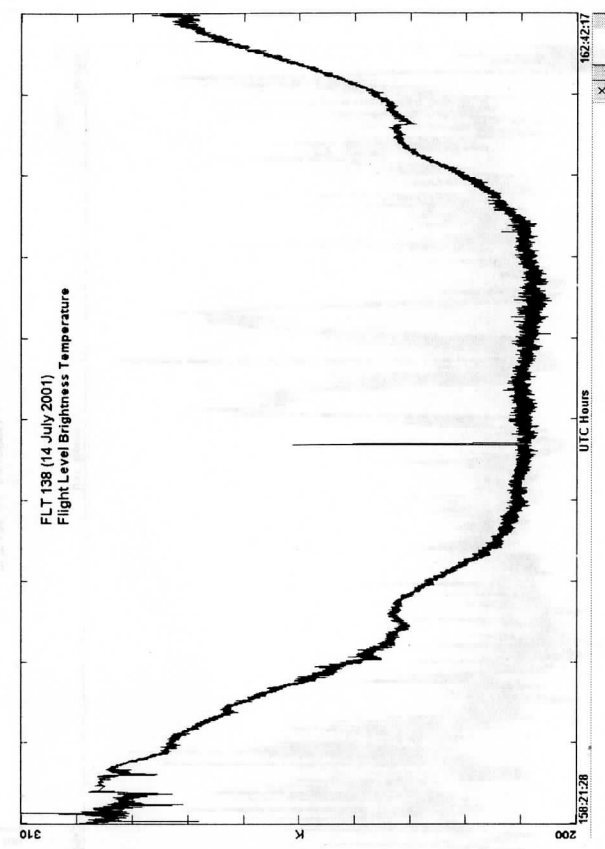
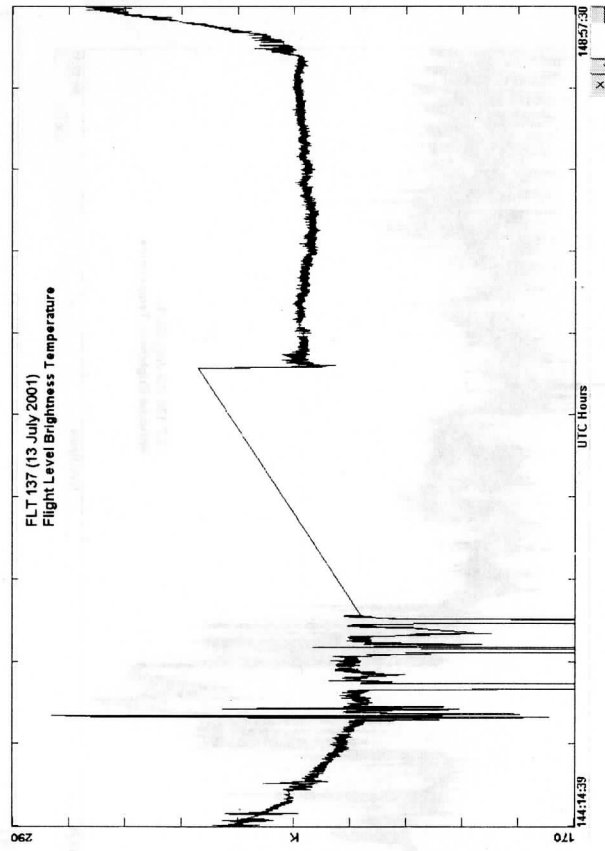
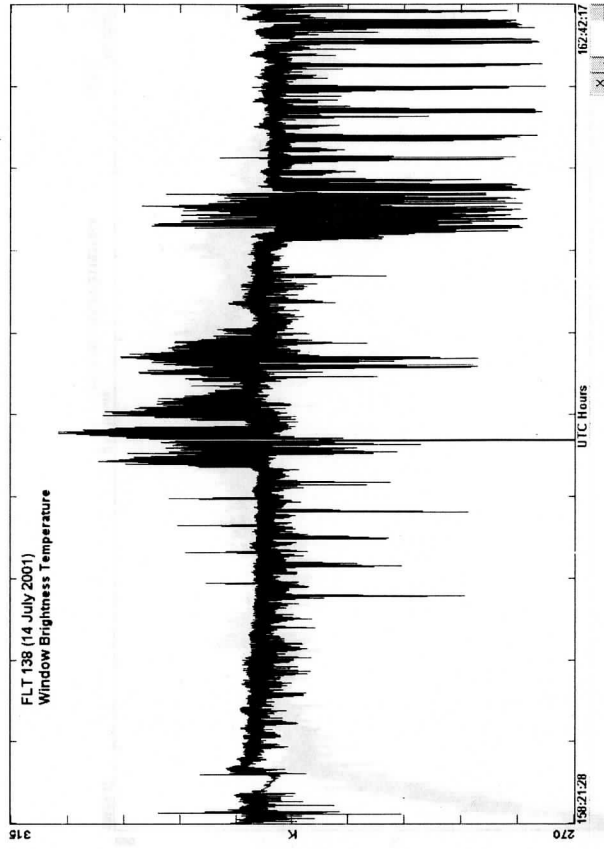
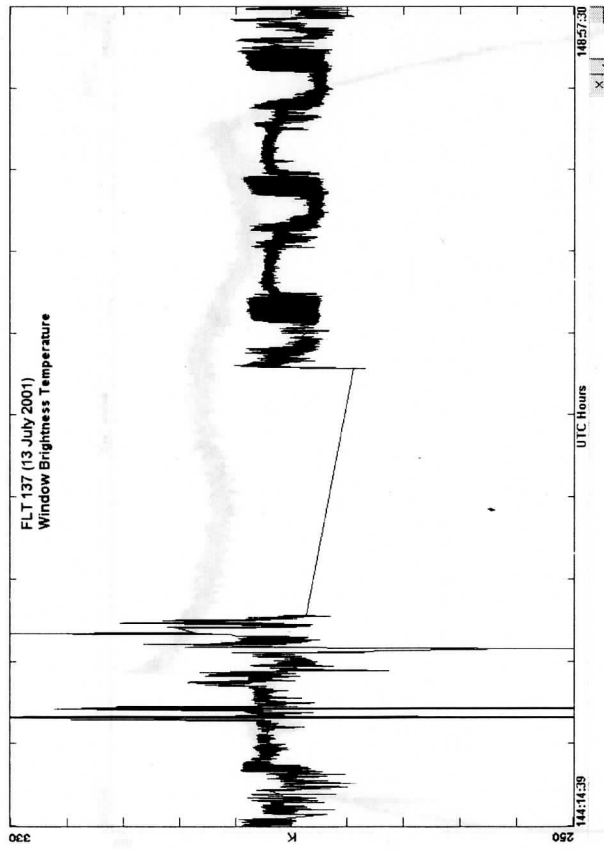


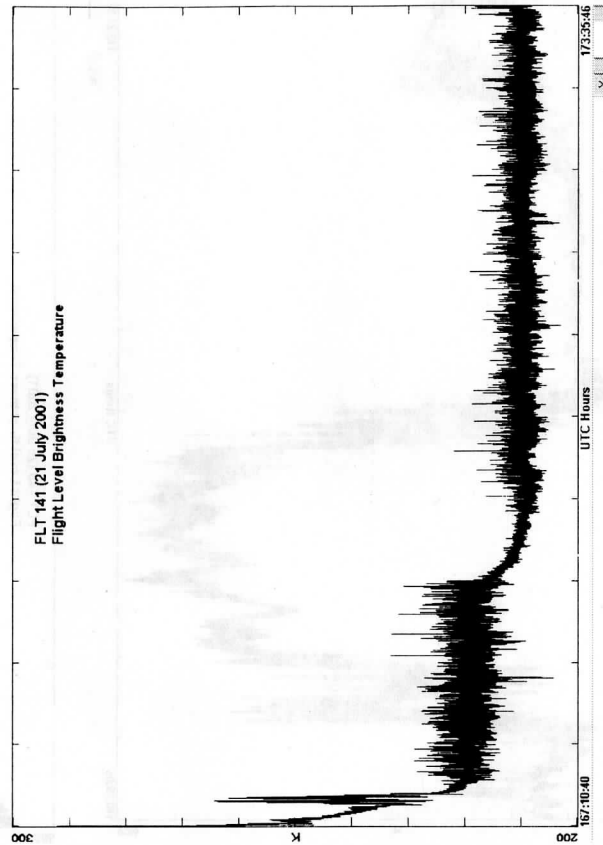
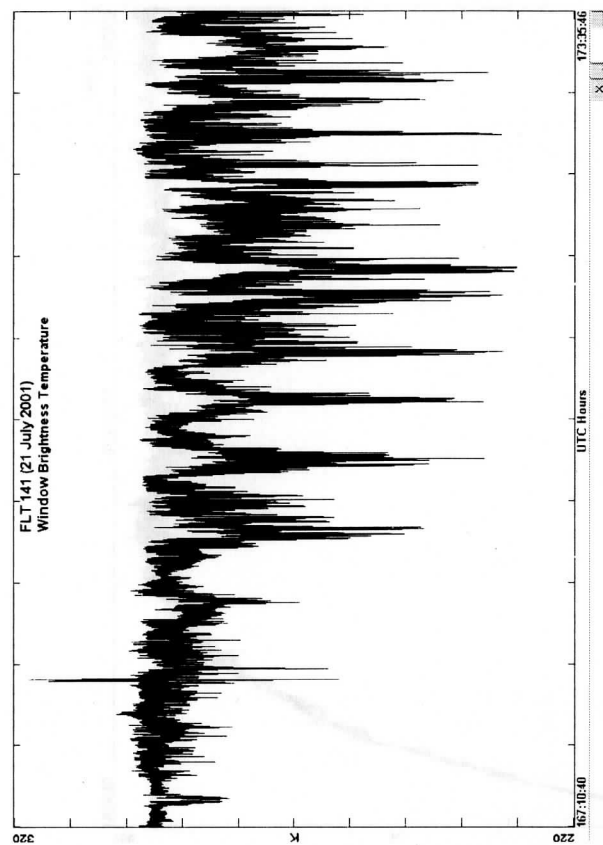
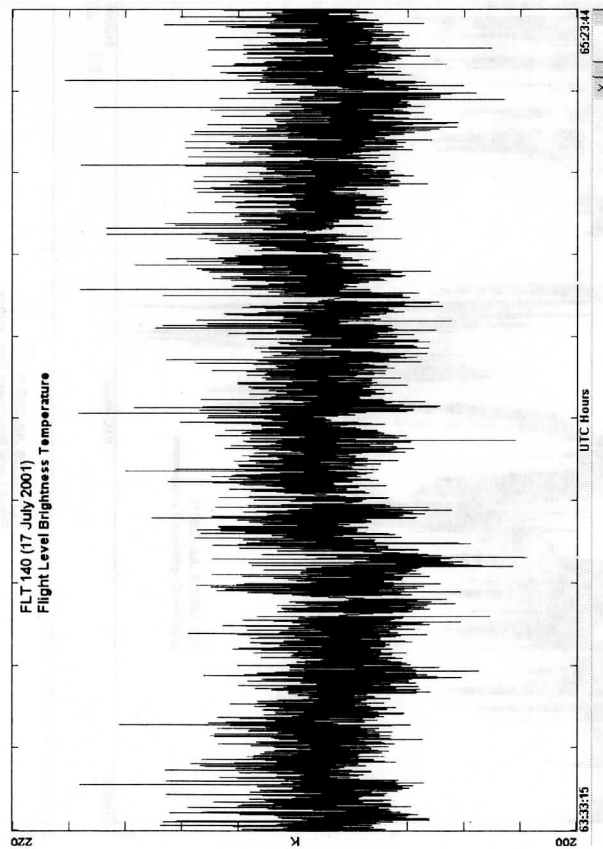
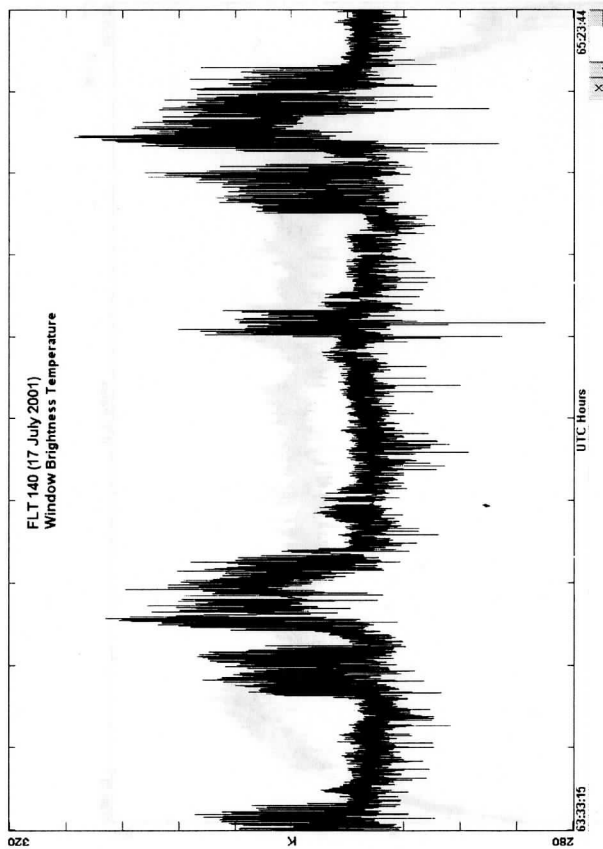


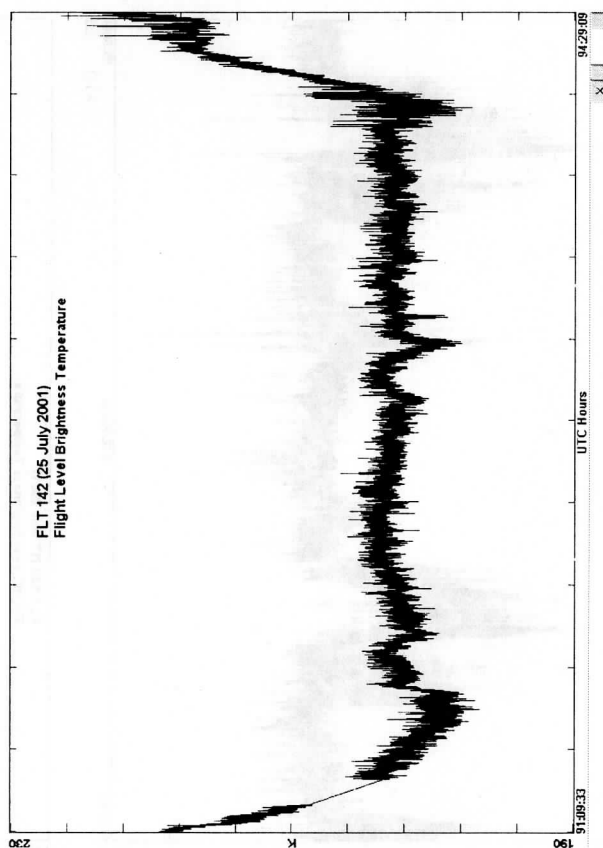
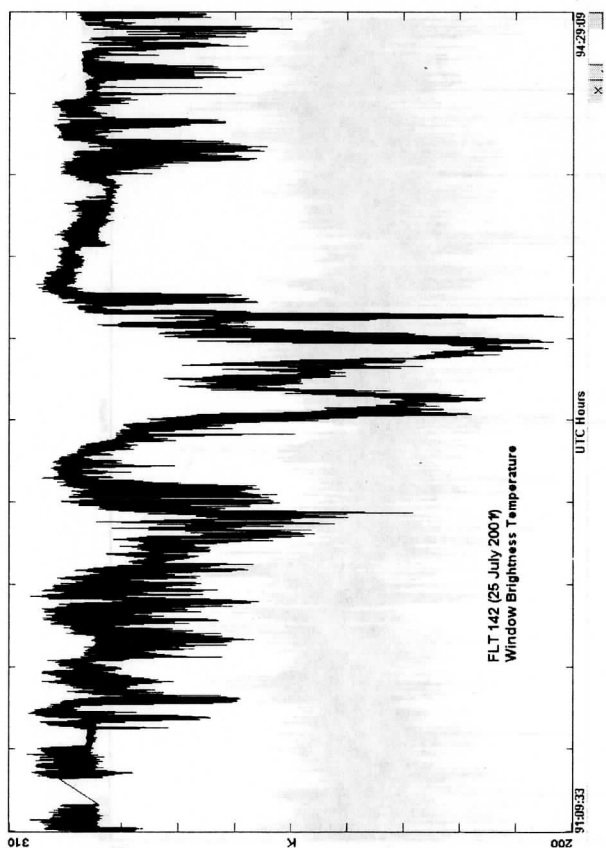
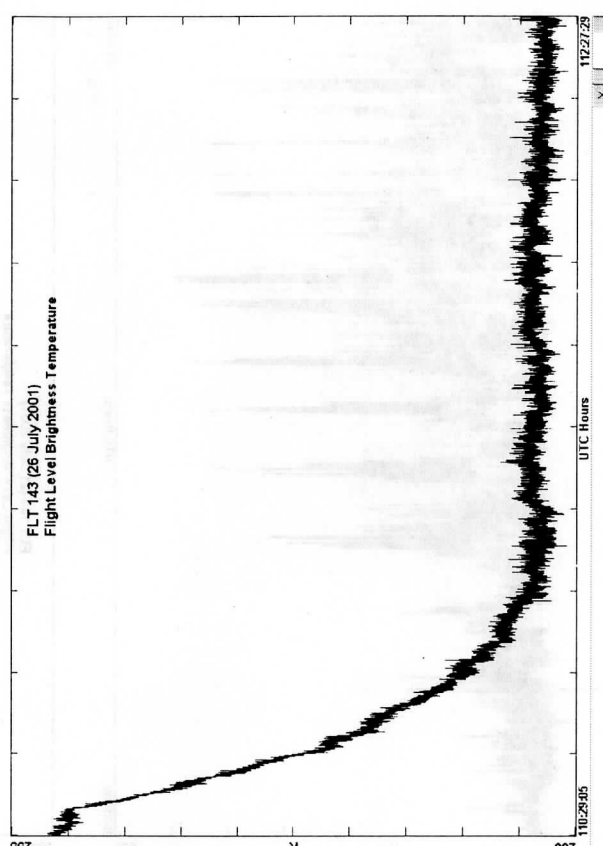
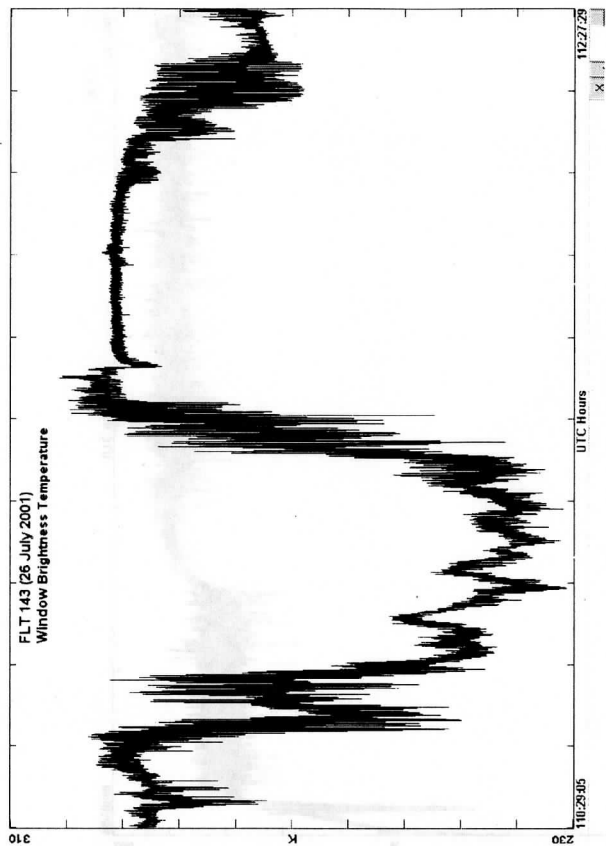
Appendix B: CLAMS Brightness Temperature Graphs

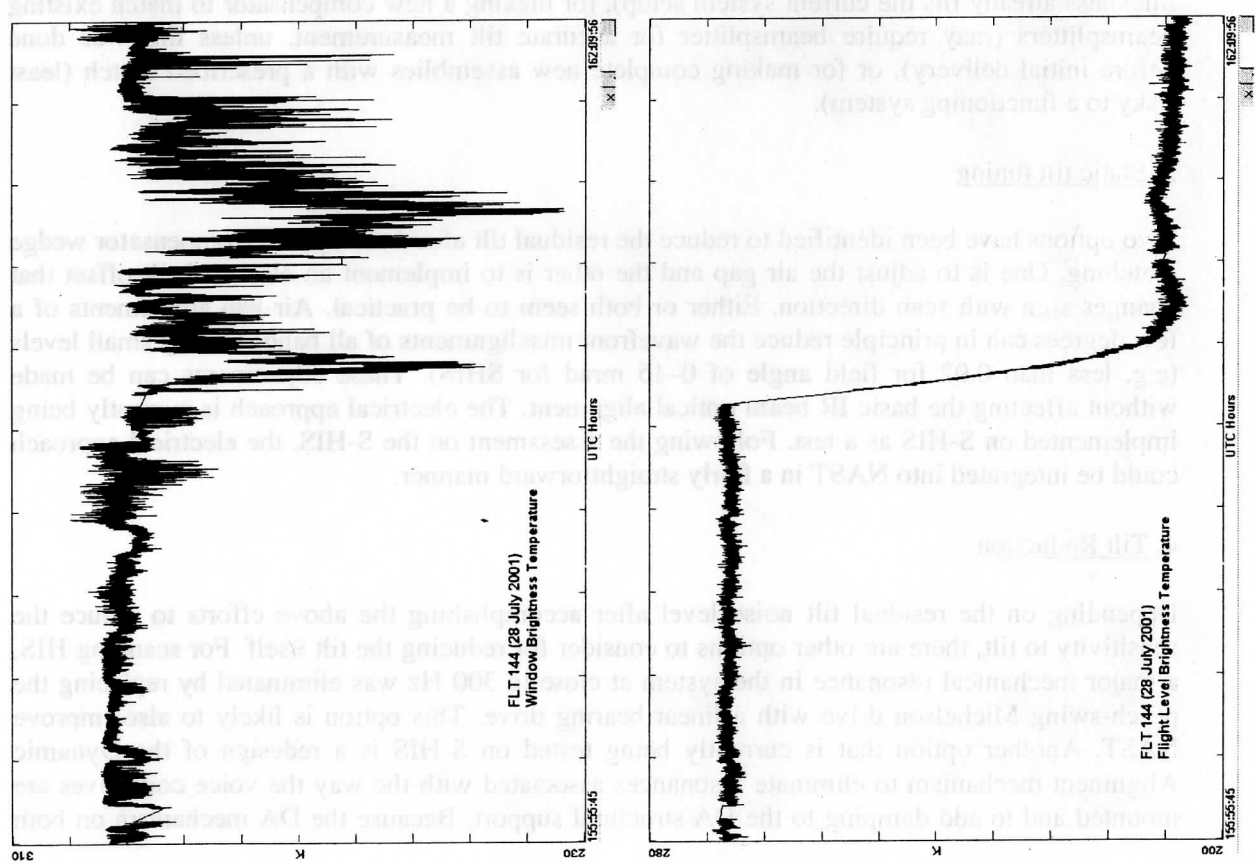
This appendix contains summary plots of the NAST-I data collected during the TRACE-P experiment. Plots are included of the longwave window channel equivalent brightness temperature ($10\text{ }\mu\text{m}$) and a flight level temperature ($15\text{ }\mu\text{m}$). The longwave infrared window channel shows the provides a coarse estimate of surface skin temperature (uncorrected for atmospheric effects) in clear skies or cloud top temperatures in the presence of clouds. The longwave infrared window channel plot is a useful "quicklook" to determine the regions of when clouds are present in the data. The flight level temperature clearly illustrates the data time periods when the aircraft is in ascent/descent or in level flight.. The flight level temperature is generally insensitive to the presence of clouds.











Appendix C: Suggested Modifications to NAST for Improving Performance and Reliability

(This material was generated 24 May 2001).

Improvements to Tilt Noise Performance

1. Air gap adjustment

Current UW calculations indicate that air gap adjustments cannot correct static tilt differences of the size currently existing in either instrument (this was pointed out to MIT/LL and they confirmed that (to their surprise) their model could not come up with a solution). These adjustments may be useful in tuning the final alignment, and a procedure must be developed to implement this capability.

2. Beamsplitter-Compensator wedge matching

According to Chuck Anderson of Spectral Systems, wedge matching to 4–5 arcsec or 20–25 microradians is reasonably easy (2 arcsec can be accomplished with extra care and 1 arcsec is possible). With 4 arcsec, SHIS (NAST) static wavefront tilt of 13–17 (7–10) microrad goes to <2 microrad, a huge improvement given that tilt errors vary like the square of the misalignment. Chuck also points out a 2nd order channeling effect that can occur with especially well-matched wedges. It is not clear why this should occur, but other causes of static tilt (wedge rotation and surface flatness) may not warrant trying for better than the easily achieved 4–5 arcsec. Options exist for polishing the existing compensators (no time required to get the materials and the thickness already fits the current system setup), for making a new compensator to match existing beamsplitters (may require beamsplitter for accurate tilt measurement, unless this was done before initial delivery), or for making complete new assemblies with a prescribed match (least risky to a functioning system).

3. Static tilt tuning

Two options have been identified to reduce the residual tilt after beamsplitter-compensator wedge matching. One is to adjust the air gap and the other is to implement an electrical tilt offset that changes sign with scan direction. Either or both seem to be practical. Air gap adjustments of a few degrees can in principle reduce the wavefront misalignments of all bands to very small levels (e.g. less than 0.02 for field angle of 0–15 mrad for SHIS). These adjustments can be made without affecting the basic IR beam optical alignment. The electrical approach is currently being implemented on S-HIS as a test. Following the assessment on the S-HIS, the electrical approach could be integrated into NAST in a fairly straightforward manner.

4. Tilt Reduction

Depending on the residual tilt noise level after accomplishing the above efforts to reduce the sensitivity to tilt, there are other options to consider for reducing the tilt itself. For scanning HIS, a major mechanical resonance in the system at close to 300 Hz was eliminated by replacing the porch-swing Michelson drive with a linear-bearing drive. This option is likely to also improve NAST. Another option that is currently being tested on S-HIS is a redesign of the Dynamic Alignment mechanism to eliminate resonances associated with the way the voice coil drives are mounted and to add damping to the DA structural support. Because the DA mechanism on both

instruments is essentially identical, it would be straightforward to implement this upgrade on the NAST. Finally, a third possibility is to modify the cooler mounts to reduce the cooler-induced vibration. Taken alone, this option may not be very effective since the aircraft induced tilts are apparently of a comparable size.

5. Tilt Measurement System

The S-HIS has a two axis stand-alone tilt monitoring system that provides the interferometer tilt angle error throughout an interferogram scan at the sampling rate of the interferometer. This tilt data may be used in the data processing to correct for the residual tilt error. It is believed that NAST now has one axis of tilt measurement, but it measures tilt at coarser resolution than would be required to make a proper correction. Both software and hardware implementations are involved with this task.

Hardware: The S-HIS tilt board would not itself need hardware modifications. Software modifications to its logic programming may be required in order to come up with an optimal interface to the NAST-I instrument controller PC. A significant hardware effort may be required in order to bridge the Tilt collector to the PC buses. Possible hardware interfacing avenues include bi-directional parallel port (EPP or ECP), direct PCI, or the inclusion of a TI C40 DSP board; more remote possibilities include SCSI, USB, or ethernet.

Software: Inserting code into the NAST-I control software in order to receive and store the tilt data may be a significant undertaking as well. Interfacing to the hardware can be major systems work (i.e. device driver authoring). In the case of S-HIS, a change of operating system was required on the data storage computer in order to handle the increased bandwidth requirements. Storing the tilt data is a similar quantity of data to a complex interferogram ($4096 \text{ values} \times 2 \text{ directions} \times 16 \text{ bits}$), which was a 50% increase in data volume on S-HIS. Of note, also, is that the PC component of S-HIS has no control functions: control in S-HIS is done entirely by realtime software on the TI C40 Controller DSP; the hardware linkage to the Tilt controller was built expressly to interface directly to the TI DSP.

Operational Enhancements

1. Housekeeping System:

In order to significantly enhance the housekeeping capabilities of the NAST instrument, a duplicate of the S-HIS housekeeping system could be built-up and integrated into the NAST. The S-HIS housekeeping system monitors 72 different channels, including temperatures, pressures, humidity, system voltages and currents, DA voltages and laser voltages. Both software and hardware implementations are involved with this task.

Hardware: The bandwidth requirements on the housekeeping are significantly lower than the tilt board, due to loosened requirements on both temporal resolution and low data volume (128 values/0.5 sec). The S-HIS housekeeping board was also built to interface directly to a FPLA on the TI C40 Controller DSP. Recreating this interface to a DSP board in the NAST-I computer, interfacing the board to bi-directional parallel port (EPP or ECP), or to a PC serial port are strong possibilities for hardware interfaces.

There are also a number of issues with inserting the actual measurement points into the existing NAST-I instrument hardware.

Software: The issues for the housekeeping system are similar to the tilt subsystem, but again, have lower overall timing and throughput requirements.

2. Data System:

Upgrades include provisions for integrating enhanced tilt and housekeeping systems and an upgrade of the storage computer.

Hardware integration of tilt and housekeeping: One slot each will be required in the NAST control computer backplane to accommodate the tilt and housekeeping upgrades. According to our knowledge, the controller computer is "feature-saturated" and cannot accept any more expansion. One possibility for extending the life of this system is to free up interrupts and I/O by replacing existing serial ports with a multi-port board (e.g. Control RocketPort). Further hardware would need to be added in order to transport data and commands to and from the housekeeping and tilt boards used by S-HIS.

Upgrade of storage/control computer: Building a new control/storage computer system from the ground up (similar to that used by the S-HIS), using the current implementation as a reference would provide the following:

- enhanced storage capacity
- network packetized transport of realtime data streams (i.e. permit realtime monitoring)
- rapid network download of data (eliminate removable disk)
- integrate tilt/housekeeping (by way of ancillary data DSP?)

In the case of a rebuild of the storage/control computer, the software system will need similar reassessment, operating system inclusive.

Appendix D: Cloud Properties Publication

Retrieval of Cloud Top Height, Effective Emissivity, and Particle Size, from Aircraft High Spectral Resolution Infrared Measurements

*Paolo Antonelli, *Steven A. Ackerman, *W. Paul Menzel,
*Allen Huang, +Bryan A. Baum, +William L. Smith

*Cooperative Institute for Meteorological Satellite Studies, University of Wisconsin-Madison,
1225 W. Dayton St., Madison, WI

+NASA Langley Research Center, Hampton, VA

Abstract

In this study we compare different approaches to retrieve Cloud Top Height (CTH), Cloud Effective Emissivity (CEE), and the Cloud Particle Size (CPS) from aircraft high-spectral resolution infrared measurements. Two independent methods are used to infer CTH. One approach is based on a high spectral resolution version of the *CO₂ Slicing* algorithm characterized by a statistically based selection of the optimal channel pairs. Another approach the Minimum Local Emissivity Variance algorithm (MLEV) takes advantage of high-resolution observations in the 8-12 micron region to simultaneously derive CTH and CEE. Once CTH has been retrieved a third method, based on the comparison between simulated and observed radiances, is used to infer CPS and CEE. Simulated radiances are computed for 18 microwindows between 8.5 and 12 microns. The cirrus scattering calculations are based on three-dimensional randomly oriented ice columns assuming six different particle size distributions. Multiple scattering calculations are performed for 26 different cloud optical thicknesses (COT) between 0 and 20. The simulated radiances are then compared to the observed radiances to infer COT and CPS for each spectral measurement. We applied these approaches to High-resolution Interferometer Sounder (HIS), National Polar-Orbiting Operational Environmental Satellite System Airborne Sounder Testbed-Interferometer (NAST-I) and Scanning-HIS (S-HIS) data. The preliminary results, consistent between the different algorithms, suggest that the high spectral resolution measurements improve the accuracy of the cloud property retrievals.

keywords: Hyperspectral infrared data, Cloud properties, *CO₂ Slicing*, *MLEV*, Particle Size retrieval

1 Introduction

In the next few years, new instruments will be launched to improve observations of atmospheric temperature, water vapor and winds. In the area of infrared remote sensing a key role is represented by the new generation of very high spectral resolution instruments (interferometers/spectrometers) like the Geostationary Imaging Fourier Transform Spectrometer (GIFTS), the Atmospheric Infrared Sounder (AIRS), the Cross-Track Infrared Sounder (CrIS) [6], and the Infrared Atmospheric Sounding Interferometer (IASI) [2]. In the last decade, prototypes of these instruments have been extensively tested on high altitude aircrafts, and have provided the scientific community with a wide variety of observations. In particular the High-resolution Interferometer Sounder (HIS) [12], the NPOESS Aircraft Sounder Testbed-Interferometer (NAST-I), the Scanning High-resolution Interferometer Sounder (S-HIS), have been employed in several missions in combination with other instruments like the Cloud Lidar System (CLS) and the Moderate-Resolution imaging spectroradiometer Airborn Simulator (MAS). Using observations obtained by the HIS instrument during the SUBsonic aircraft Contrail and Cloud Effects Special Study (SUCCESS) mission, this paper aims to prove that the high spectral resolution measurements will lead to an overall improvement of the cloud properties retrieval. The paper also introduces a new procedure that combines different approaches to simultaneously retrieve cloud top altitude, cloud effective spectral emissivity and cloud effective particle size. This procedure, that combines three different algorithms, represents the foundation of the future cloud detection operational scheme for GIFTS.

The first approach used to derive CTH and CEE is based on an extension of the broad band *CO₂ Slicing* [3] to the High-spectral resolution case (Hi-spectral resolution *CO₂ Slicing HiCO₂ Slicing*). The algorithm relies on the fact that using the broad *CO₂* absorption band at 15 μm , clouds at various levels of the atmosphere can be detected. In fact the radiances from strong absorption bands are sensitive to only upper levels while the radiances from the wings see successively lower levels of the atmosphere. The *HiCO₂ Slicing* slicing algorithm determines both cloud level and cloud effective emissivity from radiative transfer principles. It differs from the broad band version mainly

for the number of channels available to the algorithm for the retrieval¹ and for the higher spectral resolution of the measurements. The results obtained with *HiCO₂ Slicing* have been validated by collocated CLS observations.

The second approach is represented by the Minimum Local Emissivity Variance (*MLEV*) algorithm. This algorithm retrieves cloud spectral effective emissivity, for single layer cloud only, as a function of cloud top height. It is based on the concept that the best estimate of the cloud top pressure is the one that minimizes the variance of the retrieved spectral emissivity², i.e. the one that guarantees the smoothest spectral emissivity in the region between $11.7 < \lambda < 13.3 \mu m$ ($750 < \nu < 850 cm^{-1}$).

The idea of using those two independent approaches to retrieve CTH and to identify clear-sky Field of View (FOV)³, is motivated by the importance of assigning a confidence level to the retrieved values, the level of confidence being proportional to the degree of agreement between the results obtained by the different algorithms. The algorithm that synthesizes the different results and assigns a confidence level is still under development and the presentation of its implementation is beyond the scope of this paper.

The third approach represents the last step of the future operational scheme for cloud properties retrieval. It uses as input the CTH obtained from the *HiCO₂ Slicing* and *MLEV* algorithms along with the temperature and water vapor profiles retrieved in a nearby clear-sky FOV, and outputs CPS and COT. The algorithm is based on the comparison between simulated and observed radiances and requires the knowledge of the CTH. Simulated radiances are computed for 18 microwindows between 8.5 and 12 microns [1]. The cirrus scattering calculations are based on three-dimensional randomly oriented ice columns assuming six different particle size distributions. Multiple scattering calculations are performed for 26 different cloud optical thicknesses (COT) between 0 and 20. The simulated radiances are then compared to the observed radiances to infer COT and CPS for each spectral measurement. The retrieved COT values are finally used for a consistency check: COT values are converted into CEE values and are compared to the CEE results obtained by the first two approaches.

Section 2 gives a brief description of the HIS instrument and of the data set used to test the algorithms. Section 3 describes the theoretical basis for the different algorithms. Section 4 is dedicated to the presentation of the results and to the discussion of the criteria used for validation. Section 5 contains the conclusion and presents the guidelines for the future work.

2 Instrument and Data Set

2.1 HIS

HIS is a Michelson Interferometer that generates double-sided interferograms produced by displacing a mirror a set distance called an Optical Path Delay, OPD for short, [11], [12], [4]. Interferograms are produced at the rate of one every six seconds, with twelve interferograms produced before on-board calibration is performed. One interferogram consists of the forward or backward transverse of the Michelson moving mirror across the full optical path length, with separate detectors for each spectral band of incoming radiation. Calibration is performed by rotating a 45° scan mirror from nadir, twice sampling two high emissivity blackbodies, servo controlled to 300K and 240K. The three spectral bands, covering most of the region from 3.8 to 16 μm , are split inside a single liquid helium dewar, which contains three sets of bandpass cold filters, focusing optics, and arsenic-doped silicon detectors. On-board numerical filtering is used to reduce the sample rate from the HeNe laser rate by factors of 14, 8, and 8 in Bands I, II, and III, respectively. The HIS instrument has been flown aboard NASA ER2 aircraft at approximately 20 km or 50 hPa. The instrument is shock mounted to dampen high-frequency vibrations from the aircraft.

2.2 Cloud Lidar System

The Cloud Lidar System (CLS) [8, 9], which is operated from the left ER-2 superpod, measures the backscatter cross-sections of cloud and aerosol particles at 1.064 and 0.532 microns. It is used primarily to profile clouds below the flight level of the aircraft that is typically 18.0-20.5 km. In cases where the cloud optical thicknesses are small, boundary layer aerosol backscatter signals are detectable. The 0.532 micron lidar return is split into signals that are

¹Theoretically the *HiCO₂ Slicing* can count on a number of channels up to 3 orders of magnitude larger than the number of channels currently available for the broad band *CO₂ Slicing*.

²In presence of small ice particle the spectral emissivity dependency from the channels frequency can be very strong and the *MLEV* approach might not be optimal.

³A clear-sky FOV can be identified by low (< 0.1) values of the effective emissivity.

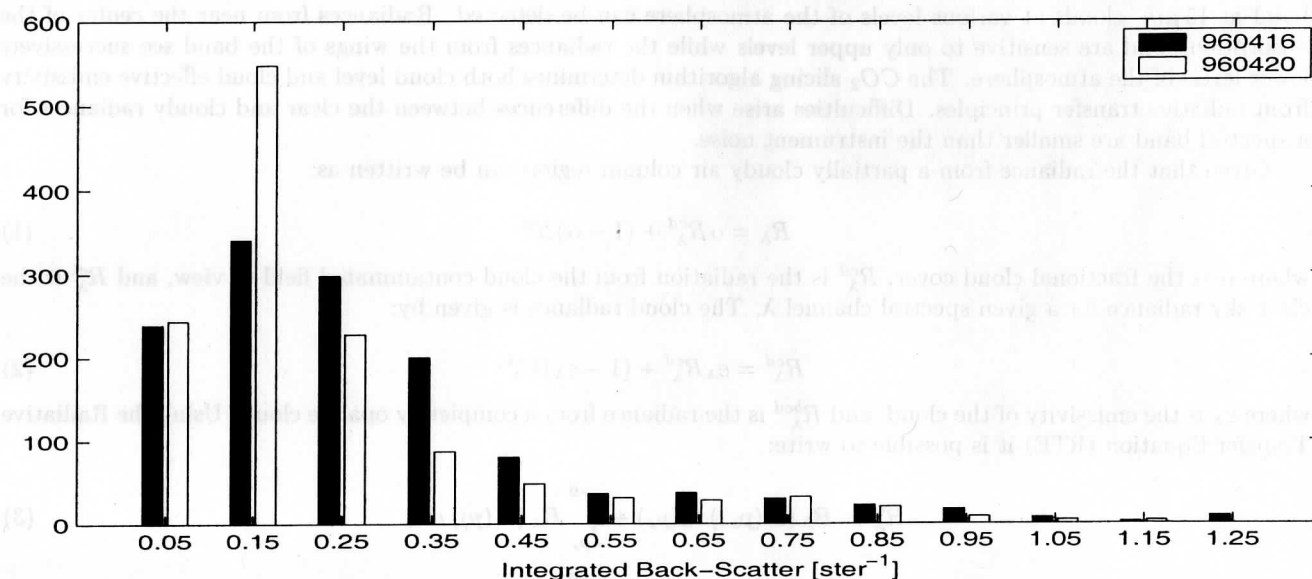


Figure 1: Histogram of the lidar integrated back-scatter signal for the 960416 and 960420 flights.

parallel and perpendicular to the outgoing laser radiation, thereby providing polarization sensitive data principally for cloud particle phase state detection. The cloud lidar provides information on the internal vertical structure of optically thin clouds which aids in the determination of the overall influence of such clouds on the radiative balance in both the shortwave and longwave portions of the spectrum. The CLS can provide information on cloud particle characteristics. Figure 1 shows the histograms of the lidar integrated back-scatter signal for both the 960416 and 960420 flights.

2.3 Data Set

The data sets used to test the different retrieval algorithms were obtained from the SUCCESS mission (8 April - 10 May 1996). SUCCESS was a NASA field program using scientifically instrumented aircraft and ground based measurements to investigate the effects of subsonic aircraft on contrails, cirrus clouds and atmospheric chemistry. SUCCESS was coordinating with the Department of Energy's Atmospheric Radiation Measurements Program (ARM) which operates the Clouds and Radiation Testbed (CART) site located in Northern Oklahoma, and Southern Kansas. An objective of SUCCESS was to better determine the radiative properties of cirrus clouds and of contrails so that satellite observations could better determine their impact on Earth's radiation budget. The determination of how cirrus clouds form; whether the exhaust from subsonic aircraft presently affects the formation of cirrus clouds, and if so whether the changes induced are of climatological significance, were all research areas addressed by SUCCESS. During the SUCCESS, all three NASA aircraft were based in Salina, Kansas on the Salina campus of Kansas State University. A series of flights, averaging one every other day during this period, were made mainly near the DOE CART site. Additional flights were made over the Rocky Mountains, to investigate wave clouds. Flights were also made over the Gulf of Mexico to utilize an oceanic background for remote sensing measurements.

Data acquired during 16 and 20 April, 1996 are selected for the demonstration of cloud property retrievals.

3 Algorithms

3.1 CO₂ Slicing

3.1.1 Theory

CO₂ slicing [3] has been extensively used to retrieve cloud top pressure and cloud effective emissivity using High resolution Infrared Radiation Sounder (HIRS) and MODIS data. With radiances around the broad CO₂ absorption

band at $15\mu m$, clouds at various levels of the atmosphere can be detected. Radiances from near the center of the absorption band are sensitive to only upper levels while the radiances from the wings of the band see successively lower levels of the atmosphere. The CO_2 slicing algorithm determines both cloud level and cloud effective emissivity from radiative transfer principles. Difficulties arise when the differences between the clear and cloudy radiances for a spectral band are smaller than the instrument noise.

Given that the radiance from a partially cloudy air column region can be written as:

$$R_\lambda = \alpha R_\lambda^{cd} + (1 - \alpha) R_\lambda^{cl} \quad (1)$$

where α is the fractional cloud cover, R_λ^{cd} is the radiation from the cloud contaminated field of view, and R_λ^{cl} is the clear sky radiance for a given spectral channel λ . The cloud radiance is given by:

$$R_\lambda^{cd} = \varepsilon_\lambda R_\lambda^{cd} + (1 - \varepsilon_\lambda) R_\lambda^{cl} \quad (2)$$

where ε_λ is the emissivity of the cloud, and R_λ^{bcd} is the radiance from a completely opaque cloud. Using the Radiative Transfer Equation (RTE) it is possible to write:

$$R_\lambda^{cl} = B_\lambda(T(p_s)) \tau_\lambda(p_s) + \int_{p_s}^0 B_\lambda(T(p)) d\tau_\lambda \quad (3)$$

$$R_\lambda^{cd} = B_\lambda(T(p_c)) \tau_\lambda(p_c) + \int_{p_c}^0 B_\lambda(T(p)) d\tau_\lambda \quad (4)$$

where p_c is the cloud top pressure. Integrating by parts and subtracting the two terms it is possible to write:

$$R_\lambda^{cl} - R_\lambda^{bcd} = \int_{p_c}^{p_s} \tau_\lambda(p) dB_\lambda \quad (5)$$

therefore

$$R_\lambda - R_\lambda^{cl} = \alpha \varepsilon_\lambda \int_{p_s}^{p_c} \tau_\lambda(p) dB_\lambda \quad (6)$$

where $\eta_\lambda = \alpha \varepsilon_\lambda$ is often called the cloud effective emissivity or the effective cloud amount. The ratio of the deviations in cloud produced radiances and corresponding clear air radiances for two spectral channels (pair), λ_1 and λ_2 , viewing the same field of view can thus be written:

$$\frac{R_{\lambda_1} - R_{\lambda_1}^{cl}}{R_{\lambda_2} - R_{\lambda_2}^{cl}} = \frac{\eta_{\lambda_1} \int_{p_s}^{p_c} \tau_{\lambda_1}(p) dB_{\lambda_1}}{\eta_{\lambda_2} \int_{p_s}^{p_c} \tau_{\lambda_2}(p) dB_{\lambda_2}} \quad (7)$$

If the wavelengths are chosen close enough together, then $\varepsilon_{\lambda_1} \simeq \varepsilon_{\lambda_2}$ and the cloud top pressure within the FOV can be determined minimizing the difference between the left and the right side of eq. 7. The left side is generally calculated using the real observations for R_λ while for R_λ^{cl} it is possible to use either a nearby clear pixel radiance or a value simulated from known temperature and water vapor profiles. The right side is calculated from the known temperature and water vapor profiles as a function of p_c , the cloud top pressure.

3.1.2 Implementation

Given the limited number of channels of the spectroradiometers, the operational versions of CO_2 slicing generally use only a few channel pairs to determine the cloud top height [3], [7]. On the contrary given the high spectral resolution of the interferometric data, the Hyperspectral version of CO_2 Slicing (*HiCO₂ Slicing*) takes advantage of numerous pairs; selecting the best pairs to be used in the retrieval however, requires a well defined strategy. Smith and Frey [13] suggested using only those pairs which are the most sensitive to variations of the cloud top height. This paper describes a different criterion for the pair selection. The pair selection is performed maximizing the accuracy of the retrieved cloud top height values on a *dependent* data set. The selected pairs are then used to retrieve CTH for different, independent, data sets.

The algorithm used to select the channel pairs, or *pair selection* algorithm, can be summarized in the following way:

- select a single flight from the SUCCESS mission
- simulate the clear sky radiances and the transmittance profiles applying the fast forward model to the closest⁴ rawinsonde profiles
- select all the channels in the $14\mu m$ absorption band whose weighting functions peak between $200mb$ and $900hPa$
- define the CO_2 pairs taking all the possible combinations of those channels, with the first channel in the pair always associated with the lower wavenumber
- using all the selected pairs, apply the CO_2 slicing technique to retrieve the cloud top heights
- compare, for each pair, the retrieved cloud top to the lidar data and count for how many FOVs a given pair has provided results in agreement⁵ with the lidar data
- select the pairs that have given results in agreement with the lidar measurements for at least 30 % of the flight FOVs

The $14\mu m$ band⁶ is selected because the channels in this band see the troposphere and it is the only band selected because the CO_2 slicing technique is applicable only if the channels in every pair are spectrally close. The use of window channels along with the lack of knowledge of the cloud phase would imply $\varepsilon_{\lambda_1} \neq \varepsilon_{\lambda_2}$ and equation 7 would not be applicable. Finally to limit the number of selected pairs, in the last step of the algorithm the threshold value for accepting or rejecting a pair is set equal to 30 %. That is, a pair is selected only if it gives results in agreement with the lidar measurement for at least 30 % of the flight FOVs, and the pairs containing channels more than $10cm^{-1}$ apart or channels located on water vapor lines are rejected. A better criterion, that will be investigated in the future, would be to set the threshold value according the distribution of the cloud heights in the training data-set. For example if only 10 % of the clouds are below $4000m$, the pairs that successfully retrieve the cloud height for those clouds should be selected even if they provide good results in only 10 % of the total cases.

Once the pairs are selected the *HiCO₂ Slicing* algorithm can be applied to retrieve the cloud top pressure and the effective emissivity. For each FOV only the N_{pairs} different solutions for which

$$\frac{\int_{p_s}^{min(p_c)} \tau_{\lambda_1}(p) dB_{\lambda_1}}{\int_{p_s}^{min(p_c)} \tau_{\lambda_2}(p) dB_{\lambda_2}} \leq \frac{R_{\lambda_1} - R_{\lambda_1}^{cl}}{R_{\lambda_2} - R_{\lambda_2}^{cl}} \leq \frac{\int_{p_s}^{max(p_c)} \tau_{\lambda_1}(p) dB_{\lambda_1}}{\int_{p_s}^{max(p_c)} \tau_{\lambda_2}(p) dB_{\lambda_2}} \quad (8)$$

are then averaged to determine the CO_2 slicing solutions for the cloud top height and effective emissivity.

3.2 MLEV

3.2.1 Theory

Neglecting scattering processes, the infrared clear sky radiance measured by high spectral resolution instrument is given by 3. For complete cloud covered IFOV with opaque cloud the infrared cloudy sky radiance is given by eq. 4 while the upwelling radiance for a partially cloud-covered FOV is given by eq. 1. Combining these equations, the effective cloud emissivity spectrum η_λ can be calculated as:

$$\eta_\lambda = \frac{R_\lambda - R_\lambda^{cl}}{R_\lambda^{cd}(p_c) - R_\lambda^{cl}} \quad (9)$$

The fundamental principal of MLEV [5] is to seek the optimal solution of η_λ which is characterized by the smallest local variation. The algorithm also allows for the retrieval of CTH h_c , obtained as the optimal altitude solution which guarantees the smallest local variation of η_λ .

⁴Closest in time and space.

⁵For any given a FOV, there is agreement when the retrieved cloud top heights are within the boundaries of at least one of the cloud layers detected by the lidar for that specific FOV.

⁶The actual spectral band chosen is in the range $720 - 760cm^{-1}$.

3.2.2 Implementation

MLEV has been tested on the same data sets used to train and test the High Spectral Resolution version of *CO₂ Slicing*. The optimal *CTH* and the corresponding effective emissivity spectrum η_λ have been obtained using the following algorithm:

- identify the clear sky pixels using the available lidar data
- generate simulated clear sky radiances for the closest⁷ radiosonde observations available
- generate simulated cloudy radiances, using the closest radiosonde observations and introducing, at 31 different pressures between 850 *hPa* and 200 *hPa*, an infinitesimal thin, optically thick, cloud
- for each FOV
 - for each *CTH*
 - * generate $\eta_\lambda(h_c)$ using 9
 - * determine the local variance at each wavelength between $\sigma_{\lambda_k}(h_c) = \frac{\sum_{i=k-12}^{i=k+12} (\eta_{\lambda_i}(h_c) - \eta_{\lambda_k}^*(h_c))^2}{25}$ where $\eta_{\lambda_k}^*(h_c) = \frac{\sum_{j=k-12}^{j=k+12} \eta_{\lambda_j}(h_c)}{25}$ and $11.7 < \lambda_k < 13.3 \mu m$ ($750 < \nu_k < 850 cm^{-1}$).
 - find the *CTH* (h_c^*) that minimizes $\sum_{\lambda_k=11.7}^{\lambda_k=13.3} \sigma_{\lambda_k}(h_c)$
 - evaluate the spectral emissivity $\eta_\lambda(h_c^*)$ using 9

3.3 Particle Size and Optical Thickness Retrieval

3.3.1 Theory

The cloud optical depth and particle size are retrieved from HIS data using an approach that utilizes a radiative transfer model based on the discrete ordinates method (DISORT model). The DISORT model is set up to handle a number of discrete layers in the atmosphere. The clear-sky absorption properties are prescribed through the use of a set of correlated-k routines, and account for such absorbers as water vapor, carbon dioxide, ozone, chlorofluorocarbons, etc. For a given temperature and humidity profile, a set of correlated-k based optical thicknesses are calculated off-line for use in the DISORT calculations. The cirrus properties are based on single scattering calculations for randomly oriented hexagonal columns. Yang [14] describes how single scattering properties can be derived for ice particles that have strong absorption; this treatment is necessary for developing cirrus scattering properties in the interferometer microwindows. However, this treatment describes the calculation of scattering properties for a single crystal size. To approximate cirrus clouds, we further integrate the single scattering properties over a particle size distribution. To retrieve particle size and optical thickness from HIS data, a set of more than 30 size distributions, based on real measurements, is used. Essentially, the size distributions are chosen so that a range of effective radii can be adopted. For the calculations a subset of size distributions such that the effective radius ranged from 10 to 60 μm , is selected. Given the set of clear-sky absorption optical thicknesses for each layer and a set of cirrus scattering properties, we set up a series of DISORT calculations to perform forward calculations for a set of 6 different cirrus models (based on the varying size distributions). For each model, a set of 26 optical thicknesses were used ranging from extremely low values to a maximum value of 20. To summarize, look-up tables involving:

- 6 particle radii ranging from 10 to 60 μm
- 26 cirrus optical thicknesses
- 18 microwindows

enable the estimation of particle size and optical depth for a range of viewing angle and relative azimuth angles from the measured radiance spectrum and the associated temperature and water vapor profile conditions. In the examples provided here, the closest clear sky temperature and moisture profile retrievals are used for the calculation.

⁷Closest in time and space.

3.3.2 Implementation

The Particle Size Retrieval can be summarized as follows:

- inputs the observed spectrum for any given FOV along with the 18 simulated microwindows (for HIS the first 14 microwindows are in band 1 and the last 4 microwindows are in band 2)
- evaluate the real microwindows corresponding to the simulated radiances by integrating the real spectrum over the same spectral ranges covered by the simulated microwindows.
- retrieve Optical Path using only the last 4 microwindows (Radiance Matching), that is find the value of optical thickness that gives the smallest differences between simulated and real microwindows (band 2 only). NOTE the selected value of the Optical Thickness represents simply a first guess.
- retrieve Particle Size using only the first 11 microwindows (Slope Matching), that is find the value of particle size that gives the smallest differences between the slope of the simulated microwindows and the slope of the real microwindows (band 1 only).
- retrieve Optical Path using only band 1 (Radiance Matching). Once the particle size (slope) has been selected, the first 11 microwindows (band 1 only) are used to refine the retrieved value of COT, simply by matching the simulated radiances to the real radiances for those microwindows.

4 Results

4.1 *HiCO₂ Slicing*

For this experiment the radiances obtained in two different flights are divided into two different data-sets: the training data set (960416) and the testing data set (960420). The *pair selection* algorithm is applied to the radiances contained in the training data set. Out of 1287 possible pairs only 41 pairs satisfy all the *pair selection algorithm* requirements and, therefore, are selected for the *HiCO₂ Slicing* algorithm. Once the pairs are selected the *HiCO₂ Slicing* algorithm was applied to the flights.

Figure 2 a) shows the results obtained applying the *HiCO₂ Slicing* to the 960416 flight. The histogram shows the differences between the peak of the back-scattered lidar signal and the retrieved cloud top height. The statistics are derived for FOVs in which the integrated back-scattered signal is greater than 0.1 ster^{-1} with no distinction for single or multi layer clouds. The 0 bin represents CTH retrieved in $\pm 500 \text{ m}$ from the peak of the back-scattered lidar signal. The distribution is skewed toward positive values indicating that the Radiative Cloud Top Height is lower than the peak height for the back-scattered lidar signal. Figure 5, like figure 2 shows the differences between the peak of the back-scattered lidar signal and the retrieved cloud top height but in this case the statistics are derived for FOVs in which the integrated back-scattered signal is greater than 0.2 ster^{-1} and for single layer clouds only. The distribution is always skewed toward positive values indicating that the Radiative Cloud Top Height is lower than the peak height for the back-scattered lidar signal, but the results are more accurate. The percentage of CTH values retrieved within 500 m from the lidar back-scatter peak is increased by about 5%.

Figures 4 a) and 5 a) show that the results for the 960420 flight are more accurate than the 960416 results. The main difference is that for this flight the distributions are skewed towards negative values, indicating that the radiative CTH is above the lidar back-scatter peak. It is worth emphasizing that good results are obtained for the 960420 flight, the independent flight that is it is not used to derive the optimal pairs used by the *HiCO₂ Slicing* algorithm. More tests are required before drawing conclusions on the generalization skills of the algorithm, but the early results are encouraging. Table 1 shows a summary of the *HiCO₂ Slicing* and *MLEV* results.

4.2 *MLEV*

The results obtained by using the *MLEV* algorithm, figures 2, 3, 4, 5, seem to be, overall, less accurate than those obtained by the *HiCO₂ Slicing* algorithm. The main reason for the differences in the results might be found in the fact that, because of the radiative forward model currently used [10], *MLEV* can only retrieve the CTH on a set of 21 altitude levels, while *HiCO₂ Slicing* can average between those levels. To verify this hypothesis a new HIS

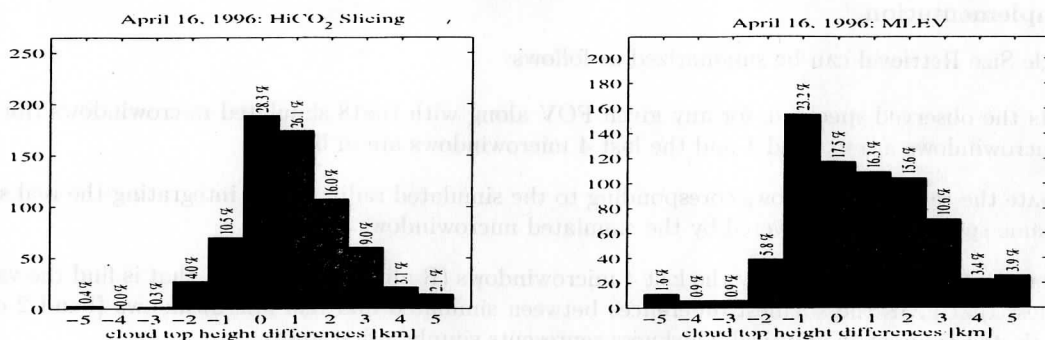


Figure 2: 960416: Cloud top height retrievals. The histograms show the differences between the retrieved cloud top height (*HiCO₂ Slicing* on the left and *MLEV* on the right) and the peak of the back-scattered lidar signal. The statistics are derived for FOVs in which the integrated back-scattered signal was greater than 0.1 ster^{-1} with no distinction for single or multi layer clouds. The 0 bin represents CTH retrieved in $\pm 500 \text{ m}$ from the peak of the back-scattered lidar signal.

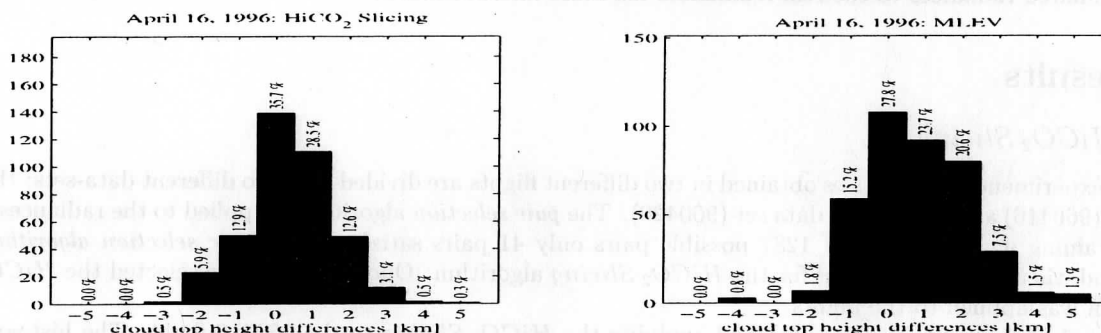


Figure 3: 960416: Cloud top height retrievals. The histograms show the differences between the retrieved cloud top height (*HiCO₂ Slicing* on the left and *MLEV* on the right) and the peak of the back-scattered lidar signal. The statistics are derived for FOVs in which the integrated back-scattered signal was greater than 0.2 ster^{-1} for single layer clouds only. The 0 bin represents CTH retrieved in $\pm 500 \text{ m}$ from the peak of the back-scattered lidar signal.

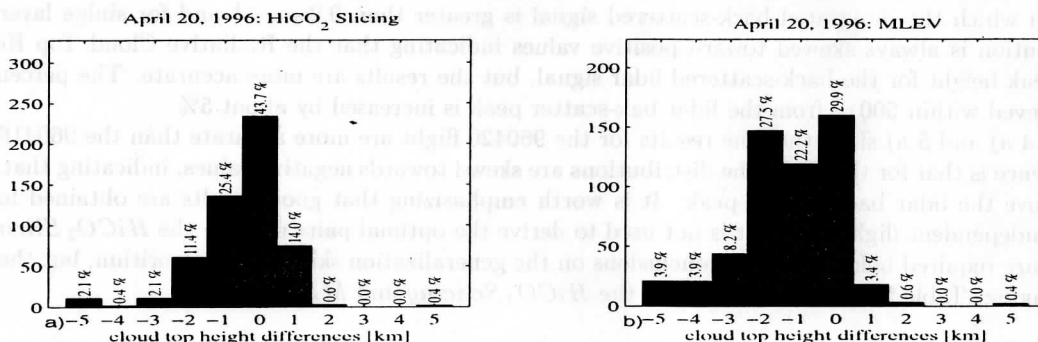


Figure 4: 960420: Cloud top height retrievals. The histograms show the differences between the retrieved cloud top height (*HiCO₂ Slicing* on the left and *MLEV* on the right) and the peak of the back-scattered lidar signal. The statistics are derived for FOVs in which the integrated back-scattered signal was greater than 0.1 ster^{-1} with no distinction for single or multi layer clouds. The 0 bin represents CTH retrieved in $\pm 500 \text{ m}$ from the peak of the back-scattered lidar signal.

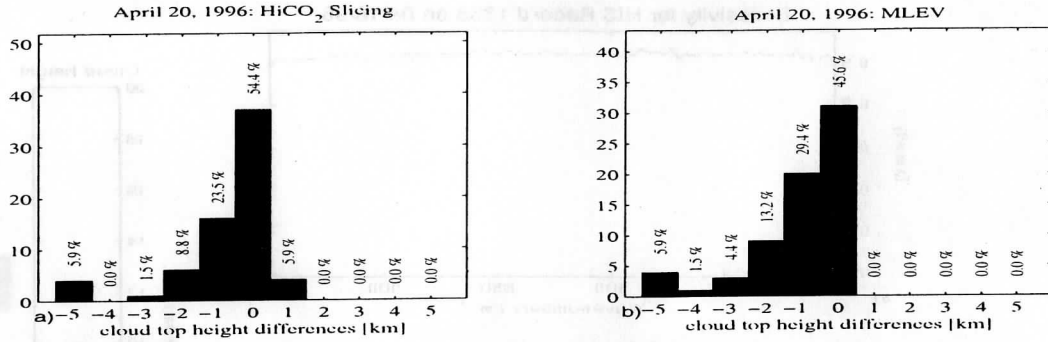


Figure 5: 960420: Cloud top height retrievals. The histograms show the differences between the retrieved cloud top height (*HiCO₂ Slicing* on the left and *MLEV* on the right) and the peak of the back-scattered lidar signal. The statistics are derived for FOVs in which the integrated back-scattered signal was greater than 0.2 ster^{-1} for single layer clouds only. The 0 bin represents CTH retrieved in $\pm 500 \text{ m}$ from the peak of the back-scattered lidar signal.

Table 1: Result summary. Percentages of CTH retrieved within 1.5 km from the lidar back-scatter peak altitude.

	<i>HiCO₂ Slicing</i>	<i>MLEV</i>
960416: integrated back-scatter $< 0.1 \text{ ster}^{-1}$	65%	57%
960416: integrated back-scatter $< 0.2 \text{ ster}^{-1}$ & single layer clouds only	65%	62%
960420: integrated back-scatter $< 0.1 \text{ ster}^{-1}$	83%	55%
960420: integrated back-scatter $< 0.2 \text{ ster}^{-1}$ & single layer clouds only	90%	64%

forward model, already created, will be used. The model inputs vertical profiles of Temperature, Water Vapor and Ozone defined over 40 levels with a vertical resolution of 500 m .

In any case, for each flight, both the distributions are skewed in the same direction and in both cases, as expected, the results for single layer clouds are more accurate. The consistency between the results indicates that it will be possible to combine the two algorithms to define a confidence level to be associated to each retrieval. The way of combining them and the criterion used to assign the confidence level to the retrieval are still under investigation and are not presented in this paper.

Figure 6 shows an example of *MLEV* retrieval, figure a) represents the retrieved effective spectral emissivity, b) shows part of band 1 HIS observed spectrum and c) shows the retrieved CTH and the lidar back-scatter peak altitude.

4.3 Particle Size and Optical Thickness Retrieval

Once the CTH is retrieved, the particle size and optical thickness retrieval is applied to the entire flight. For this experiment the temperature and water vapor profiles used to retrieve CPS and COT are obtained from radiosonde observations. In the operational framework they will be derived from clear sky sounding retrievals. Figures 7 a) and b) show, as an example, a single case of retrieval. Figure 7 a) shows why to determine the first guess of the optical thickness only the microwindows in band 2 (midwaves) are used. The figure shows how the band 1 microwindows (longwaves) are sensitive to the effective particle size, while the band 2 microwindows are less sensitive to particle size and more sensitive to optical thickness. After the first guess has been determined, the particle size is selected matching the slope of the band 1 real and simulated microwindows, as in figure 7 b). The last step of the algorithm determines the final value of optical thickness by matching the values of the simulated and real band 1 microwindows for the selected particle size.

The retrieved optical thickness is finally used for a consistency check. Its value is converted in emissivity using the following expression:

$$\eta = 1 - e^{-\tau} \quad (10)$$

where τ is the retrieved optical thickness (at $11 \mu\text{m}$) and η is the effective emissivity (at $11 \mu\text{m}$). In the example

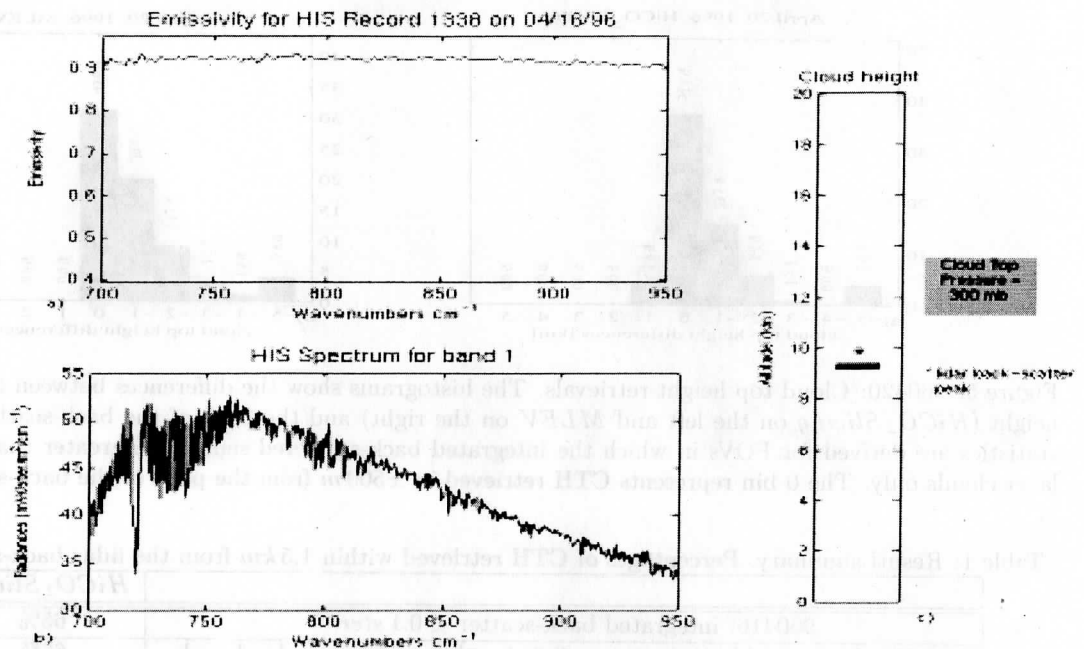


Figure 6: Example of *MLEV* retrieval. The CTH (c) and Effective Emissivity (a) are retrieved for FOV 1338 (UTC 21:33:18) of the 960416 flight. (b) represents part of the observed HIS spectrum. The asterisks in (c) represents the lidar back-scatter peak altitude.

showed in figures 7 and 6, *MLEV* and *HiCO₂ Slicing* retrieved a value of $\eta \simeq .93$ while the particle size and optical thickness retrieval, through eq. 10, gives a value $\eta = .99$.

5 Conclusions and Future Work

The work presented in this paper is intended to describe the basic foundations for the cloud detection and cloud property retrieval for very high spectral resolution instruments like GITS, AIRS, CrIS. The scheme for the cloud property retrieval is based on the combination of different approaches to retrieve CTH, CEE and CPS. Two approaches are used to derive CTH and CEE, the first approach being based on the well tested *CO₂ Slicing* algorithm adapted to high spectral resolution measurements, and the second on the novel *MLEV* algorithm. The two approaches, both physically based, are built on different principles. The combination of the results obtained by using the two approach might improve the estimate of the CTH and might provide a confidence level to be associated to the CTH retrieval. The way of combining the results to derive a confidence level is still under investigation and is not presented in this paper. A third approach is used to derive CPS and COT for any given FOV, it requires the knowledge of the CTH and of the temperature and water vapor profiles. The COT is then converted to CEE for a consistency check with the CEE values retrieved by the first two approaches.

The results obtained, validated by the collocated lidar measurements, suggest that the *HiCO₂ Slicing* algorithm are more accurate than those obtained by *MLEV*, and that both the algorithm results are consistent with each other. The higher accuracy showed by the *HiCO₂ Slicing* can be explained by the following considerations:

- as Huang [5] suggested that the *MLEV* performs better for clouds below 200 hPa and is not optimal for cold isothermal regimes
- the impact of the limits of the HIS forward model [10], currently used to simulate the radiances for the retrievals, is different for the two algorithms. An improved version of the forward model has been realized and will be tested soon.

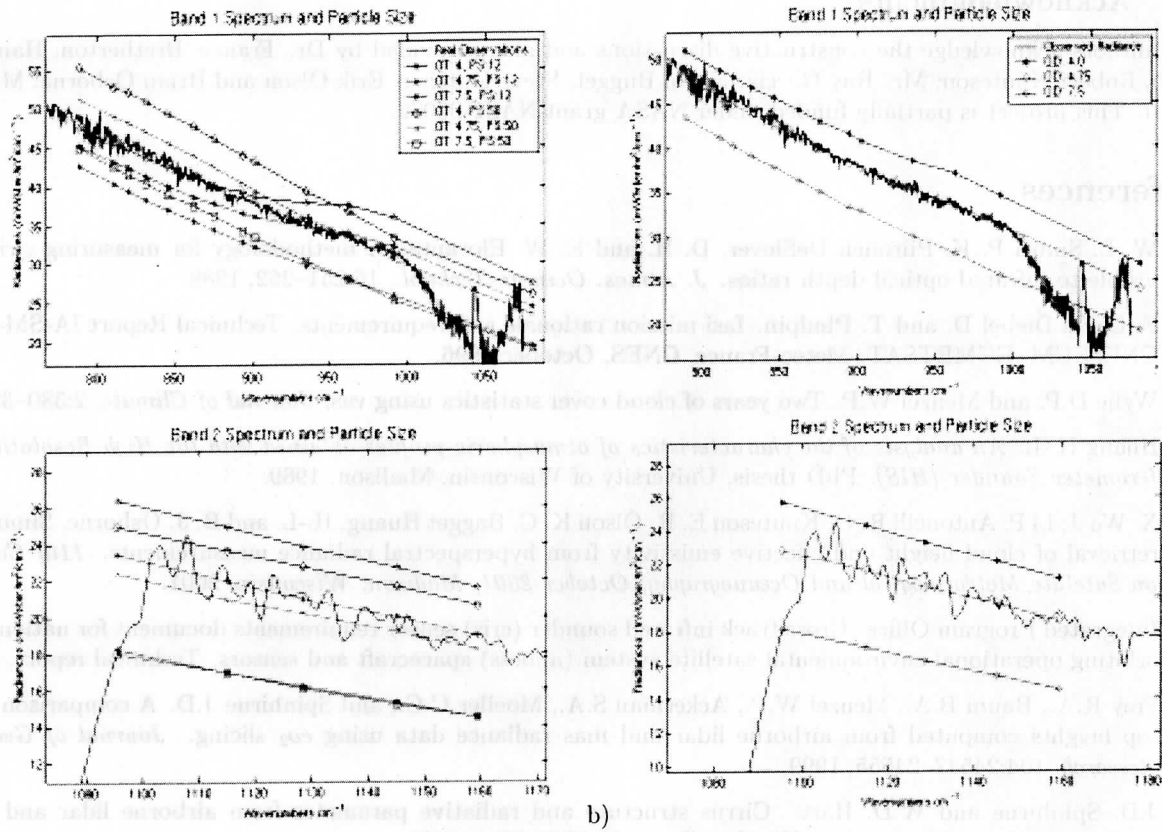


Figure 7: a) Particle Size Retrieval. Date: 960416; ScanLine: 1338; UTC: 21:33:18.

- a) The solid line represents the HIS observed spectrum. The other curves represent respectively the microwindows generated for effective particle size of $12\ \mu\text{m}$ and $50\ \mu\text{m}$ and optical thickness 4, 4.75, 7. A first guess of the correct optical thickness is identified using band 2 (lower plot) only. The slope of the microwindows in this band, in fact, appears not to be sensitive to the effective particle size.
- b) The solid line represents the HIS observed spectrum. The hexagrams, circles, and diamonds represent respectively the microwindows generated for effective particle size of $20\ \mu\text{m}$ and optical thickness 4, 4.75, 7. Once a first guess correct optical thickness is identified using band 2 (lower plot) the optimal particle size is retrieved matching the values and the slope of the band 1 microwindows. After deriving the optimal value for the particle size is retrieved the first 11 microwindows (band 1 only) are used to refine the retrieved value of COT, simply by matching the simulated radiances to the real radiances for those microwindows.



The hyper spectral version of the *CO₂ Slicing*, seems to perform better than the classical broad band version, but more extensive test are required before drawing final conclusions.

The CPS and COT retrieval provides results consistent with the *HiCO₂ Slicing* and *MLEV* algorithms, but currently the results are not validated by any in-situ measurements. In this sense more work is required to validate the results. The algorithms themselves need to be improved and more widely tested, but the early results are encouraging and show that the high spectral resolution measurements will improve our capability of retrieving cloud properties.

5.1 Acknowledgments

The authors acknowledge the constructive discussions and ideas provided by Dr. Francis Bretherton, Hank Revercomb, Robert Knuteson, Mr. Ray Garcia, Kevin Bugget, Steve Dutcher, Erik Olson and Brian Osborne; Ms Shaima Nasiri. This project is partially funded under NASA grant NAS1-00072.

References

- [1] W. L. Smith P. K. Piironen DeSlover, D. H. and E. W. Eloranta. A methodology for measuring cirrus cloud visible to infrared optical depth ratios. *J. Atmos. Oceanic Technol.*, 16:251-262, 1989.
- [2] F. Cayla Diebel D. and T. Phulpin. Iasi mission rationale and requirements. Technical Report IA-SM-0000-10-CNE/EUM, EUMETSAT, Meteo-France, CNES, October 1996.
- [3] Wylie D.P. and Menzel W.P. Two years of cloud cover statistics using vas. *Journal of Climate*, 2:380-392, 1989.
- [4] Huang H.-L. *An analysis of the characteristics of atmospheric profiles obtained with the High-Resolution Interferometer Sounder (HIS)*. PhD thesis, University of Wisconsin, Madison, 1989.
- [5] X. Wu J. Li P. Antonelli R. O. Knuteson E. R. Olson K. C. Bagget Huang, H.-L. and B. J. Osborne. Simultaneous retrieval of cloud height and effective emissivity from hyperspectral radiance measurements. *11th Conference on Satellite Meteorological and Oceanography, October 2001, Madison, Wisconsin*, 2001.
- [6] Integrated Program Office. Cross track infrared sounder (cris) sensor requirements document for national polar-orbiting operational environmental satellite system (npoes) spacecraft and sensors. Technical report, 1997.
- [7] Frey R.A., Baum B.A., Menzel W.P., Ackerman S.A., Moeller C.C., and Spinhirne J.D. A comparison of cloud top heights computed from airborne lidar and mas radiance data using *co₂ slicing*. *Journal of Geophysical Research*, 104:24547-24555, 1999.
- [8] J.D. Spinhirne and W.D. Hart. Cirrus structure and radiative parameter from airborne lidar and spectral radiometer observations. *Mon. Weather Rev.*, 118:2329-2343, 1990.
- [9] W.D. Hart Spinhirne, J.D. and L.O. Caudill. Cloud top remote sensing by airborne lidar. *Appl. Opt.*, 21:1564-1571, 1982.
- [10] L. L. Strow, H.E. Motteler, R.G. Benson, S.E. Hannon, and S. De Souza-Machado. Fast computation of monochromatic infrared atmospheric-transmittances using compressed look-up tables. *Journal of Quantitative Spectroscopy and Radiative Transfer*, 59:481-493, 1998.
- [11] Smith W.L., Howell H.B., and Woolf H.M. The use of interferometric radiance measurements for sounding the atmosphere. *J. Atmos. Sci.*, 36:566-575, 1979.
- [12] Smith W.L., Revercomb H.E., Howell H.B., and Woolf H.M. His - a satellite instrument to observe temperature and moisture profiles with high vertical resolution. *AMS, Boston. Preprints Fifth Conference on Atmospheric Radiation.*, page 9, 1983.
- [13] Smith W.L. and Frey R.A. On cloud altitude determinations from high resolution interferometer sounder (his) observations. *Journal of Applied Meteorology*, 29:658-662, 1990.
- [14] B.C. Gao B.A. Baum Y.X. Hu W. Wiscombe M.I. Mischenko D.M. Winker Yang, P. and S.L. Nasiri. Asymptotic solutions of optical properties of large particles with strong absorption. *Applied Optics*, 40:1532-1547, 2000.